Study of Line Edge Roughness and Interactions of Secondary Electrons in Photoresists for EUV Lithography

Suchit Bhattarai

Electrical Engineering and Computer Sciences
University of California at Berkeley

July 9, 2017

Acknowledgement

Study of Line Edge Roughness and Interactions of Secondary Electrons in Photoresists for EUV Lithography

by

Suchit Bhattarai

A dissertation submitted in partial satisfaction of the
requirements for the degree of
Doctor of Philosophy

in

Engineering - Electrical Engineering and Computer Sciences

in the

Graduate Division

of the

University of California, Berkeley

Committee in charge:

Professor Andrew R. Neureuther, Chair
Dr. Patrick P. Naulleau
Professor Jeffrey Bokor
Professor Thomas Devine

Summer 2017

Study of Line Edge Roughness and Interactions of Secondary Electrons in Photoresists for EUV Lithography

Abstract

Study of Line Edge Roughness and Interactions of Secondary Electrons in Photoresists for EUV Lithography

by

Suchit Bhattarai

Doctor of Philosophy in Engineering - Electrical Engineering and Computer Sciences

University of California, Berkeley

Professor Andrew R. Neureuther, Chair

EUV lithography (EUVL) is a candidate technology for patterning of ever shrinking feature sizes in integrated circuits. There are several challenges to high volume manufacturing of devices using EUVL in a cost-effective manner, which include limited source power, mask defects and non-idealities in the photoresist, the imaging medium. Focus of this thesis is on photoresists. Specifically, influence of absorption shot noise on the final LER was studied experimentally through comparative analysis of LER obtained with EUV (92 eV photons) and 100 keV e-beam lithography. The key contribution here is that the lithography experiments were performed with matched imaging conditions between EUV and e-beam, which allowed for a fair comparison between the LER values measured using the two patterning technologies. In scenarios where the e-beam spatial resolution was better than that for EUV, the technique of gray-scale e-beam lithography was experimentally demonstrated to result in closely matched image gradients between e-beam and EUV patterning. It was shown that the measurable parameter known as the exposure latitude is a good parameter to test whether the aerial images between two experiments have identical gradients for idential materials and processing conditions.

With matched imaging conditions, resist materials and processing conditions, lithographic data showed that the incident flux needed to pattern 50 nm half-pitch lines and spaces for a leading chemically amplified resist was 10.7 photons/nm^2 for 92 eV photons, and 4.44 e$^-$/nm^2 for 100 keV electrons. Measurements of absorption of 100 keV electrons estimated through an EELS measurement with 120 keV beam showed that despite having access to core levels in the material (e.g., 284 eV edge in carbon), these electrons mostly just excite the energy levels less than 100 eV in the resist, with a mean deposited energy of 35 eV. Results showed that the probability of an energy loss event in a 45 nm thick resist film with 100 keV electrons was 0.4, about 2.35x larger than that for EUV (0.17). By combining the incident flux and the absorption probabilities, the absorption flux was found to be similar between the two patterning technologies. A possible reason is that either the secondary electron spectra created in the material through ionization events are similar for EUV and

100 keV e-beam exposures, or that there are only small differences which ultimately do not matter from the standpoint of acid generation statistics. With matched imaging conditions and matched absorption density, the mean LER for e-beam was found to be larger by about 1 nm.

Influence of various material contributors in determining the resist LER was also studied from a modeling standpoint. Reaction/diffusion parameters in a stochastic resist model were calibrated to resist contrast curve data and line/space patterns. With the best fit reaction and diffusion parameters, the contributions of absorption shot noise, acid generation statistics and the base counting statistics on the resist LER were determined. Shot noise was found to account for 46% of the total LER, while the acid generation and base loading statistics were found to account for 22% and 32% of the LER respectively.

Interactions of low energy electrons in EUV resists were studied from both experimental and modeling standpoint. Low energy (< 92 eV) electrons are primarily responsible for initiating chemistry that leads to image formation in EUV resists. Thus key to controlling EUV exposure efficiency is understanding low energy electron radiation chemistry efficiency as a function of electron energy. Thickness versus exposure dose measurements were made with incident electron energies ranging between 29 eV and 91 eV. Thickness removed was much larger than the average secondary electron range and was bake temperature dependent and thus is a useful indicator of de-protection blur introduced by the bake process. The dissolution volume per eV deposited energy was nearly similar for 29 eV to 91 eV energies, although there is some indication that incident electrons with lower energies are slightly more effective at causing chemistry. The volume removed per eV was about 0.1 nm^3 per 1 nm^2 area.

The well-known dielectric model for inelastic scattering was used to develop a stochastic model for simulating trajectories traversed by secondary electrons in the resist. Electron energy loss spectroscopy (EELS) was used to measure the dielectric function for a leading chemically amplified resist. Analytical expressions for the Mermin dielectric functions which account for energy and momentum transfer were then fit to the measurement to build a complete dielectric model for the resist. Stochastic simulations were then performed with the scattering parameters determined by the dielectric model to calculate energy deposition and acid generation statistics. These results were used to quantify the net acid generation blur, which was found to be between 1.8 nm and 2 nm from the point of origin of the electrons. The radial distribution of acid generation sites was fit using a Rayleigh distribution and the best fit σ parameters in the distributions were found to range between 1.2 nm at 30 eV and 1.41 nm at 91 eV. The net acid yield calculated by the simulator was found to be 1.6 for an 80 eV electron.

Dedicated to Mom and Dad

Contents

List of Figures

List of Tables

Acknowledgments

First, I would like to thank my advisors Andy Neureuther and Patrick Naulleau for their mentorship all these years, for creating a great research environment, for always being available to discuss research ideas, and their overall compassionate nature in general. From them, I have learned a great deal about doing good science and engineering, as well as communicating the research findings in an effective manner. I would also like to thank Professor Jeff Bokor and Professor Tom Devine for serving in my qual and thesis committees.

I would also like to thank the Berkeley MET (BMET) operators who ran the EUV exposures for my research, including Chanin, Warren, Jessalyn, Margaret and Kurt. I would like to thank Weilun Chao of Center for X-Ray Optics (CXRO) for help with performing the e-beam experiments, and for letting me use the tools in his lab. I would like to thank Eric Gullikson and Julia Meyer-Ilse of CXRO for help with performing measurements of the optical properties of resists with the CXRO reflectometer. I would like to thank Shaul Aloni from Molecular Foundry for help with performing EELS measurements in EUV resists. I also thank Andreas Schmid and Gong Chen from the National Center for Electron Microscopy (NCEM) for help with performing the LEEM exposures with low energy electrons on an EUV resist. I would also like to thank Deirdre Olynick previously from Molecular Foundry, and Frank Ogletree, also from Molecular Foundry, for useful discussions. I would also like to thank Shirley Salanio from the EECS department for help with all kinds of administrative details.

I would like to thank Tom Wallow from ASML, who was my mentor during a summer internship, as well as Moshe Preil from Global Foundries who was my mentor during another internship. I had a great time working on projects with them, and also got a chance to learn about the kinds of problems they're working on solving. I would also like to thank the funding agencies for supporting this research, including the IMPACT+ (Integrated Modeling Process and Computation for Technology) center and C-DEN (Center for Design-Enabled Nanofabrication).

I would like to thank both current and previous colleagues of mine in our EUV research group, including Henry, Rene, Rick, Stuart, Colin, and Aamod, for being cool people. Lastly, I want to thank my mom and dad for their unconditional love and support.

Chapter 1

Introduction

Lithography is a technology that enables mass production of integrated circuits. Currently the techology used by the industry is known as deep ultraviolet (DUV) lithography. Conceptual overview of the patterning process using a deep-ultraviolet (DUV) imaging system as an example is illustrated in Fig. 1.1 [1]. The mask contains the circuit patterns that need to be printed, encoded in the form of a binary grating. The grating has selected regions that allow light to go through, while other regions that absorb the incident light. Light emerging from the non-absorbing regions of the mask diffracts, and the diffracted orders that fall within the acceptance angles of the lens propagate onto the wafer plane and form an image. A photo-sensitive material known as the photoresist is first spin-coated, then baked before the exposure. The exposure leads to photo-chemistry in selected regions of the resist. Formation of the chemical image typically requires a bake process which drives several reaction and diffusion mechanisms. Subsequently, the resist patterns are developed in a special solvent which, in the case of a positive tone resist, causes the reacted regions of the resist to dissolve in it. This process leads to the formation of thickness differential in certain regions of the resist. Resist remains in the bright regions of the mask or in the dark regions of the mask depending on the imaging tone. The final step involves pattern transfer onto the substrate through an etching process.

The driving force behind innovations in the lithography industry is Moore's law. In 1965, Gordon E. Moore performed a fit on the number of integrated components in the four preceding years on a logarithmic axis to predict that the number of components in an integrated circuit should double every year [2]. In recent times, continuing the scaling trends with high yield and low costs has proven to be increasingly challenging.

The theoretical pitch resolution of a periodic pattern that can be printed with single exposure with a diffraction limited optical system is given by equation 1.1. Here, λ is the wavelength of light, NA is the numerical aperture defined as the sine of the maximum diffraction angle emerging from the mask that can be collected by the lens, and k_1 is a technological constant. The value of k_1 can be lowered by using resolution enhancement techniques, but it has a lower limit of $1/2$. Thus, the smallest possible pitch for single exposure is $0.5\lambda/\text{NA}$.
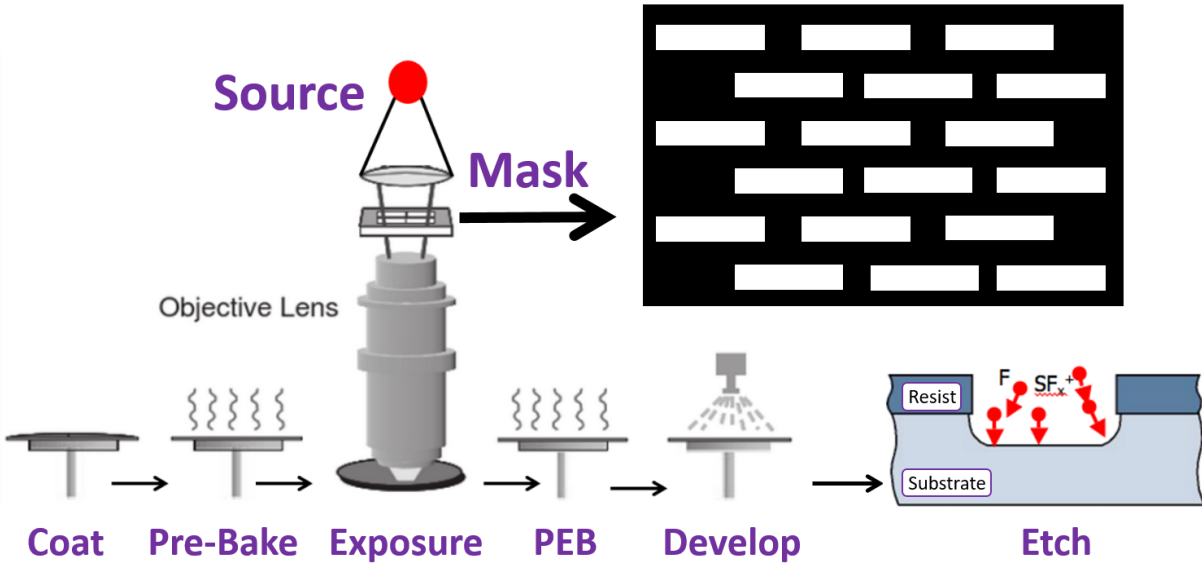
Figure 1.1: Overview of lithography and pattern transfer processes [1]

$$PitchResolution = k_1 \frac{\lambda}{NA} \tag{1.1}$$

This equation shows that by decreasing the wavelength and increasing the NA, smaller features can be printed. In addition to these knobs however, the lithography industry has had to rely on multiple patterning techniques for shrinking the feature sizes even more. While these techniques can help, they can drive up the cost and impact yield specially at smaller feature sizes. The promise of EUV lithography is that it allows for a drastic reduction of the wavelength of light down to 13.5 nm, a factor of 14.3 reduction relative to a DUV system. This technology has therefore received attention from the lithography industry for more than two decades. An example imaging system used in EUV lithography is shown in Fig. 1.2 [3]. In current versions of the commercial tools tin droplets are used as the source. The droplets are struck with a pulsed CO_2 laser, which results in the production of a plasma, and emission of 13.5 nm wavelength light. While the example DUV imaging system shown in Fig. 1.1 utilizes refractive optics, at EUV wavelengths this is not feasible as materials absorb strongly. Therefore, the masks and the optics have to be reflective. Reflectivity of a thin layer is small because the index of refraction at EUV is very close to one. Therefore, multilayer mirrors made with Molybdenum and Silicon (Mo/Si) stacks are used as the reflectors.

While the improved resolution is a big advantage to using EUV lithography, there are practical challenges which have delayed the deployment of the technology for high volume manufacturing. The biggest hurdle has been source power, which directly impacts through-put. A second challenge has to do with defects on the mask which can affect printing. They
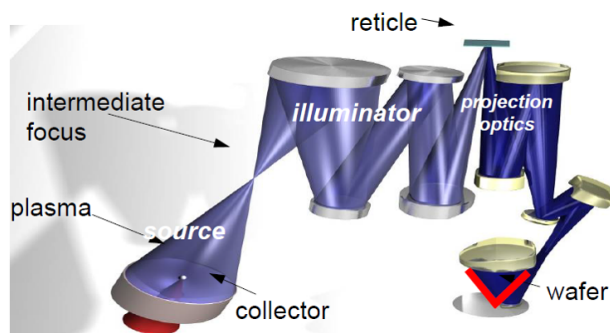
Figure 1.2: An example EUV lithography imaging system [3]

can be introduced during the multilayer deposition process, and may even be buried deep in the multilayer [4][5].

The third important challenge for EUV lithography deals with photoresist, the medium that is responsible for forming the chemical image. One of the biggest challenges is known as the resolution, LER and sensitivity (RLS) trade-off. Here, resolution (R) is the net chemical blur of the resist, the LER (L) refers to the statistical fluctuations on the placement of the edge of a line in the resist, and the sensitivity (S) refers to the dose needed to pattern a given feature. This trade-off suggests that the three parameters cannot be simultaneously improved [6].

1.1   How Chemically Amplified Resists Work

One of the most widely used family of resists are the chemically amplified resists (CARs). These resists are polymeric systems loaded with photo-acid generators (PAGs) at a certain percent by volume. The polymer also has protecting groups known as tert-butoxycarbonyl (tBOC). These groups serve the purpose of covering the regions of the polymer that are soluble in a developer like tetra-methyl ammonium hydroxide (TMAH). When exposed to 193 nm wavelength (6.44 eV) photons in a DUV lithography system, the photons excite the PAGs, resulting in the generation of acids. When exposed to 13.5 nm wavelength photons in an EUV lithography system (92 eV), the most probable outcome of the absorption of the photon is the generation of photo-electrons, which subsequently can result in the creation of secondary electrons. Some of these electrons can excite the PAGs to generate the acids. After these initial events, there is a spatial distribution of generated acids in the material, with some volumetric number density. The next step in the imaging process is to bake the resist. During the bake, the acids gain enough energy to diffuse through the material and react with the t-BOC protecting groups, thus de-protecting these sites. The "chemically amplified" aspect of these resists has to do with the fact that the acid acts as a catalyst, which means that it is capable of causing many de-protection reactions over a certain spatial

range. After the bake, when the resist is put in a special solvent, the de-protected regions dissolve away, thus resulting in a height differential in selected regions.

1.2 Line Edge Roughness in Resists

Image formation in the resist is a stochastic process that involves discrete events. This results in the formation of line edge roughness. A simple demonstration of line edge roughness over a length L is provided in Fig. 1.3. The dashed black line is the ideal desired edge position based on the pattern on the mask. Solid blue lines represent edge positions in the resist pattern.
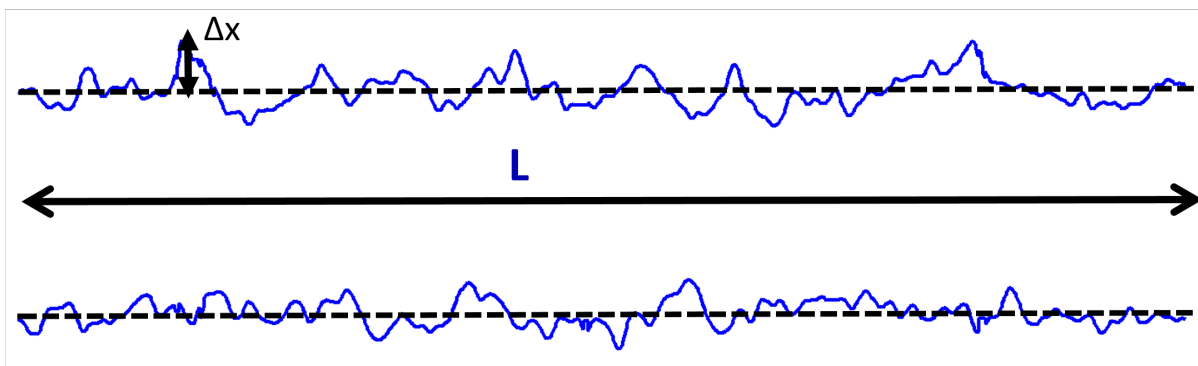
Figure 1.3: Line edge roughness (LER) demonstration

One of the properties of resist LER is that it is a form of correlated noise because the acids that are responsible for causing deprotection reactions (in a chemically amplified resist) do so over a certain spatial range governed by their diffusivity. By analyzing the LER along the length of the line L, its correlation properties can be calculated. Example calculations are shown in Fig. 1.4. Plot on the left shows the auto-correlation function, while the plot on the right shows the power spectral density defined as the magnitude squared of the Fourier transform of the edge deviations relative to the mean edge position. An uncorrelated process would result in an auto-correlation function that is a Dirac delta function and a power spectral density that is flat across all spatial frequencies. In a resist, the auto-correlation function has a certain non-zero width related to the correlation length. The correlated nature of LER is also responsible for the shape of the PSD. At large spatial frequencies corresponding to length scales smaller than the correlation length, the PSD magnitudes are small. At lower frequencies corresponding to length scales larger than the correlation length, the PSD magnitudes are large and this is also the regime that contributes the largest fraction of the total LER.
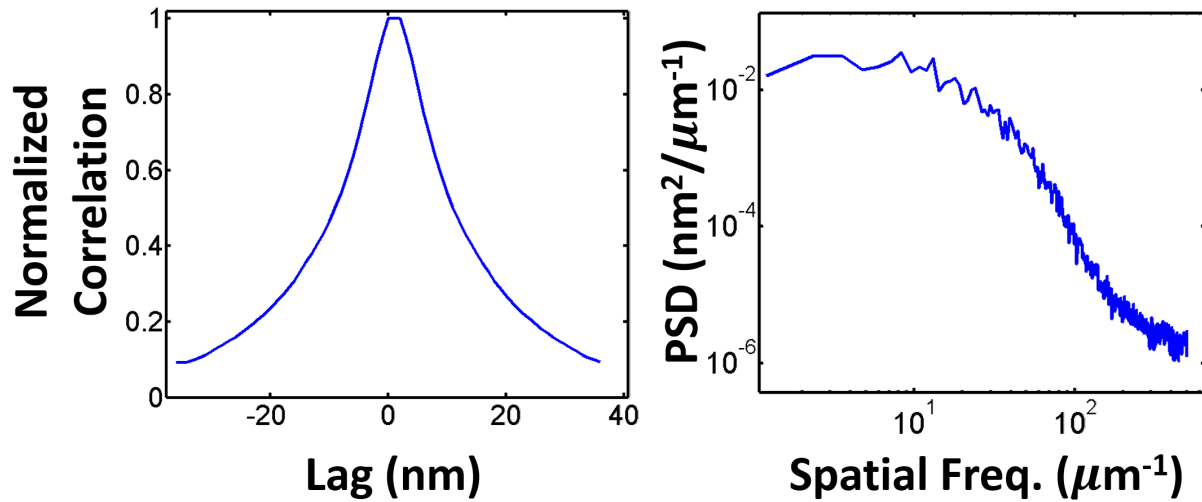
Figure 1.4: Demonstration of properties of LER; **(left):** Auto-correlation function; **(right):** Power spectral density

1.3   Thesis Structure

The two main phenomena pertaining to EUV resists that are studied in this thesis are line edge roughness (LER) and interaction of secondary electrons in photoresist materials. Of particular importance to lithography is determining the influence that all the different contributors have on the final LER. In this thesis, we first looked for LER differences between e-beam and EUV lithography for identical materials and processing conditions. This led to practical issues with creating comparable EUV and e-beam image qualities to perform a fair LER comparison. It also raised a host of fundamental questions as to the nature of exposure events in the resist, models for electron mean free path and the nature of secondary electron interactions in the material. These topics will be covered at various points in this thesis.

Chapter 2 presents an experiment designed to test whether substantial differences in absorption events density can be created by using 100 keV e-beam lithography compared to EUV lithography, and whether this can be used to experimentally test the influence of absorption shot noise on resist LER in relation to other material intrinsic contributors. The techniques for matching the imaging conditions between EUV and e-beam for a fair LER comparison will be presented. In scenarios where e-beam spatial resolution is found to be better than EUV, the technique of gray-scale lithography is used to slightly degrade the e-beam aerial image quality to match EUV. Experimental demonstration of this approach will be shown. The technique of measuring the probability of 100 keV electrons participating in energy transfer events by using electron energy loss spectroscopy (EELS) will be presented. Analysis of the LER data from EUV and e-beam patterning experiments with matched

imaging conditions will then be presented, and the expected relative LER magnitudes based on absorption shot noise alone will be compared against the measurement results.

In chapter 3, an existing stochastic resist model that treats initial absorption event and the number density of resist constituent molecules in a probabilistic manner, will be used to model line edge roughness. The procedure used for calibrating the reaction/diffusion parameters in the model to lithographic data for open frame exposures and line/space patterns will be presented. With the reaction and diffusion conditions fit to data, the contributions of absorption shot noise, acid generation statistics and the base counting statistics on the resist LER will be quantified.

In chapter 4, an experimental methodology for determining the relative capacities of electrons with various energies at triggering chemistry in the material that can ultimately lead to dissolution will be presented. In the experimental method, the EUV resist is directly exposed with electrons with energies typical of those that would be created by an EUV absorption event. The exposures were performed using a dedicated low energy electron microscope (LEEM) tool, as well as a conventional scanning electron microscope (SEM) operated in deceleration mode. The thickness loss data as a function of exposure dose will be presented for both of these techniques. The issues of sample charging that can influence the thickness loss data will be discussed. In the SEM tool, visual input observed through the secondary electron image provides useful qualitative clues pertaining to charging mechanisms that may be occuring during exposures at a given energy. For energies ranging from 29 eV to 91 eV where severe image distortions in the images were not found and measurement of the landing current was possible, quantification of the resist volume cleared per incident area density of electron flux will be presented. It will be shown that while acid generation events in the resist due to electron interactions occur in the top few nanometers, thickness loss values ranging from 7 to 10 nm are observed. Diffusion of acids into the resist during the bake process is the reason for these large thickness losses. A fitting procedure used for estimating the net acid blur during bake based on the thickness loss data will be presented.

In chapter 5, a modeling methodology to account for low energy electron interactions to complement the experimental methodology developed in chapter 4 will be presented. The dielectric model for inelastic scattering of electrons will be described. This model allows for calculation of inelastic mean free path, and the energy and angle-differential cross-sections for inelastic scattering. The method with which these pieces of information are used for modeling electron scattering in a probabilistic manner will be presented. As a way of calibrating this scattering model to photoresist data, the dielectric function for a leading chemically amplified resist was measured using electron energy loss spectroscopy. The model for inelastic scattering requires knowing the dielectric properties as a function of both energy loss and momentum transfer by an electron during the scattering process. For this purpose, the model uses the analytical dielectric functions known as the Mermin dielectric functions, which provide an explicit dependence on momentum transfer as well as energy transfer. The procedure used for calibrating the measured dielectric function in the optical limit with a linear combination of Mermin functions will be presented. After describing the probabilistic model for electron scattering, a simple model for electron-PAG interactions which accounts

for electronic excitations of the photo-acid generator (PAG) will be presented. Then, simulation scenarios that yield insights on the energy transfer and acid creation trends in resists will be presented. In the first simulation scenario, the statistics of acid creation by an electron traversing the 3-D resist grid while obeying the laws of inelastic scattering will be quantified for energies ranging between 30 eV and 91 eV. As a second analysis scenario, simulation of the thickness loss upon exposure to electrons at various energies will be demonstrated. The resulting acid distributions created near the top of the resist will then be provided as inputs to a 3-D reaction/diffusion solver with which the resist contrast curves will be calculated. The question of acids created by electrons per deposited unit energy will be studied by using the simulator.

Chapter 2

EUV Resist Shot Noise Limits: Experimental Study

2.1 Overview of Formation of the Chemical Image in a Photoresist

Lithographic patterning of nano-scale features in a photoresist involves three main steps. First, an image of the features to be printed is formed using, for example, optical projection lithography system or a direct programmed write pattern in electron-beam lithography. Next, the energy density profile incident on the photoresist selectively triggers chemistry which subsequently leads to a selective modification of the solubility of the resist when exposed to a developer solvent. Finally, dissolution chemistry results in selective removal of the photoresist depending on the selective solubility change from previous step, thus completing the imaging process and resulting in a resist height map which corresponds to either the desired pattern or the negative of it, depending on the imaging tone.

A pictorial summary of the mechanism that takes place during image formation in a chemically amplified resist is shown in Fig. 2.1. In EUV lithography, due to the ionizing nature of the radiation, the absorption of a 92 eV photon in a photoresist film leads to the generation of photo-electrons and secondary electrons with energies less than 92 eV. These low energy electrons propagate through the resist, and when they come in contact with photo-acid generators, they cause an acid generation event. Under room temperature, these acids do not have enough diffusivity, so they remain localized after the initial exposure events. The resist is therefore baked after the exposure, during which time the acids gain diffusivity so they can participate in a few reactions. One set of reactions that the acids participate in are the polymer deprotection reactions. The second set of reactions that the acids participate in are the quenching reactions with bases that are typically loaded in the resist at various concentrations for improving image contrast. These reactions help reduce the blur of the acid, and minimize the number of acids crossing the line edge from the exposed regions to the unexposed regions.

Majority of the sites on the polymer backbone in a chemically amplified resist consist of a protecting group known as the t-butoxycarbonyl (t-boc) group, which results in the polymer being insoluble in a base developer like tetramehtyl ammonium hydroxide (TMAH). An acid that comes in contact with t-boc sites can fragment the molecule, thus forming a hydroxyl group on the polymer chain [1] which makes it soluble in a basic developer like TMAH.

Incident aerial image carrying energetic photons (mJ/cm²)

Generated Acids

De-protected sites during the bake step

Post-dissolution height map
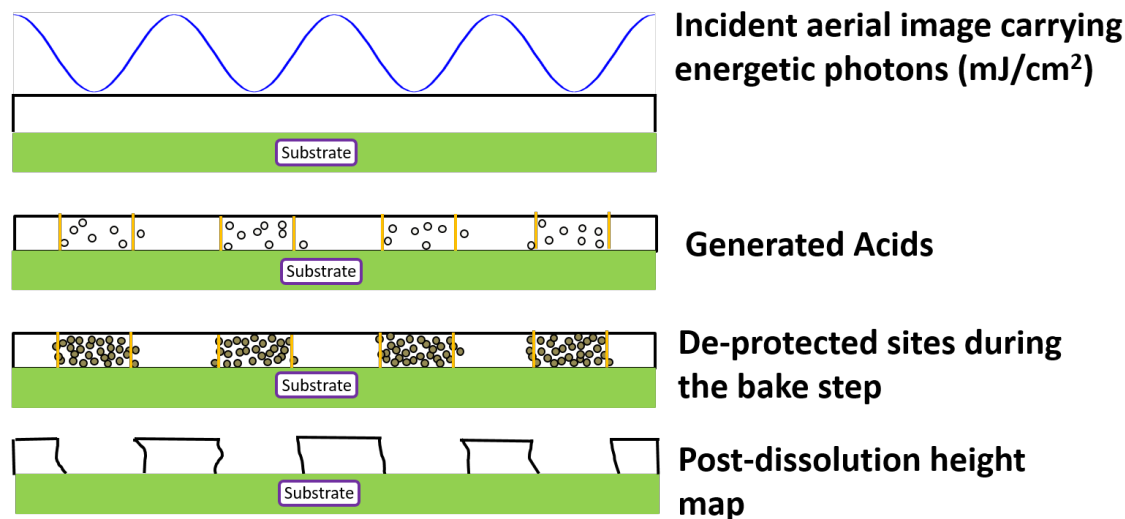
Figure 2.1: Schematic of LER Formation in an EUV Resist

2.2 Contributors to Line Edge Roughness

Line edge roughness (LER) in a resist emerges because of the fact that the exposure events and the chemistry events triggered as a result of the deposited energy density profile are discrete in nature. Owing to the Beer-Lambert law for absorption, there are not many absorption events in a photoresist film that is typically less than 50 nm thick. For example, in a photoresist consisting of the polyhydroxystyrene (PHS) based backbone polymer, the absorptivity is about $0.004/\text{nm}$, which in a 50 nm thick resist translates to an 18% absorption probability. To put it in perspective, an incident dose of 15 mJ/cm² translates to an incident flux of 10.2 photons/nm², and an absorption flux of 1.85 photons/nm². At such low photon count values, the phenomenon of exposure event shot noise starts to become important and plays a role in causing line edge roughness owing to intensity fluctuations. Since the number of acids created by the secondary electrons is only about twice as large as the number of photons absorbed, this adds additional variation that contributes to LER. In addition to the acids, the bases put in the resist for improving imaging contrast, are likely even less dense and also contribute to LER. The dissolution process where the developer molecules interact with exposed areas of the resist, also likely contributes to the final resist LER.

In addition to the material contributions to LER summarized above, the mask can also contribute resist LER [4], though it is a small contribution relative to current resist performance limits. Since the masks have to be reflective in EUV lithography, the surface roughness of the mask multilayer introduced by the non-idealities of the fabrication process result in phase roughness, which in turn couples to intensity fluctuations on the wafer plane image, known as speckle [4]. These intensity fluctuations can cause fluctuations at the line edge, and thus can contribute to LER. LER on the absorber patterns on the mask can also propagate through the optical system and show up as LER of the aerial image incident on the resist.

2.3 Experimentally Investigating the Influence of Absorption Count in Determining Final Resist LER: Methodology

Resist LER is an increasingly practical challenge for EUV lithography. Quantifying the contributions of the various material challenges is an important problem, and can aid in LER mitigation strategies. This study utilizes experimental measurements to quantify the number and influence of absorption events that ultimately dominates LER. In the study, a comparative analysis was conducted of the lithographic performance of EUV and e-beam lithography on a leading positive tone chemically amplified EUV resist with matched aerial image. In the more typical scenario where the e-beam spatial resolution is better than that for EUV, the aerial images can be matched by using the technique of gray-scale e-beam lithography. Experimental demonstration of this technique will be provided later, and an overview is provided in the next section. In the scenario where the EUV point spread function is better than e-beam, aerial images can be matched simply by defocusing the EUV image. In principle, the novel feature of this experimental approach would be that comparable lithographic experiments could be performed with the same resist reaction/diffusion chemistry and identical aerial image intensity profile. The only parameters that would be different are the initial absorption events, i.e. the secondary electron yield and energy distribution in the bulk material, which could subsequently translate into a discrepancy in the volumetric density of acids generated by an absorption event. Considering that the density of acids needed for formation of a feature of a given dimension must be identical, the difference in the acid yield between the two techniques could result in a net difference in the absorption count density. This discrepancy could then be used to test if the LER scales directly with the shot noise prediction calculated with the absorption count density. In practice however, our electron energy loss spectroscopy (EELS) measurements (to be demonstrated later) showed that while 100 keV electrons have access to the core-level energies in the material (e.g., 284 eV for hydrocarbons present in the material), majority of the energy loss events are in the less than 50 eV regime. Moreover, the mean energy loss for 120 keV electrons in 47 nm thin films containing a resist layer and a silicon nitride layer, was found to be about 37 eV.

A pictorial summary of the overall approach is provided in Fig. 2.2. Four experiments were performed, two patterning experiments (EUV and e-beam), and two experiments aimed at quantifying the probability of absorption of the energy sources (photons and electrons) in a 45 nm thick resist material. The measured LER values were then simply compared against the shot noise prediction based on absorption count data to test whether the shot noise model adequately explains the LER discrepancy, or whether other resist processing parameters have a larger influence on the LER.

Design comparable litho experiments
1. **Identical chemistry**
2. **Identical aerial image slope**

LER metrology

Measure absorption probability
1. **EUV: reflectometry (CXRO)**
2. **E-Beam: EELS (Foundry)**

Compare $\frac{LER_{EBeam}}{LER_{EUV}}$ with shot noise predictions
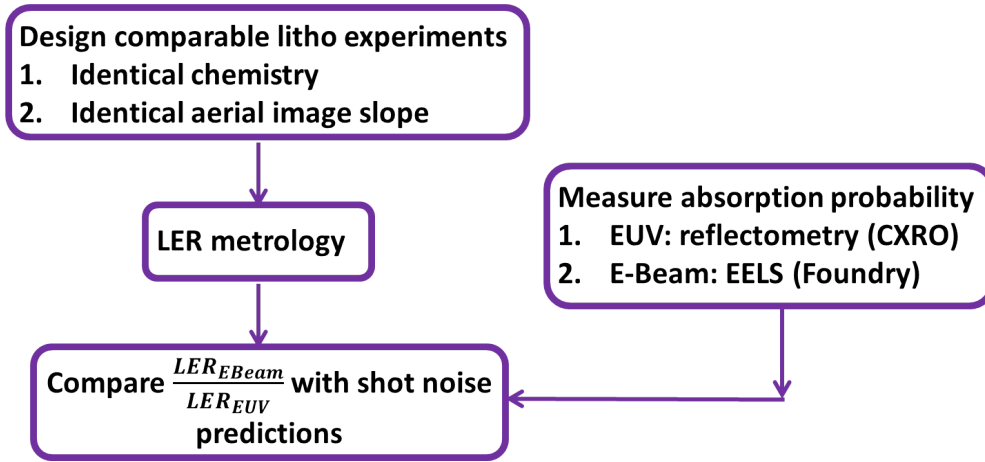
Figure 2.2: Experimental Methodology for Shot Noise Investigation

2.4   Gray-Scale E-Beam Lithography

The motivation for performing gray-scale e-beam lithography is provided by way of comparing the point spread functions (PSFs) for EUV and e-beam imaging systems illustrated in Fig. 2.3. The EUV point spread function was calculated by using an existing MATLAB based software that is capable of modeling partially coherent illumination [7]. The Berkeley MET (BMET) model for illumination conditions accounting for aberrations present in the system were used in this simulation. The e-beam point spread function was modeled simply as a Gaussian function with a full-width at half maximum of 8 nm, the measured value for the e-beam tool at the Center for X-Ray Optics (CXRO). The figure clearly shows differences in the two imaging systems, which need to be corrected for in order to perform a fair comparison of lithographic data. The inset shows the gradients of the PSF at half-maximum. Gradient for the e-beam PSF is 2.6 times larger than that for EUV.

Parameter	EUV	E-Beam
Gradient @ half-max	0.065 /nm	0.169 /nm
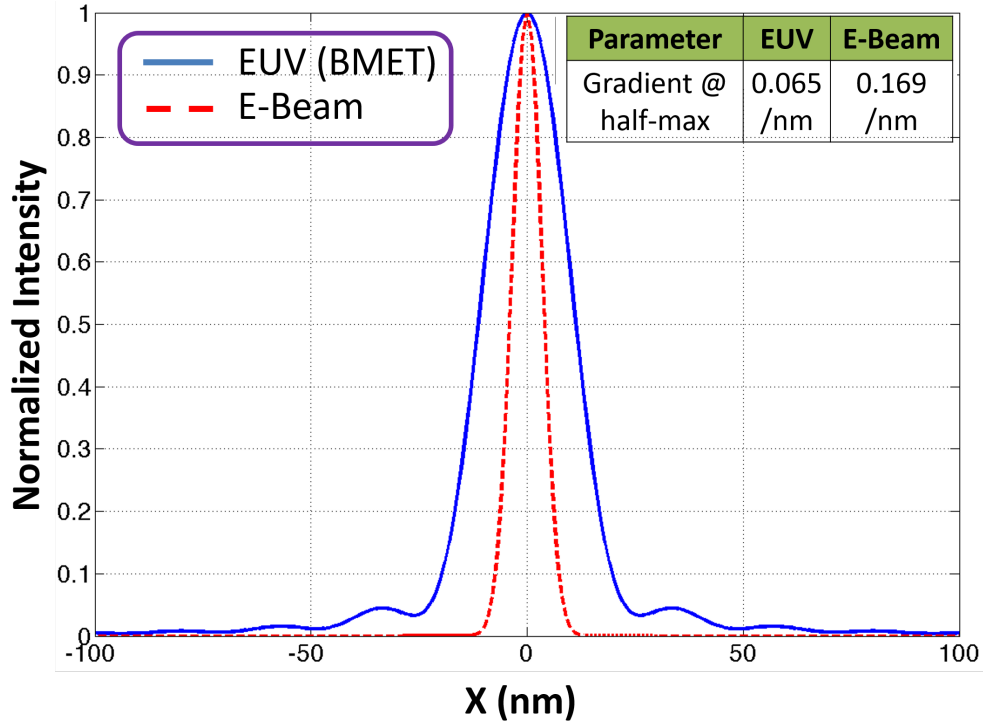
Figure 2.3: Comparison between EUV and e-beam point spread functions (PSFs)

In situations where the e-beam spatial resolution is in fact better than EUV, the goal of gray-scale e-beam imaging is to compensate for it by slightly lowering the contrast of the e-beam write pattern. This is accomplished through a simple deconvolution procedure illustrated by the diagram in Fig. 2.4. Plot on the top left shows cross-section profile of the computed EUV aerial image for 50 nm half-pitch line/space pattern calculated by assuming annular imaging conditions (σ_{in}/σ_{out}/=0.35/0.55). The illumination conditions match the conditions used for experimental results that will be shown later in this chapter. The bump near the minimum intensities results from aberrations present in the Berkeley MET (BMET). Plot on the top right shows a Gaussian point spread function with a full-width at half maximum (FWHM) of 8 nm. The plot on the bottom shows a comparison between the binary e-beam dose pattern and the gray-scale pattern computed by deconvolution in the Fourier domain. For the binary write pattern, the tool only exposes the regions along the write pattern that correspond to a value of 1 in this plot. In the gray-scale patterning technique, all regions along the write pattern are exposed at varying intensity levels by varying the dwell time per pixel at a constant beam current. The calculation here was performed by using a pixel size of 5 nm. Experimental demonstration of this technique will be presented later.
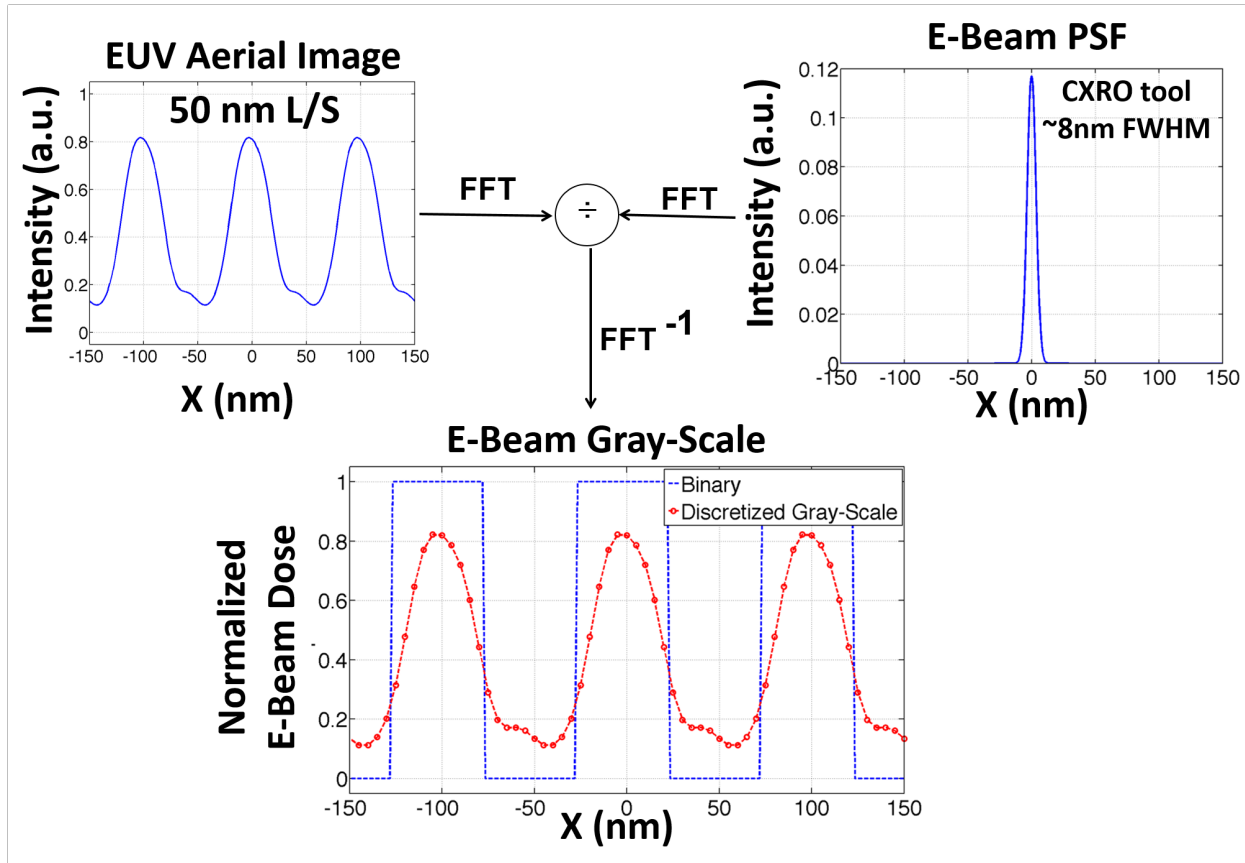
Figure 2.4: Overview of the technique of gray-scale e-beam lithography; **(top left):** EUV aerial image for 50 nm half-pitch line/space pattern; **(top right):** Gaussian e-beam PSF with an estimated full-width at half maximum of 8 nm; **(bottom):** Comparison of binary e-beam dose vs. gray-scale e-beam dose that matches EUV image-quality on the wafer plane

2.5 Measurement of Absorption Probability: 100 keV Electrons

For the absorption of an EUV photon, reflectance based measurement of the imaginary part of the material refractive index at 92 eV was performed, while the probability of absorption of an electron was measured using the technique of electron energy loss spectroscopy (EELS). A diagrammatic overview of the transmissive EELS technique is shown in Fig. 2.5. An electron-beam, typically higher energy than 100 keV, is focused onto a thin sample in a transmission electron microscopy (TEM) chamber. The electrons undergo scattering in the sample, emerge on the other side of the sample with a certain energy and angular distribution,

and subsequently pass through the magnetic spectrometer which results in deflection of electrons based on the energy and the magnitude of the magnetic field applied across it [8]. In a serial energy acquisition mode, the electrons emerging from the spectrometer are scanned across a slit, so as to make a measurement of the electron counts that correspond to various energy loss values. One of the several architectures for the electron counting system consists of a scintillator, which produces photons when struck by electrons, followed by a photo-multiplier tube where photons produce electrons due to the secondary electron emission mechanisms, which finally get collected as current on the anode terminal after going through amplification steps through accelerations in the subsequent dynode stages [8].

Example EELS spectra for four compounds from the literature, available through the EELS database [9, 10] and the EELS Atlas [11] are provided in Fig. 2.5. Typical EELS spectra have three main regimes, as illustrated in the figure. The elastic peak correponds to electrons that suffer 0 eV losses in the sample. The negative energy loss values recorded by the system result from the finite energy resolution of the tool. The full width at half maxima (FWHM) of the energy distribution under typical operating conditions are below 2 eV. The larger energy loss events in the EELS spectra can be broadly classified into the low-loss and the core-loss regimes. In the EELS literature, energy losses up to 50 eV are considered as the low-loss regime, while the energy losses larger than 50 eV are considered to be the core-loss regime. The low-loss regime consists of a major peak centered at the bulk plasmon energy of the material. Plasmons are a collective excitation of the valence band electrons in a solid, characterized by the oscillatory movement of these electrons in the presence of an electric field induced by an electron beam propagating through the sample [12]. The core-loss regime corredsponds to the excitation of deeper energy levels in the sample. For example, in the example figures shown in Fig. 2.5, we see ionization edges of Silicon and Carbon around 105 eV and 284 eV respectively.
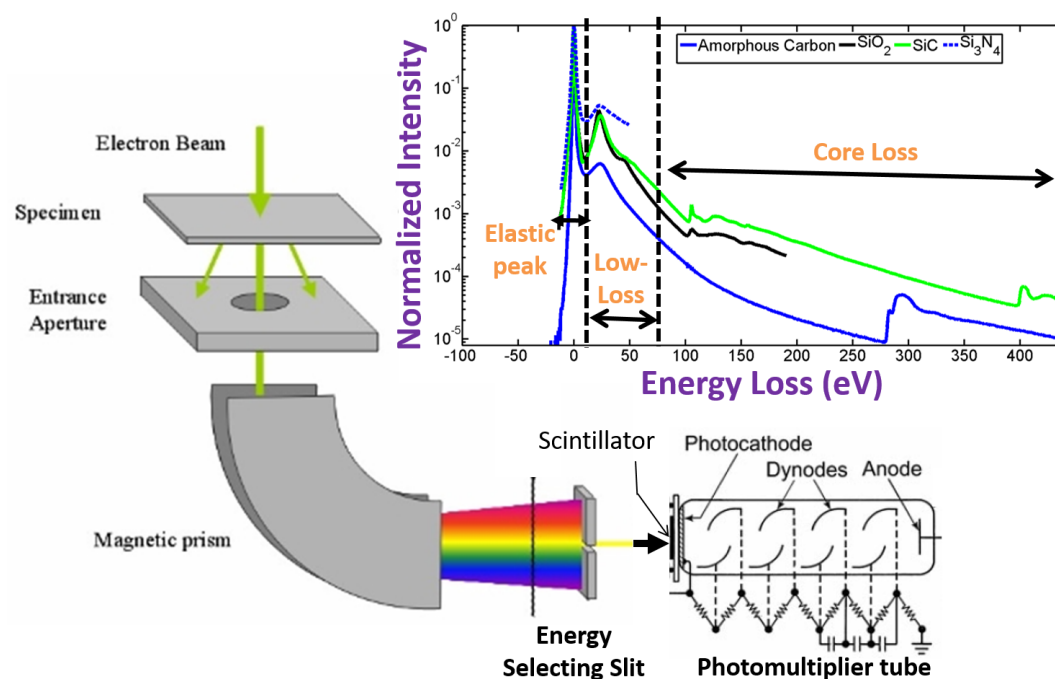
Figure 2.5: Overview of the electron energy loss spectroscopy (EELS) technique

2.5.1   The Electron Energy Loss (EELS) Experiment

For measuring the absorption probability of electrons in an EUV resist, we first spin-coated the resist on a silicon nitride window as shown in Fig. 2.6. The EELS spectrum with a 120 keV beam was first obtained on the bare nitride window, and the spectrum was subsequently measured for the resist-nitride stack using the TEM-EELS tool at the Molecular Foundry at the Lawrence Berkeley National Laboratory [13]. The bare nitride thickness was 25 nm, while the thickness of the stack was 47 nm. The data from these two measurements were then used to estimate the probability of electron absorption in the resist.
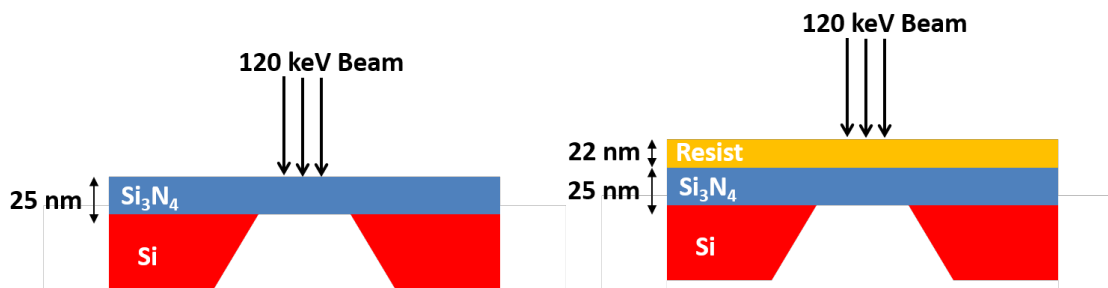
Figure 2.6: The EELS experiment technique used in this study

The EELS spectra in the low energy loss (less than 55 eV) regime were first collected by raster scanning the beam along the sample with 2.5 nm step size. The spectra in the core loss regime were then subsequently acquired at a single measurement site for both bare nitride and the resist/nitride stack. The relative signal strength in the low-loss regime (which includes the zero-energy-loss peak) and the core loss regimes are usually more than 4 orders of magnitude apart. This scheme of acquiring the data in the two regimes separately is used in the EELS community so as to adequately resolve peaks and core edges within reasonable data acquisition times. The raw EELS data for the resist/nitride stack and the bare nitride are shown in Fig. 2.7. The two plots show the spectra for the bare nitride and the resist/nitride stack acquired from 441 measurement sites by raster scanning the beam in a 50 nm X 50 nm region. We note that the number of electrons at each energy loss have small variability. The average spectra at each energy loss were calculated and are shown at the top in Fig. 2.8. The plot to the right in Fig. 2.8 shows the raw data for the core loss acquisition. The elemental contributors to various peaks are annotated. The dual peaks around 100 eV correspond to the ionization edges of silicon [14]. The 284 eV ionization edge in the resist/nitride stack data results from the presence of carbon in the photoresist. The 400 eV peaks in both the resist/nitride stack and the bare nitride correspond to the nitrogen edge.
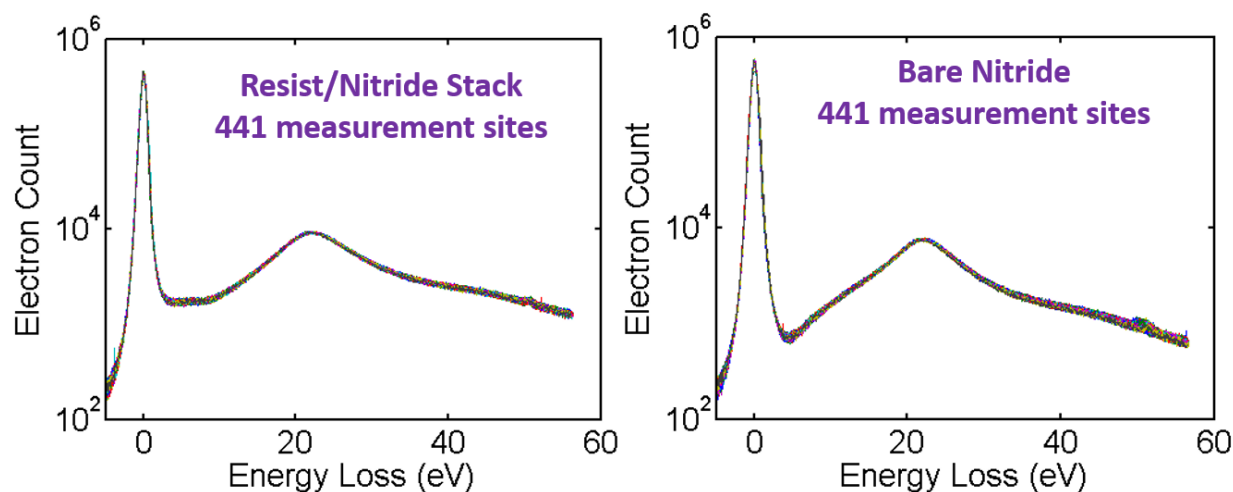
Figure 2.7: EELS data for energy loss values upto 55 eV with a 120 keV e-beam probe
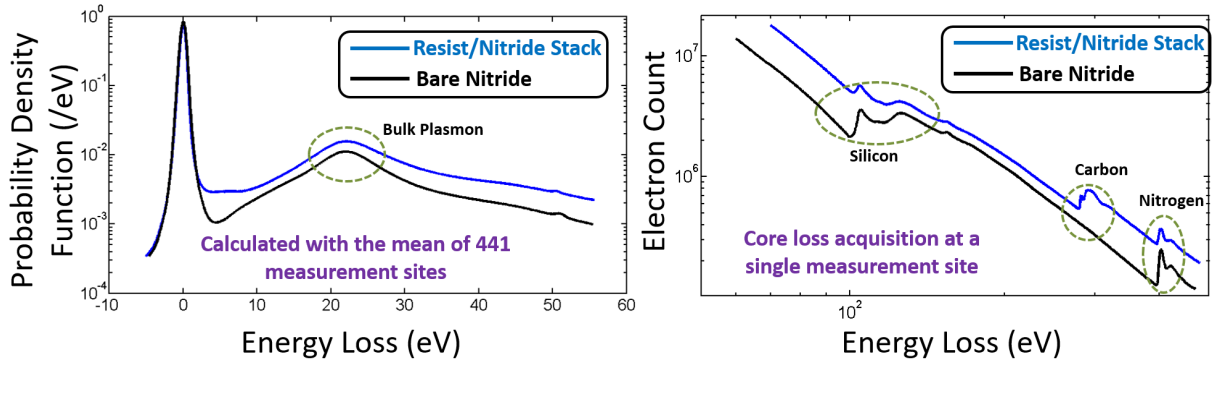
Figure 2.8: Comparison of low-energy and high-energy loss EELS data with a 120 keV e-beam probe

In order to gain better insight into the absorption probability of high energy electrons involved in e-beam lithography, we seek to synthesize the spectra for the full energy range from 0 eV to 100s of eV. For this purpose, the low energy spectra were stitched to the core loss spectra. In the 55 to 70 eV regime where data was not available, the energy loss trend in the 40-55 eV regime was extrapolated by performing a fit of the form AE^{-r} [8], done in log-log scale to extract the parameters A and r. Magnitude of the core-loss data at 70 eV was then normalized to be equal to the result of the extrapolated low loss spectra at 70 eV. The stitched spectra are shown in Fig. 2.9. For the resist/nitride stack, the mean energy loss calculated from the energy loss probability distribution is 37.15 eV, while the mean energy loss in the bare nitride is 33.77 eV. These energies were calculated by first de-convolving the plural scattering from both of the data sets to obtain the single scattering energy loss spectra for energy losses larger than 2 eV, which represent the actual inelastic scattering events in the material. Removal of plural scattering was performed using the Fourier-log deconvolution (FLOG) deconvolution technique described in detail by Egerton [8].
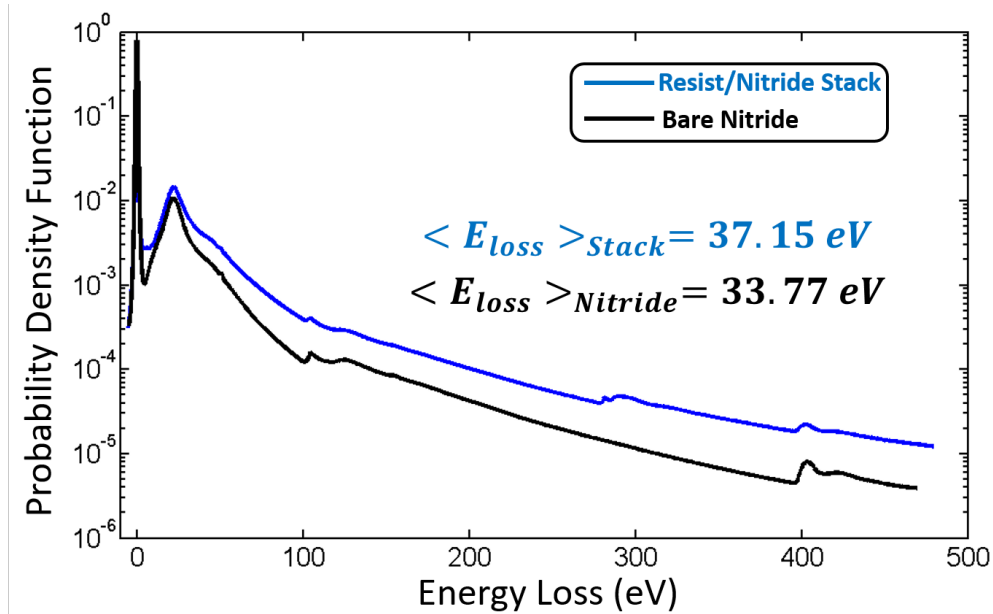
Figure 2.9: EELS data for energy losses upto 410 eV for 120 keV electrons

2.5.2   Extracting the Scattering Probability for 100 keV Electrons from the EELS Data

Estimating the probability of scattering events in the resist requires accounting for plural scattering events, where the probability of more than one event for a given film thickness increases with t/λ, where t is the thickness, and λ is the inelastic mean free path of the electron in the material. The probability that an electron undergoes n scattering events in a material can be treated as a Poisson process described by Egerton, and defined by equation 2.1 [8]. The expression for elastic scattering probability (n=0), is also shown in equation 2.1, where I_0 is the integral of the measured zero-loss peak, while I_T is the total integral of the entire energy loss spectrum.

$$P_n = \frac{1}{n!}\left(\frac{t}{\lambda}\right)^n e^{-t/\lambda}$$
$$P_0 = I_0/I_T = e^{-t/\lambda} \tag{2.1}$$

For measurements where data is available for 100s of eV of energy loss, we can estimate t/λ directly from the data. From the experimentally determined t/λ value, we can compute the inelastic mean free path of the electron given that the thickness is known. For the stitched spectra from Fig. 2.9, the calculated t/λ values are summarized in table 2.1, and are 0.47 for the resist/nitride stack and 0.25 for the bare nitride.

Table 2.1: t/λ from measured EELS data

Sample	t/λ
Resist/Nitride Stack	0.47
Bare Nitride	0.25

Using the t/λ values for the resist/nitride stack and the bare nitride measurements in conjunction with the Poisson scattering process (equation 2.1), we can compute the t/λ value for scattering in the resist using a simple probability model illustrated in equation 2.2. In the equation, p_S, p_N and p_R are the probabilities for scattering in the stack, nitride and resist respectively, and the subscripts 1 and 0 corresponds to single scattering and no scattering event scenarios, respectively. This model simply expresses the fact that the probability of a single scattering in the stack equals probability of single scattering in the resist and no scattering in the nitride, or no scattering in the resist and single scattering in the nitride. By substituting the values from table 2.1, we can solve for t/λ in the resist numerically, to obtain 0.22. With a resist thickness of 22 nm, the inelastic mean free path for 120 keV electrons in the resist is estimated to be 100 nm. For converting the incident electron dose values into discrete number of absorbed events in the 100 keV lithography data to be presented later, the inelastic mean free path above needs to be appropriately scaled. In appendix C of [8], Egerton suggests a rule of thumb that the mean free path for 100 keV for a given material is 1.45X smaller than that at 200 keV. This simple ratio was used to estimate that the mean free path at 100 keV is 0.92X as large as the mean free path at 120 keV, i.e. 92 nm.

$$p_{S1} = p_{R1} * p_{N0} + p_{R0} * p_{N1}$$
$$\left(\frac{t}{\lambda}\right)_S e^{-(\frac{t}{\lambda})_S} = \left(\frac{t}{\lambda}\right)_R e^{-(\frac{t}{\lambda})_R} e^{-(\frac{t}{\lambda})_N} + e^{-(\frac{t}{\lambda})_R} \left(\frac{t}{\lambda}\right)_N e^{-(\frac{t}{\lambda})_N}$$
(2.2)

With an estimate for the inelastic mean free path, we can use the Poisson scattering model from equation 2.1 to compute the probabilities of multiple scattering events in a 45 nm thick photoresist, which is used for lithography experiments to be demonstrated later. In Fig. 2.10, calculations for the probabilities of n scattering events in the resist are provided on the plot to the left. Plot on the right shows the cumulative absorption probability. From this plot, we see that most of the absorption of 100 keV electrons in a 45 nm thick resist is explained by single and double scattering events. Double scattering contributes about 24.7% more probability compared to single scattering. The cumulative probability saturates at $1-e^{-t/\lambda} = 0.388$.
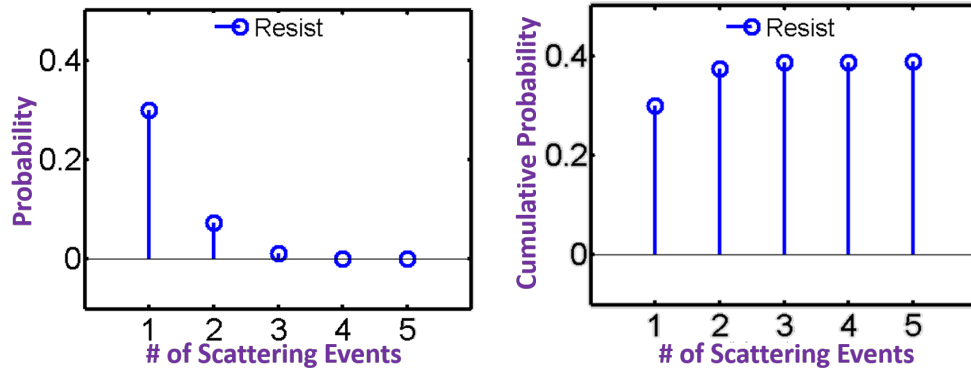
Figure 2.10: Probabilities of Multiple Scattering Events in 45 nm thick EUV resist

Equation 2.2 was also used to calculate the probability of single scattering in the resist at each energy loss value. The single scattering distributions in the stack and nitride, p_{S1} and p_{N1} respectively, for each energy loss were calculated from the raw spectra by using the Fourier-log deconvolution (FLOG) technique [8], mentioned earlier. The probability of zero scattering events in the resist and nitride, p_{R0} and p_{N0} respectively in the equation, were calculated by using the Poisson scattering model from equation 2.1 and the t/λ values reported above. The resulting energy-dependent spectrum in the resist is shown in Fig. 2.11
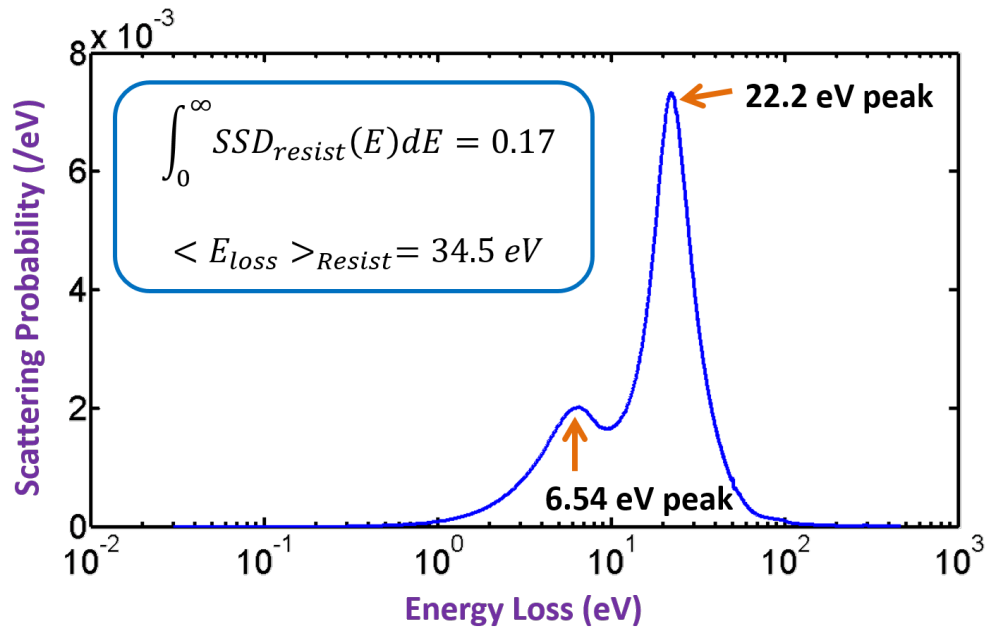
Figure 2.11: Single scattering distribution in 22 nm thick photoresist

2.6 Measurement of Absorption Probability: EUV Photons

The probability of absorption of an EUV photon in the resist is calculated by using the Beer-Lambert law for exponential decay of photon intensity in the material shown in equation 2.3, where the absorptivity (α) relates to the imaginary component of the refractive index (κ), also shown in equation 2.3.

$$I(z) = I_0 e^{-\alpha z}$$
$$\alpha = \frac{4\pi}{\lambda}\kappa \tag{2.3}$$

The complex index of refraction (n+j*k) for the photoresist was extracted from reflectance measurements from a 45 nm thick photoresist spun on a silicon substrate by using the CXRO reflectometer [15] at beamline 6.3.2 at the ALS. The measured real and imaginary parts of the refractive index of the photoresist (n and k respectively) are shown as open circles on the plot to the left in Fig. 2.12. As mentioned above, a typical positive tone chemically amplified resist is made of polyhydroxystyrene (PHS). Therefore, n and k values for PHS were obtained from the CXRO database [16], and is plotted as dashed lines. A good general agreement is seen between the measured results and the values in the database. The plot to the right in Fig. 2.12 shows the absorptivity in the material evaluated using equation 2.3 as a function of photon energy. At the EUV energy of 92 eV, the absorptivity is 4.13 μm^{-1}.
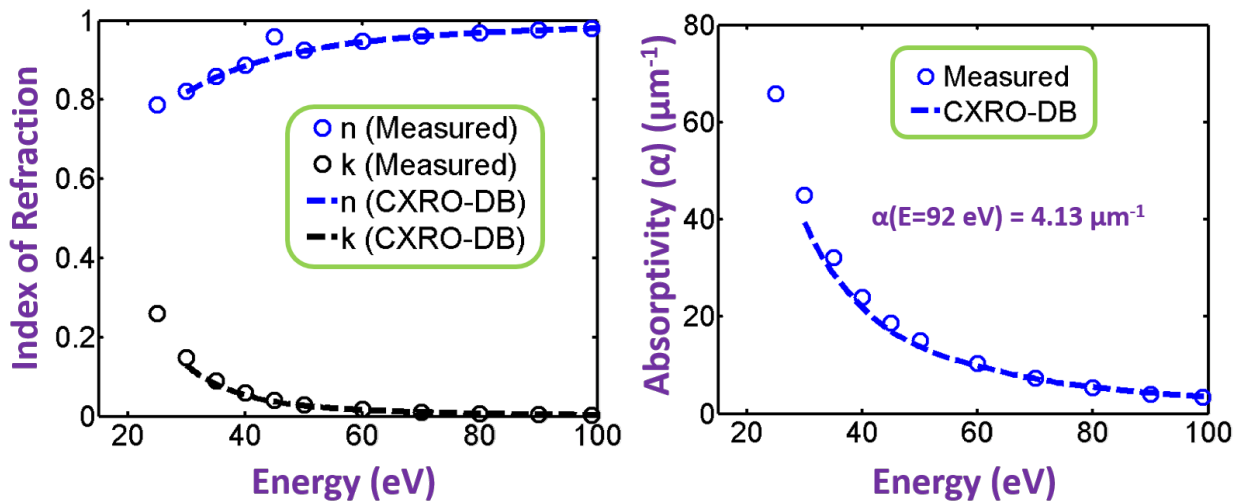
Figure 2.12: **(left):** Real and imaginary parts of refractive index from direct measurement, as well as from the CXRO database [16]; **(right):** Photon absorptivity as a function of energy

A summary of the absorption probabilities for 100 keV e-beam and 92 eV EUV photon is provided in table 2.2. The probabilities are also included for a second resist that were quantified using the exact steps illustrated above for the first resist. The interesting result that we see is that while there is a difference in absorption probability for 92 eV photons, the e-beam absorption probabilities are very close. Particularly, resist B shows a 29% larger photon absorption probability compared to resist A, while the electron absorption probability is only 3% larger than resist A. However, we note that as described above, the mean energy lost by the electrons in the resist is 34.5 eV for single scattering, and this number is likely not too much larger with double scattering. This is roughly 44% of the amount of energy delivered by an individual EUV photon.

Table 2.2: Summary of e-beam and EUV absorption probabilities in a 45 nm thick positive tone chemically amplified photoresist

Exposure Source	Probability of Absorption (45 nm film)	
	Resist A	Resist B
EUV (92 eV photon)	0.17	0.22
E-Beam (100 keV e$^-$)	0.388	0.40

2.7 Other Issues with EUV and E-beam Lithography

2.7.1 Proximity Effects in E-Beam Lithography

In the case of e-beam lithography, the highly energetic 100 keV electrons, by the time they reach the bottom of the resist, lose only a small fraction of energies in resists which are typically less than 50 nm thick. A fraction of the electrons back-scatter at the resist/silicon interface. Remainder of the electrons propagate through silicon until they lose all of their energy and come to a stop. The range of 100 keV electrons in silicon is expected to be 78.2 μm, calculated using the stopping power from the NIST E-Star database [17]. The significance of the back-scatter mechanism is that it is a long-range effect that can result in small levels of resist exposure up to tens of microns away from the exposed pixel. In the photoresist, the overall e-beam point spread function (PSF), in the polar co-ordinate system, takes the form shown in equation 2.4 [18].

$$h(r) = h_1(r) \otimes \frac{1}{\pi(1+\eta)} \Big(\frac{1}{\alpha^2} e^{-\frac{r^2}{\alpha^2}} + \frac{\eta}{\beta^2} e^{-\frac{r^2}{\beta^2}} \Big) \tag{2.4}$$

Here, h$_1$(r), α, β and η represent the spatial profile of the beam incident on the sample surface, forward scatter range, back-scatter range, and the ratio of the total energy delivered through back-scattering in the resist, relative to forward scattering [19] respectively. The forward scattering range proves to be important when the resist thickness is large (e.g., on

the order of μms), because it causes broadening of the electron beam at the bottom of the resist. For resists with thickness values on the order of about 50 nm however, the beam broadening is a negligible effect [20], such that the forward scattering term in equation 2.4 approaches the Dirac Delta function.

The back-scatter range for 100 keV and 50 keV e-beam lithography were experimentally investigated by Anderson et. al. [21] for HSQ resist on silicon substrate by using the point exposure technique with a focused electron beam [18]. By fitting the printed diameter as a function of the beam dwell time (which maps to dose), back-scatter range (β) values of 8 μm and 26 μm were estimated for 50 keV and 100 keV electron beam, respectively. These values are in reasonable agreement with the values of 9.5 μm for 50 keV and 31.2 μm for 100 keV tabulated by Owen [20].

A simple 1D calculation of the spatial profile of the global intensity contributed by the back-scatter process for 50 nm half-pitch lines with 5 nm raster scan pixel size is provided in Fig. 2.13. We expect roughly 10% lower intensity of exposure due to back-scattering 10 μm away from the center of the exposed field. In our e-beam experiment, the field sizes of the patterned line/space patterns were 20 μm X 20 μm, and the line/space patterns for LER and CD analyses were imaged near the center of the field, so the relative back-scatter induced dose perturbation is likely up to 10% in the data. The field-to-field separation between the patterns in the lithography experiment to be shown later, was 100 μm, which results in a closest separation of 80 μm between fields, which for the parameters presented above, prevents field to field proximity effects.
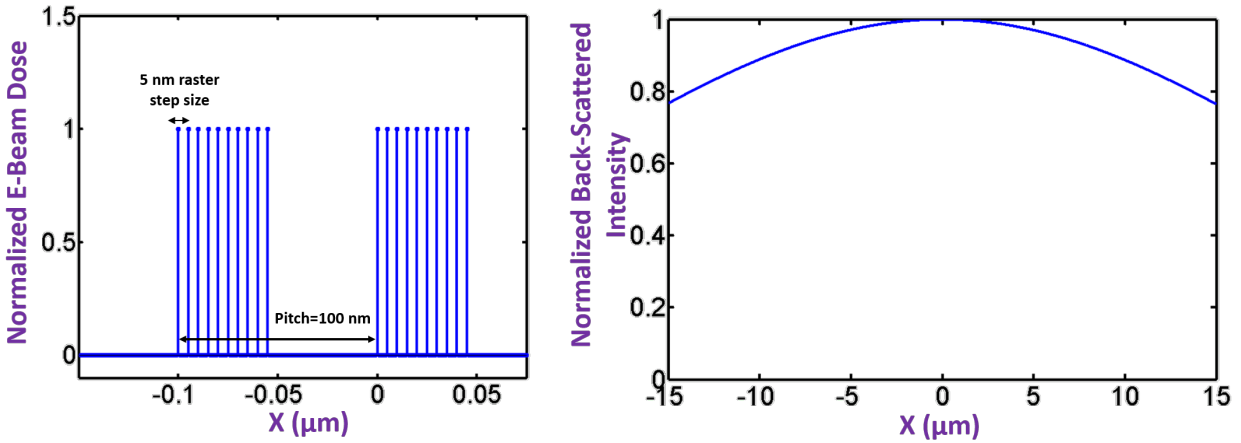
Figure 2.13: Proximity effect calculation in 100 keV e-beam lithography with silicon substrate; **(left):** 50 nm line/space beam write pattern with 5 nm raster scan step size; **(right):** Normalized back-scattered dose distribution assuming Gaussian back-scatter PSF with $\beta = 26$ μm

In addition to the spatial profile of the relative back-scattered dose contribution, the

actual magnitude of the dose is also important. In order to calculate the contribution from all source points in a 20 μm X 20 μm square to a point at the center of the square, we can analytically integrate the back-scatter PSF in equation 2.4. In order to account for the fact that we have line/space patterns with a 50% duty cycle, this integral can be simply scaled by 0.5X in order to estimate the back-scattered dose. The 2-D integral of the back-scatter PSF from equation 2.4 integrated radially from 0 up to a radius R is given by equation 2.5. The total back-scatter yield, η, has been approximated by Owen [20] to be 0.74 for 100 keV beam with silicon substrate. By using R = 14.1 μm (the half-diagonal of the 20 μm X 20 μm field) and assuming 50% duty cycle of lines and spaces, the back-scatter dose contribution is 5.4% of the incident electron dose at the center of the exposure field.

$$\int_0^R PSF_{backscatter}dxdy = \int_0^R \frac{1}{\pi}\frac{\eta}{1+\eta}\frac{1}{\beta^2}e^{-r^2/2\sigma_{BS}^2}2\pi r dr = \frac{\eta}{1+\eta}\Big[1 - e^{-R^2/\beta^2}\Big] \qquad (2.5)$$

2.7.2   Mask Contributions to LER in EUV Lithography

EUV masks consist of multilayer reflectors with absorber layers deposited in regions where no resist exposure is desired. Two of the major contributors to mask-induced LER are the surface roughness on the multilayer mirror and the line edge roughness on the absorber pattern itself, as described by Naulleau et. al. [7].

An extensive investigation of the mask contributors to aerial image LER as a function of numerical aperture (NA) and illumination conditions were reported in McClinton's PhD thesis [4]. In order to correct for mask-induced LER from the measured resist LER, we performed a calculation of the aerial image LER for 50 nm half-pitch line/space patterns for a range of defocus conditions by using a thin mask model [7]. The lithographic conditions in the simulation were picked to match the actual conditions used in the experiment.

Two separate simulations were performed. In the first simulation, the contribution of the multilayer surface roughness to LER was determined by using as an input mask, binary line/space patterns overlaid on the spatial phase roughness of the multilayer surface. The phase roughness was calculated from the surface roughness of a representative mask measured directly with atomic force microscopy (AFM), by using the relation: PR=2*2π/λ*SR, where PR represents the phase roughness that results from a mask with surface roughness (SR), and λ is the wavelength of EUV light (13.5 nm). Of all the various surface roughness data-sets from several masks available to the author, 100 pm rms surface roughness data was used to estimate phase roughness. As suggested by McClinton [4], this is the typical mask surface specification.

In the second simulation, contribution of the absorber LER to the image-plane LER was simulated by using as an input mask, a line/space pattern with the desired spectral properties, and no multilayer roughness. A 3σ absorber LER of 1.8 nm reported in the literature for a representative mask [7] was used, with a correlation length of 19 nm and a

roughness exponent of 0.7 [22]. The mask with these spectral properties was generated by using the LER synthesis tool included in the SuMMIT software toolset [23].

The resulting image-plane LER values for the aerial image are shown in Fig. 2.14. The total LER was calculated by adding the multilayer surface roughness and the absorber LER contributions in quadrature.
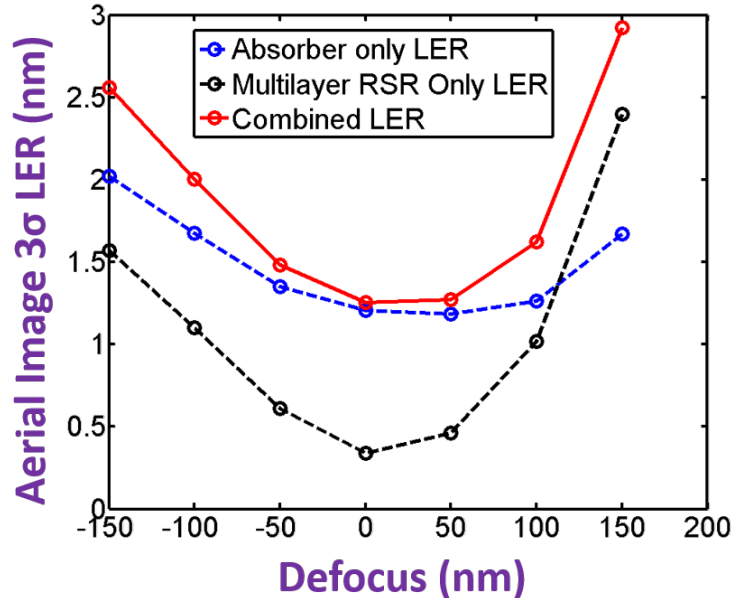
Figure 2.14: Image plane LER due to mask multilayer surface roughness and absorber LER

2.8 EUV/E-Beam Patterning Results

2.8.1 Experiment Conditions

EUV exposures of 50 nm half-pitch lines and space patterns were performed at the Berkeley MET (BMET), while the 100 keV e-beam exposures were performed at the Molecular Foundry at LBNL. The processing conditions are provided in table 2.3. SEM imaging was used as a technique for extracting the nano-scale LER values. Extraction of the nano-scale LER values was performed by using the SuMMIT LER analysis toolkit [23]. Considering that most of the LER is contributed by the lower frequency components in the power spectral denstiy of the edge deviations, the SEM working distance and magnification were chosen such that the lines in a single image were adequately long, while retaining a reasonable scan pixel size. The extracted correlation lengths for the data to be shown later are around 16 nm, thus the line lengths are about 50x the correlation length.

Table 2.3: Summary of parameters for lithography experiments

Parameter	Resist A	Resist B
Resist Thickness	45 nm	
Resist Post-Apply Bake	110° C / 90 s	130° C / 60 s
Resist Post-Exposure Bake	100° C / 90 s	110° C / 60 s
CD Analyzed	50 nm half-pitch	
EUV Illumination	Annular 0.35/0.55	
E-Beam Litho Pixel Size	5 nm	
E-Beam Litho Field Size	20 μm X 20 μm	
LER PSD Analysis Length	800	
SEM Imaging Energy	2.0 keV	
SEM Imaging Emission Current	2.0 μA	
SEM Imaging Working Distance	4.0 μm	
SEM raster scan pixel size	0.992 nm	

Example SEM images are provided in Fig. 2.15 for the two lithography techniques used on two resists. Resist A prints with a larger LER than resist B.
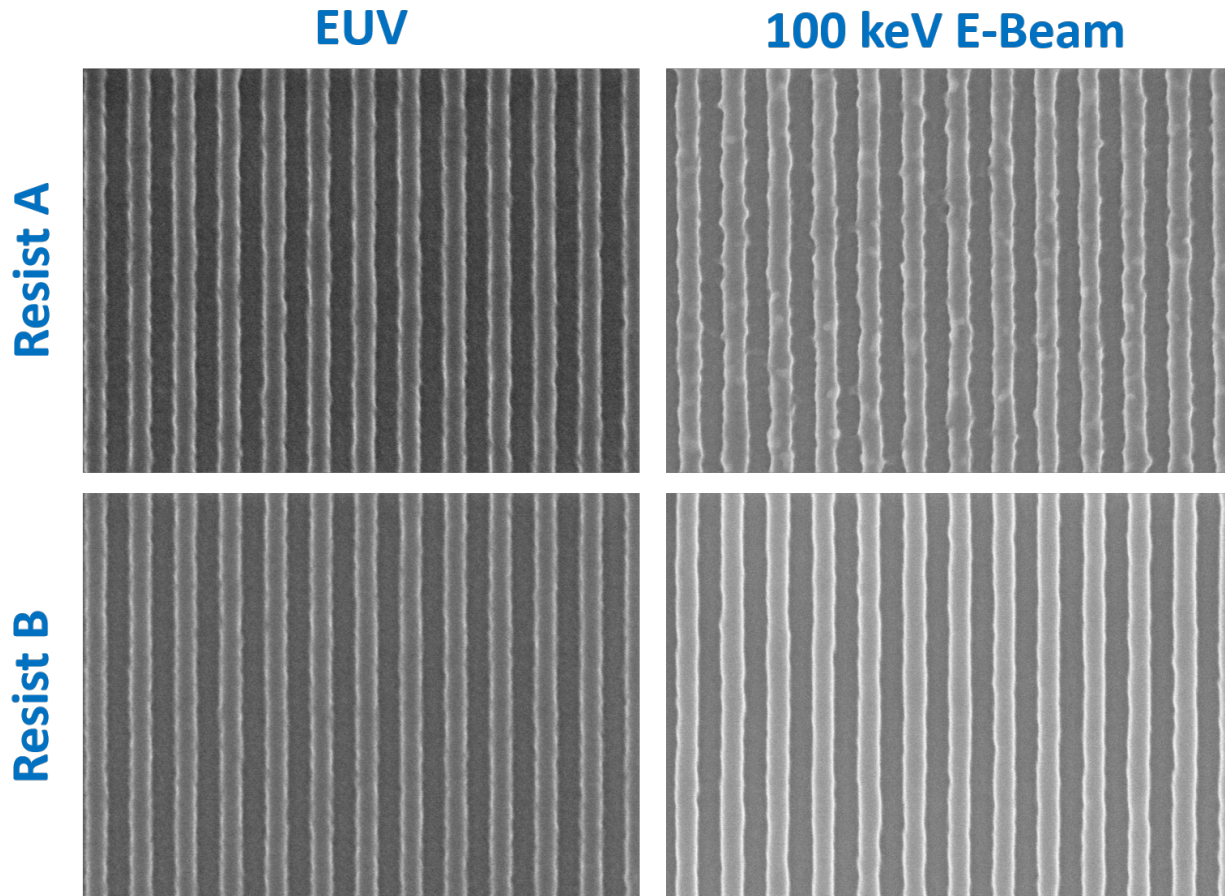
Figure 2.15: Example SEM images for 50 nm line/space patterns demonstrating LER for two EUV resists patterned with EUV and 100 keV e-beam lithography

2.8.2 Matching Lithographic Image Gradients between EUV and 100 keV E-Beam

2.8.2.1 Using Resist Exposure Latitude to Test Whether Image Gradients are Matched

Image log slope (ILS) of the intensity pattern incident on the resist (I(x)), calculated at the intensity threshold level where the target CD is achieved and defined by equation 2.6, inversely impacts the line edge roughness. For identical noise contributors, a larger image log slope results in a lower LER.

$$ILS = \frac{1}{I_{thr}} \frac{\partial I}{\partial x}\Big|_{I_{thr}} \tag{2.6}$$

The measurable parameter that directly relates to ILS is the exposure latitude of the patterns formed in the photoresist, which quantifies the perturbation in exposure dose needed to produce a given perturbation in printed linewidth (CD). For example, the exposure latitude that can be calculated assuming 10% perturbation of CD is shown in equation 2.7 [1].

$$ExposureLatitude(EL) = \frac{Dose(1.1 * CD_{nominal}) - Dose(0.9 * CD_{nominal})}{Dose(CD_{nominal})} \quad (2.7)$$

A simple demonstration of the relationship between the image log slope and the exposure latitude is provided in Fig. 2.16. A trend for the image log slope as a function of defocus for the wafer-plane aerial image for 50 nm line/space patterns simulated using a thin mask model and utilizing the imaging conditions for the Berkeley MET (BMET) is provided on the plot to the left in Fig. 2.16. The plot on the middle in the figure provides the experimentally measured exposure latitude in the resist image, calculated using the definition in equation 2.7 as a function of the defocus conditions. As shown on the plot to the right in Fig. 2.16, we clearly see a direct relationship between the exposure latitude and the ILS.
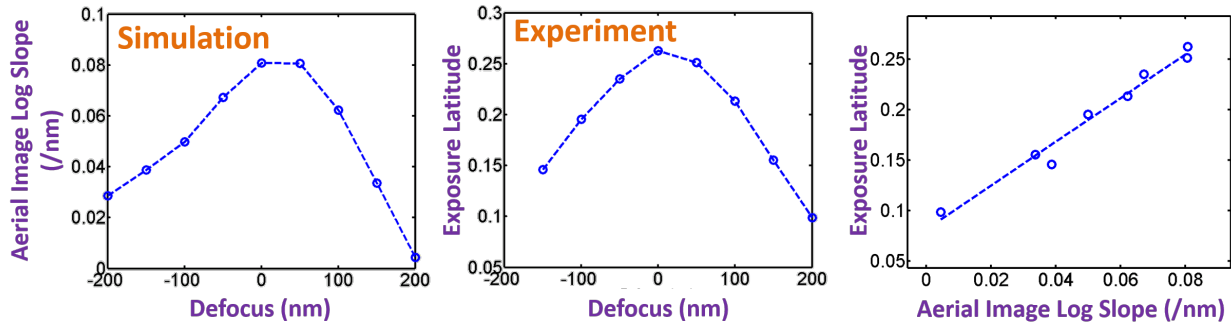
Figure 2.16: Demonstration of exposure latitude as a way of determining image gradients using 50 nm half-pitch line/space patterns as an example; **(left):** Simulated image log slope (ILS) vs. defocus; **(middle):** Experimental exposure latitude around best-dose; **(right):** Measured exposure latitude vs. simulated image log slope

The improvement in LER with increasing exposure latitude, corresponding to smaller offset from best-focus conditions, is demonstrated in Fig. 2.17 for two resists, where resist B prints with a higher dose than resist A.
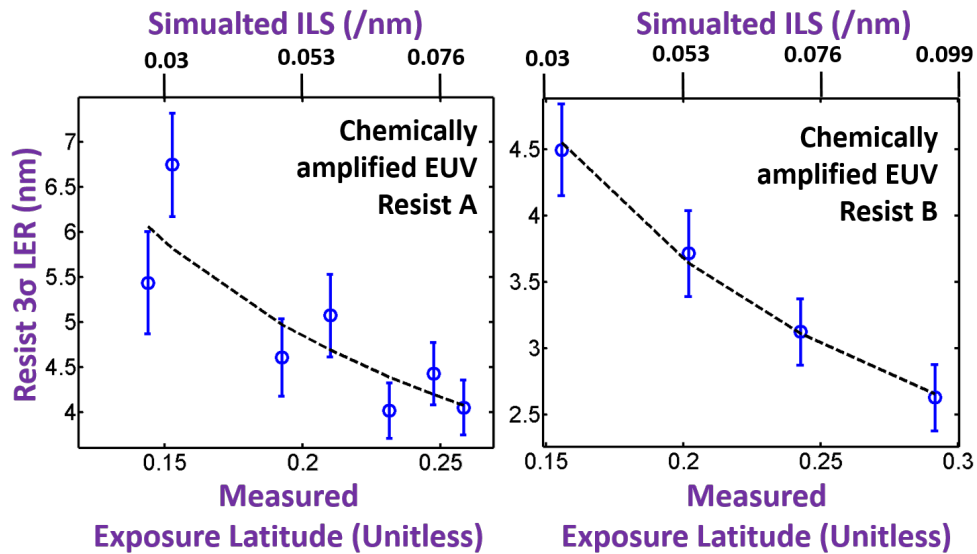
Figure 2.17: LER at dose to print 50 nm half-pitch lines/spaces vs. exposure latitude for 2 resists

2.8.2.2   Lithographic Results for EUV/E-Beam Matched Exposure Latitudes

The lithographic results demonstrating matched exposure latitudes between EUV and e-beam patterning for the first resist is shown in Fig. 2.18. The blue points represent the measured linewidth (CD) as a function of exposure dose. The black dashed lines going through the data points are linear fits. In each plot, the remaining two dashed lines were calculated by using the standard deviations of the linear fitting parameters introduced by uncertainties in measured CD for a given dose. The exposure latitude obtained with EUV lithography was found to be larger than that obtained with e-beam lithography, likely because the spot size of this particular e-beam tool was larger compared to the EUV imaging condition that was used. The exposure latitudes were therefore matched by defocusing the EUV image. In this figure, CD vs. dose for +150 nm defocus of EUV image is shown.
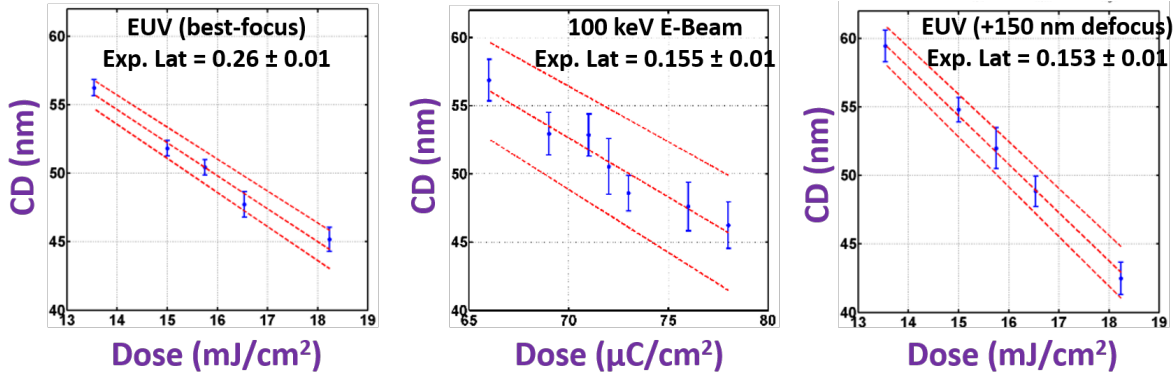
Figure 2.18: Exposure latitude of 50 nm line/space patterns; **(left):** EUV in-focus image; **(middle):** E-beam in-focus image; **(right):** EUV defocused image

For the second resist, the exposure latitude obtained with e-beam lithography (0.37) was larger than that obtained with an in-focus EUV image (0.29), as the resolution of the beam was improved after the exposures on the first resist. The exposure latitude here was matched by slightly degrading the e-beam image gradient, by programming a gray-scale pattern for dose delivered at each pixel, instead of a binary one. Overview of the technique was presented earlier. The dose pattern was calculated by deconvolution of the e-beam PSF from the desired EUV aerial image intensity pattern. The aerial image was computed by using an existing MATLAB based software that is capable of modeling partially coherent illumination conditions [7]. The Berkeley MET (BMET) model for illumination conditions accounting for aberrations present in the system were used in the simulation. The e-beam PSF was assumed to be a Gaussian function with a full-width at half maximum of 8 nm, that matches the CXRO tool. A demonstration of the calculation is shown in Fig. 2.19. The two images on the top correspond to the normalized e-beam doses for both binary as well as gray-scale scenarios. Only one period of the line/space feature is shown so that the varying colors in the gray-scale write pattern corresponding to spatially varying e-beam dose are easily visible. The bottom two images are the formed images. We can see qualitatively that the gray-scale pattern results in a degraded image contrast. The plot to the right in the figure shows a comparison of the image cross-sections for EUV, gray-scale e-beam and binary e-beam. The EUV aerial image and the e-beam image computed with the designed gray-scale input pattern both result in idential aerial images as expected.
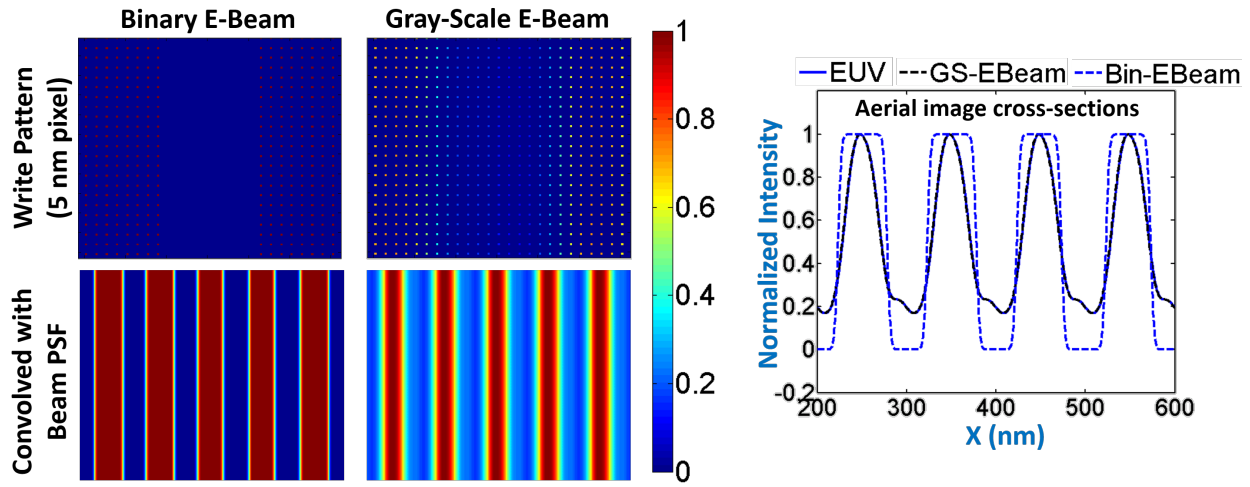
Figure 2.19: Demonstration of the gray-scale e-beam dose patterns for matching EUV and e-beam aerial images

In real patterning experiment with the computed gray-scale pattern however, it was found that EUV image had to be defocused by 50 nm in order to match the e-beam exposure latitude. The point spread function for the Molecular Foundry e-beam tool likely had a slightly larger full width at half maximum compared to the CXRO tool, which was used during the deconvolution process. The results for the second resist are shown in Fig. 2.20.
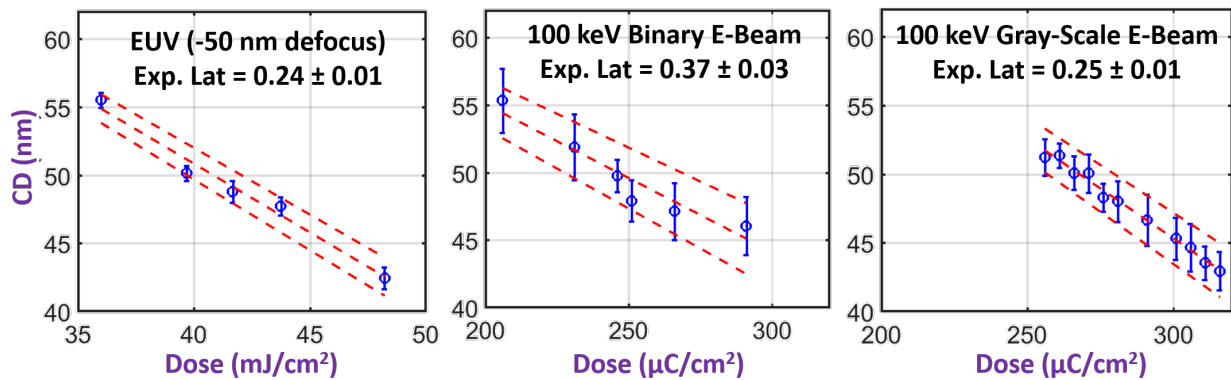
Figure 2.20: Exposure latitude of 50 nm line/space patterns; CD vs. dose for **(left):** EUV image defocused by 1 focus step; **(middle):** Binary e-beam image pattern; **(right):** Gray-scale e-beam image pattern showing close match in exposure latitude with EUV

Example SEM images that show patterning comparisons between binary and gray-scale techniques at the dose needed to pattern the target linewidth of 50 nm are shown in Fig.

2.21. The LER values have been annotated. Image formed with binary write pattern results in a lower LER than gray-scale patterning due to a larger exposure latitude.
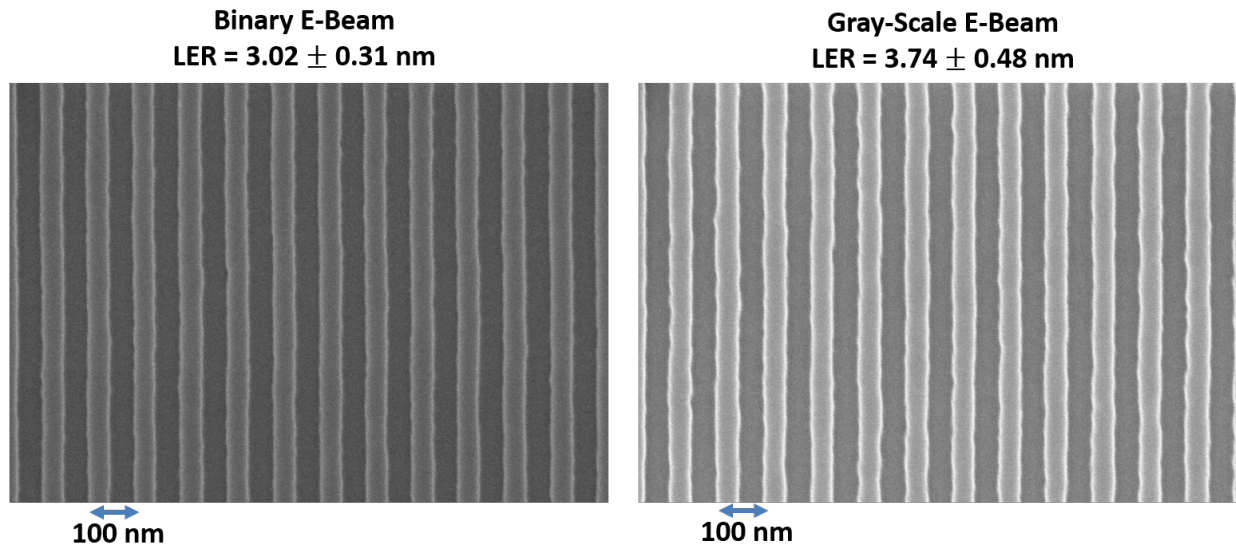
Figure 2.21: SEM images of a chemically amplified EUV resist patterned using binary **(left)** and gray-scale **(right)** e-beam techniques

2.8.2.3   Analyses of LER with Matched Exposure Latitudes

The statistics of measured 3σ LER for both of the resists are shown in Fig. 2.22. For resist A, the LER values measured three focus steps (150 nm) away from the best focus on each side were used to plot the statistics that have been provided. As shown in the plot on the middle in Fig. 2.16, both of these defocus conditions result in exposure latitude that closely matches the e-beam exposure latitude. When plotting the distributions, the individual mask contributions for each focus that were previously demonstrated were first subtracted. The LER distributions for resist A are found to have a larger overlap than for resist B.
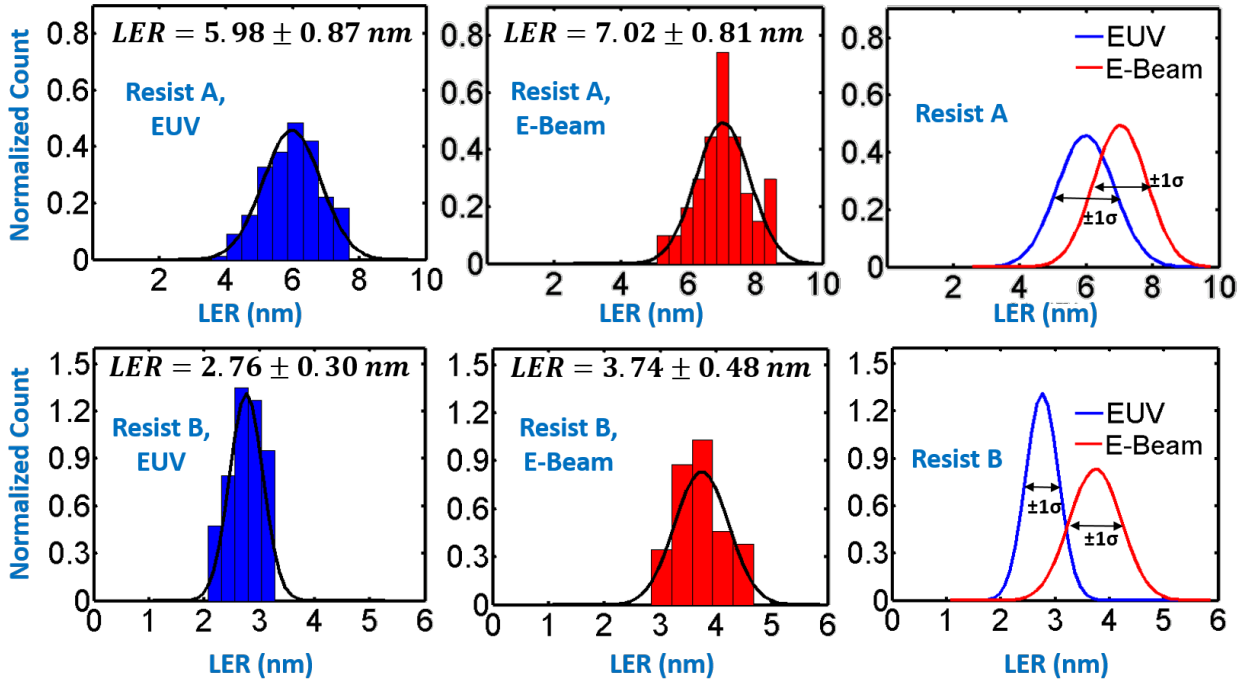
Figure 2.22: Comparison of EUV/E-Beam LER statistics; **(top):** Data for resist A; **(bottom):** Data for resist B; **(Left):** EUV; **(middle):** E-Beam; **(right):** Gaussian fit functions

Summary of the shot noise numbers are provided in tables 2.4 and 2.5. For both the resists, we see that the absorption probability is larger for 100 keV e-beam compared to a 92 eV EUV photon. The incident particle flux values have been computed simply from the dose values. The probability of absorption of 100 keV electrons is larger than that of 92 eV photons. However, we find that this discrepancy is almost exactly canceled by a scaling of the the dose needed to print roughly equal linewidths, as reflected in the absorbed particle flux values shown in the tables. These results show that this technique did not help with creation of a significant difference in absorption flux as had been originally intended. A possible reason is that either the secondary electron spectra created in the material through ionization events are similar for EUV and 100 keV e-beam exposures, or that there are only small differences which ultimately do not matter from the standpoint of acid generation statistics. The data however, does show that both the resists result in larger LER when exposed with e-beam compared to EUV radiation, which suggests there may be other contributors to formation of roughness in e-beam lithography.

Table 2.4: Lithography and absorption shot noise data for resist A

Parameter	EUV	100 keV E-Beam
CD	51.04 ± 1.21 nm	51.74 ± 1.54 nm
Dose to size	15.75 mJ/cm^2	71 $\mu C/cm^2$
Incident Particle Flux	10.7 photons/nm^2	4.44 e$^-$/nm^2
Absorption Probability	0.17	0.402
Absorbed Particle Flux	1.82 photons/nm^2	1.78 e$^-$/nm^2

Table 2.5: Lithography and absorption shot noise data for resist B

Parameter	EUV	100 keV E-Beam
CD	49.55 ± 0.55 nm	49.38 ± 1.22 nm
Dose to size	39.69 mJ/cm^2	266 $\mu C/cm^2$
Incident Particle Flux	27 photons/nm^2	16.63 e$^-$/nm^2
Absorption Probability	0.22	0.38
Absorbed Particle Flux	5.94 photons/nm^2	6.32 e$^-$/nm^2

2.9   Summary

There are several material contributors to noise formation in an EUV photoresist. In this chapter, a new approach of comparative analysis of EUV and e-beam lithography performance for experimental investigation of the influence of absorption count statistics on LER was tested. The probabilities of scattering of 92 eV photons and 100 keV electrons were measured, using reflectometry for EUV lithography and electron energy loss spectroscopy (EELS) for 100 keV e-beam lithography. From the results it was learned that despite having access to core energy levels in the resist (e.g., 284 eV ionization edge due to carbon), 100 keV electrons mostly excite only the valence band, and lose on average only about 35 eV in a resist film. The probability of absorption for 100 keV e-beam was determined to be 2.36x larger than for EUV photons for resist A, and 1.73x for resist B. In the lithography experiments however, these discrepancies in absorption probabilities almost exactly canceled out by a scaling of the incident dose needed to print 50 nm half-pitch lines and spaces. These results suggest that the secondary electron spectra in the resist are similar enough so as to not result in a discrepancy in the acid generation statistics, considering that the volumetric density of acids needed to print a given feature has to be similar between the two techniques. Furthermore, it was observed that with the same absorption density between EUV and e-beam patterning, the electrons lose only 35 eV on average while the photons lose 92 eV. This suggests that lower energy electrons induced by the electrons are more efficient at triggering chemistry. With matched exposure latitudes and roughly equal absorption count however,

e-beam lithography resulted in a larger mean LER than EUV lithography, which suggests the likely presence of other contributors to LER in e-beam lithography.

Chapter 3

EUV Resist Shot Noise: Modeling Study

In this chapter, a stochastic resist simulator is used to study the role of a few material contributors to the overall LER in relation to the LER contributed by absorption count alone. The great advantage of using simulation models is that it enables us to assess the influence that a given parameter has on the final outcome of a physical process. In the context of LER in particular, we can turn on one source of randomness at a time to better understand the role each source of randomness plays in determining the final LER. The challenge however, is in picking realistic parameters that result in a close match between simulation and experimental data. In the next section, an overview of a resist simulator that models chemical image formation mechanisms in a probabilistic manner, will be provided. Then, the approach used for fitting the simulation model parameters to lithographic data will be presented. Subsequently, contribution of the dominant material intrinsic sources in determining resist LER will be provided.

3.1 The Stochastic Resist Simulator

The stochastic resist simulation framework known as SuMMIT has been previously described in the literature [24][25][26]. The simulator is capable of taking into account the major mechanisms that govern chemical image formation in chemically amplified resists. Chemical species that can be loaded in the resist in simulation are photo-acid generators (PAGs), base compounds and the polymer protecting groups. The simulator implements models for initial events consisting of photon absorption and excitation of photo-acid generators (PAGs) to produce acids. The acids diffuse during the post-exposure bake and participate in catalytic de-protection reactions in the polymer, as well as neutralization reactions with base compounds. The neutralization reaction mechanisms in the resist help with improving image gradients at the line edge because acids crossing the edge from the exposed areas to unexposed areas get effectively quenched by the base compounds. The trade-off however, is that base compounds also consume acids in the exposed regions which has the effect of increasing the dose needed to print a given feature, all other resist parameters being equal.

Table 3.1: Sources of randomness and what they model

Source of randomness	What it models
Absorbed photon	Shot noise
Quantum efficiency	Acid generation statistics
Photo-acid generator loading	Randomness of number densities
Base loading	Randomness of number densities
Protecting group loading	Randomness of number densities

A major strength of the model is its capability of solving the coupled reaction/diffusion system characteristic of the bake process in small time increments [24], instead of treating the resist image as a simple convolution with a guess of the mathematical description of the chemical point spread function. Another strength of the simulator is its ability to model discrete aspects of the overall imaging process, and treating the intial exposure processes in a probabilistic manner. This allows for predicting the limits imposed by counting statistics on LER. The model allows for studying the impact of five major material intrinsic sources of randomness in resist LER. A summary of each source of randomness is provided in table 3.1. Randomness applied on absorbed photon image models shot noise effects. Randomness applied on the quantum efficiency parameter models the fact that interactions between electrons produced by an absorption event and the PAGs may lead to generation of a random number of acids. Randomness applied on the chemical species in the system, i.e. PAGs, base compounds and protecting group concentrations simply makes the occupancy of each species in a given voxel a statistical parameter.

An approximation that is used in the simulator is that it is a 2-D model, and the imaging operations involved in the reaction/diffusion step are performed on 2-D matrices that describe the number of chemical species within a voxel whose volume is: $V_{voxel} = \Delta x * \Delta y * r_t$. Here, Δx and Δy are the 2-D pixel dimensions, and r_t is the thickness of the resist. This makes the simulator faster in comparison to a full 3D simulator. The impact of this approximation is that the simulated linewidth and LER values are really thickness-averaged parameters. This is however okay because measurements of these parameters from common imaging technique like scanning electron microscopy (SEM) are also thickness-averaged. Furthermore, the impact of resist roughness on electrical performance of devices is also an average along the thickness dimension.

3.1.1 Initial Exposure Events

The initial exposure events modeled by the simulator include photon absorption and acid generation statistics. Photon absorption is modeled by using the Beer-Lambert model shown previously in equation 2.3. Photo-electrons and secondary electrons created by an absorption event traverse trajectories in the material governed by laws of scattering, and electrons with

various energies may be more or less efficient at triggering the acid generation chemistry. In this simulator, these effects are not accounted for, and movement of the electrons is modeled simply by convolving the absorbed photon image with a blur function. This convolution kernel represents the spatial extent relative to the photon absorption site, over which photo-electrons and subsequent secondary electrons may create acids. Creation of acids can be treated with first-order kinetics using Dill's equations, a summary of which is provided by Mack [1]. The end results is summarized in equation 3.1. This same model is used for modeling the PAG excitation events triggered by the electrons produced by absorbed EUV photons. Here, Φ is the quantum efficiency, and $[p_{abs}]$, $[PAG]_{reacted}$, $[PAG]_0$, and [Acids] are the volumetric number densities of absorbed photons, PAGs that have reacted, initial PAG density, and the generated acids, respectively.

$$
\begin{aligned}
[PAG]_{reacted} &= [PAG]_0 * e^{-\Phi*[p_{abs}]/[PAG]_0} \\
[Acids] &= [PAG]_0 * (1 - e^{-\Phi*[p_{abs}]/[PAG]_0})
\end{aligned}
\tag{3.1}
$$

3.1.2 Reaction/Diffusion Process During Bake

3.1.2.1 Assumptions about Diffusion and Reactions

Diffusion of acids and bases is assumed to be Fickian, i.e. the diffusivity is constant as a function of bake time. However, there is some evidence for the presence of non-Fickian diffusion that may need to be accounted for in the future. For example, Hinsberg et. al. [27] estimated that the diffusivity of acids in regions of the polymer where majority of the protected groups were intact was around 2 orders of magnitude larger than in regions where majority of these groups had already been de-protected by an acid. Yuan [28] formalized the distinction between ehanced non-Fickian (ENF) diffusion and reduced non-Fickian (RNF) diffusion. ENF corresponds to the mechanism where the diffusivity in a given environment is larger than the Fickian case, while RNF corresponds to the mechanism where the diffusivity in a given environment is smaller than the Fickian case. Mathematically, these mechanisms were captured by the model for diffusivity given by: $D = D_o e^{\omega A}$. Here, A represents the de-protection level within a given volume in the resist. D_o and ω are fit parameters, with $\omega = 0$ resulting in Fickian diffusion. The author also devised a double exposure based test pattern to accurately estimate the type of diffusion in two chemically amplified resists. The RNF mechanism was found to best describe the empricial data on corner-to-corner spacing vs. trench width estimated using SEM imaging. Croffie et. al. modeled the impact of free volumes on diffusivity of acids in resists [29]. The de-protection reactions between acids and the protected t-BOC groups in the polymer result in the formation of volatile byproducts. These byproducts leave behind transient free volumes, which ultimately result in relaxation of the polymer matrix with a given time constant. This mechanism might impact the diffusivity of acids, however it is not implemented in the model here.

The simulator assumes that the deprotection reactions do not result in consumption of the acids. The only mechanism for acid loss includes interactions with the base. Additionally, the effects associated with interactions of weak acids is not considered. Nagahara et. al. [30] and Yuan [28] showed that non-flourinated sulfonic acids tend to behave as weak acids in organic solvents, which required developing a model for dissociation of weak acids.

3.1.2.2 The Model

The coupled reaction/diffusion equations that govern the processes that occur during the bake step are summarized in equation 3.2 [1][24]. Here, [A] is the number density of acids, [B] is the number density of base compounds loaded in the resist, [P] is the number density of the protected (tert-butoxycarbonyl, t-BOC) groups in the polymer, [D] is the number density of the de-protected sites, and [p] is the net fraction of t-BOC sites in the polymer that get de-protected due to interactions with an acid. The reaction/diffusion parameters are D_A, which is the diffusivity of acid, D_B, the diffusivity of base, k_{AB}, the rate constant for acid/base neutralization reaction, and k_D, the rate constant for the de-protection of a protected site in the vicinity of an acid. The acid/base neutralization reaction results in the consumption of acids and bases, thus the negative terms on the right hand sides of the d[A]/dt and d[B]/dt equations.

$$\frac{d[A]}{dt} = D_A \nabla^2 [A] - k_{AB} * [A] * [B] \tag{3.2a}$$

$$\frac{d[B]}{dt} = D_B \nabla^2 [B] - k_{AB} * [A] * [B] \tag{3.2b}$$

$$\frac{d[P]}{dt} = -k_D * [A] * [P] \tag{3.2c}$$

$$[D] = [P]_0 - [P] \tag{3.2d}$$

$$[d] = 1 - [P]/[P]_0 \tag{3.2e}$$

Numerically, the system in equation 3.2 is modeled by splitting the total bake time into N steps, where N is determined by the bake time and the bake time step size. For each step, the acids and bases are allowed to first diffuse by a small amount to a reaction site, and then letting the deprotection and neutralization reactions occur. The number densities of acids, bases and protecting groups available for reactions and diffusion in time iteration i+1 relative to the number available at iteration i are described by equation 3.3. Here, Δt is the specified bake time step size.

$$\begin{aligned}
[A]_{i+1} - [A]_i &= -k_{AB} * [A]_i * [B]_i * \Delta t \\
[B]_{i+1} - [B]_i &= -k_{AB} * [A]_i * [B]_i * \Delta t \\
[P]_{i+1} - [P]_i &= -k_D * [A]_i * [P]_i * \Delta t
\end{aligned} \tag{3.3}$$

The diffusion steps are not modeled as a random walk procedure that might assign a randomized path length and directionality to the acids and bases that traverse the resist and participate in various reactions. Instead, the diffusion is modeled as a convolution with a Gaussian kernel. For each step, the acid and base diffusion lengths are $\sigma_{step}=\sigma_{Tot}/\sqrt{N}$, where $\sigma_{Tot} = \sqrt{(2*D*t_{PEB})}$ is the total Fickian diffusion length expected at the end of the bake, D being the diffusivity at a given temperature. Example of an acid blur function for a PEB time step from a simulation is provided in Fig. 3.1. In this simulation an acid blur of 10 nm over a 90s time was used, with a reaction/diffusion time step of 1 s. The reaction rate constants are specified in the simulator in units of nm^3/s, and are normalized by the voxel size internally in the simulator when using them in equations 3.3.
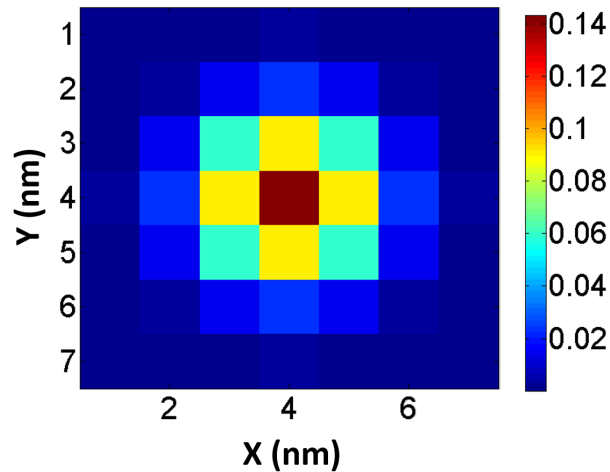
Figure 3.1: An example acid blur function used for convolutions in a PEB time step size of 1 s

3.2 Reaction/Diffusion Kinetics Parameters

With the goal of measuring the reaction/diffusion kinetics parameters for chemically amplified photoresists, Hinsberg et. al. [27] devised an experimental technique, where open frame exposures were done with 193 nm and 254 nm wavelength photons. With 254 nm light exposing a weakly absorbing film, the authors created a uniform distribution of acids throughout the resist thickness, while with 193 nm wavelength they created a thin acidic layer on the top surface. For each scenario, the authors measured the depletion of t-boc protecting groups due to the deprotection reactions triggered by diffusing acids by monitoring its characteristic absorption in the IR regime during the bake process. A stochastic model for reaction kinetics was then used to find the best fit rate constants that matched the measurement results for the case of uniform distribution of acids created with the 254

nm exposure experiment. With the data for 193 nm exposures containing acidified layer on the top surface, the authors performed a fit of the diffusivity of the acids. The experiments were performed with two different types of acids, and the widely used tert-butoxycarbonyl (t-boc) as the protecting group in a polyhydroxystyrene (PHOST) polymer backbone. The authors highlighted an important point that the temperature dependent diffusivity of acids in the resist film is a strong function of the shape and size of the acid itself, as well as the local polymeric environment that the acid is in. In particular, strong differences were seen for two different families of PAGs [27] with identical polymeric environment. The authors suggested that the diffusivity of acids in an environment where most of the protected sites in the polymer have already been deprotected is different by up to two orders of magnitude from the diffusivity in an environment where most of the protected sites are still intact. The implication of this result is that the diffusivity of the acid can change as a function of bake time. Houle et. al. [31] followed up, and showed that two environment-sensitive (deprotected vs. protected) diffusivities were needed to best fit the measured deprotection level vs. bake time data. While using the two diffusion paths provided a closer match between simulation and experiment, the relative difference between the two diffusion models were well within 10% at a bake temperature of 95 ^{o}C (Fig. 3 in [31]).

As for the deprotection reaction rates (k_D in equation 3.2), Hinsberg et. al. [27] found that the rates for two different PAGs in identical polymer environment that were studied were different by 40%. Houle et. al. also investigated the rate constant for acid/base reactions (k_{AB} in equation 3.2) in a chemically amplified resist through a combination of experiment and stochastic modeling of the reaction/diffusion mechanisms [32]. At a temperature of 100°C, they predicted a rate constant of k_Q=6 liters/(mole*s), which translates to an acid/base neutralization rate of 10 nm^3/s. However, the reported uncertainty on this number is a factor of 2.

3.3 An Example Simulation Flow

The chemical compounds that are a part of resist formulations are specified as volumetric densities (#/nm^3), and the imaging operations (e.g., reaction/diffusion processes during the bake step) are performed on 2D matrices, which represent the number of chemical species contained in a voxel with a volume of $\Delta x * \Delta y * r_t$, where r_t corresponds to the thickness of the resist and Δx and Δy correspond to the pixel size in x and y dimensions respectively. As an example, spatial distribution of photo-acid generators that may be used in a simulation is shown in Fig. 3.2. A volumetric density of 0.2/nm^3, a pixel size in x/y dimension of 1 nm, and a resist thickness of 45 nm is assumed in this example. Statistical nature of the number of chemical species in a given volume element in the resist is accounted for by applying Poisson statistics on mean volumetric densities.
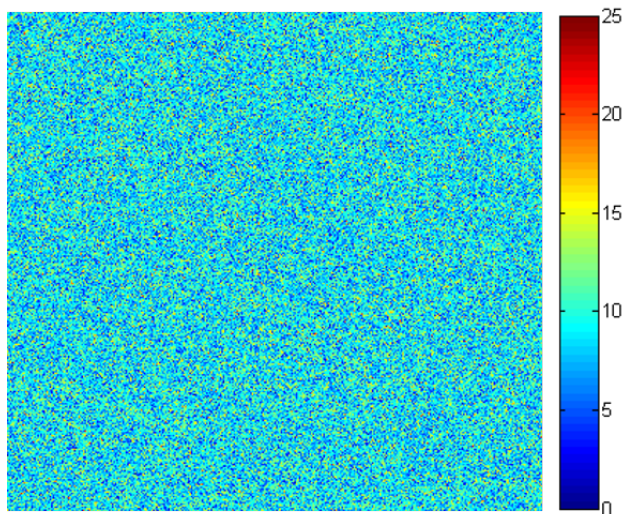
Figure 3.2: An example of the spatial distribution of photo-acid generator molecules

Diagrammatic summary of a typical simulation flow is demonstrated in Fig. 3.3. The aerial image is computed by using an existing MATLAB based software that is capable of modeling partially coherent illumination conditions [7]. The aerial image shown in Fig. 3.3 was calculated using the Berkeley-MET (B-MET) model for illumination conditions accounting for aberrations present in the system. This aerial image is provided to the resist simulator, which then computes the absorbed photon count at each pixel, and subsequently implements the initial exposure events to compute the acid distribution. The acid distribution then enters the reaction/diffusion process step, during which time some of the acids lead to deprotection of the protected t-BOC sites in the resist, which ultimately become soluble in a base solvent.
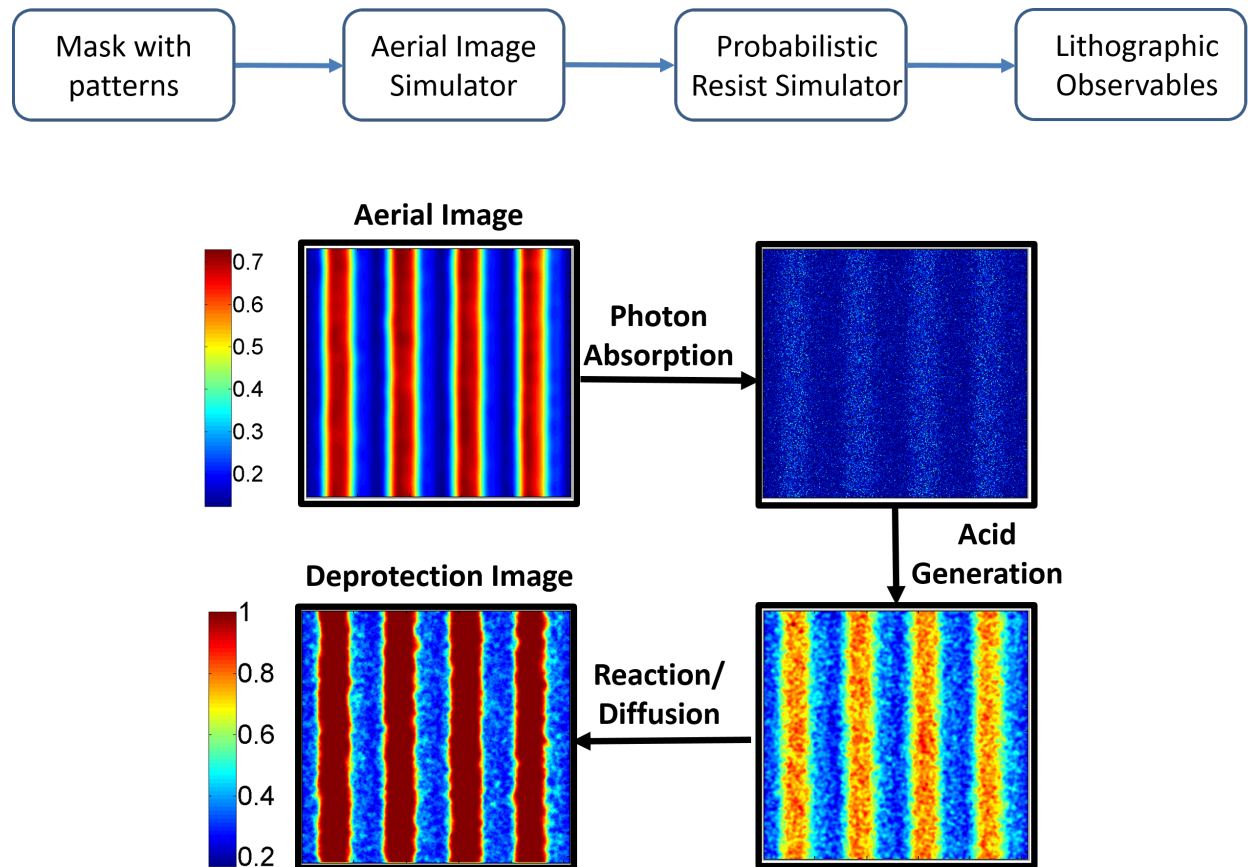
Figure 3.3: SuMMIT resist simulation flow; **(top left):** Wafer-plane aerial image; **(top right):** Absorbed photons; **(bottom right):** Acids created by absorbed photons; **(bottom left):** Spatial map of de-protection densities at the end of the reaction/diffusion process

3.4   Calibration of the Model to Data

In order to quantify the role of various contributors in determining the final resist LER, it is important to first calibrate the model parameters to empirical data. Due to the fact that the resist has many parameters, we need to hold constant the parameters that can either be measured through other means, or can be estimated through data in the literature. In this project, emphasis was placed on calibrating the reaction rate constants and the acid diffusion length during a 90 s bake at 100°C. The input diffusion parameters in the simulator correspond to the net diffusion over a given bake time. The Fickian diffusivity can be obtained from the numbers shown later with the relation: $\sqrt{2Dt_{PEB}} = \sigma_T$.

A summary of baseline resist parameters and how they are determined, is provided in table 3.2. The four measured parameters are the dose needed to pattern 50 nm half-pitch

Table 3.2: Baseline resist parameters

How Determined	Parameter	Value
Measured	E_{size} (50 nm half-pitch)	15.45 mJ/cm^2
	Dose-to-clear (E_o)	8.12 mJ/cm^2
	Resist Thickness	45 nm
	Photon Absorptivity	4.13 μm^{-1}
Approximation from Typical Values	Quantum Effiency	2 acids per absorbed photon
	Secondary electron range	3 nm
	PAG loading	0.4/nm^3
	Base loading	0.04 /nm^3
	σ_{Base} (100°C, 90s)	5 nm
Swept/Fit	σ_{Acid} (100°C, 90s)	
	Deprotection Rate (k_D)	
	Acid-Base Quenching Rate (k_Q)	
	Threshold deprotectoin level	

features (E_{size}), the dose to clear a 45 nm thick resist (E_o), the resist thickness used in the experiments, the absorptivity of the resist for 13.5 nm light measured using EUV reflectometry, and the bake time. The parameters that were not directly measured, but were estimated are the quantum efficiency, the electron blur and the number densities of photo-acid generators (PAGs) and the base. The quantum efficiency, defined as the number of acids generated by an absorbed photon, was approximated as the generally accepted value of 2. The secondary electron range was set to a value of 3 nm, and is close to the value of 2.4 nm suggested by Biafore et. al. [33]. The number densities of photo-acid generator (PAG) and the quenchers were chosen based on typical values. A PAG density of 0.4/nm^3 was assumed, while the base loading was assumed to be 10% by volume of the PAG loading. A resist with polyhydroxystyrene (Mw=120g/mol) backbone with a density of 1.2g/cm^3 has (1.2 g/cm^3)/(120 g/mol)*(6.02*10^{23} molecules/mol) = 6.02 monomer molecules/nm^3. A PAG loading of 0.4/nm^3 therefore translates to a loading of 6.25% by volume, a reasonable number.

The four reaction/diffusion parameters consist of the diffusion lengths of acid and base, the deprotection reaction rate constant and the acid/base neutralization rate constant. Houle et. al. [32] and Hinsberg et. al. [27] suggested that the base compounds due to their size, are expected to diffuse small distances if at all, and found that fitting their deprotection level measurement data did not require having a non-zero base diffusivity. In this work, the base diffusion length was set to a small magnitude of 5 nm.

3.4.1 Calibrating with Resist Contrast Curves

Gronheid et. al. [34] used an existing resist simulator to fit the reaction rate constants to resist thickness loss data obtained from open frame exposure experiments. Subsequently, the authors performed a fit of the diffusion parameters by using patterned line/space data measured using a scanning electron microscope. Here, a similar strategy was used. Line/space patterning data for resist A were presented in chapter 2. Thickness loss in the resist as a function of exposure dose can be measured after the bake step and the dissolution step to obtain the dissolution contrast curve. The contrast curve measured by exposing the resist with EUV light is provided in Fig. 3.4. Post exposure bake temperature of 100^oC and a bake time of 90 seconds were used for this experiment. The wafer was developed in TMAH for 30 s, and rinsed with de-ionized water for 30 s. In the transition region, the thickness loss trend is expected to be linear in logarithmic dose. Therefore, a linear fit was performed to estimate the dose to clear the full resist thickness. A value of 8.12 mJ/cm² was obtained, as annotated in the plot.
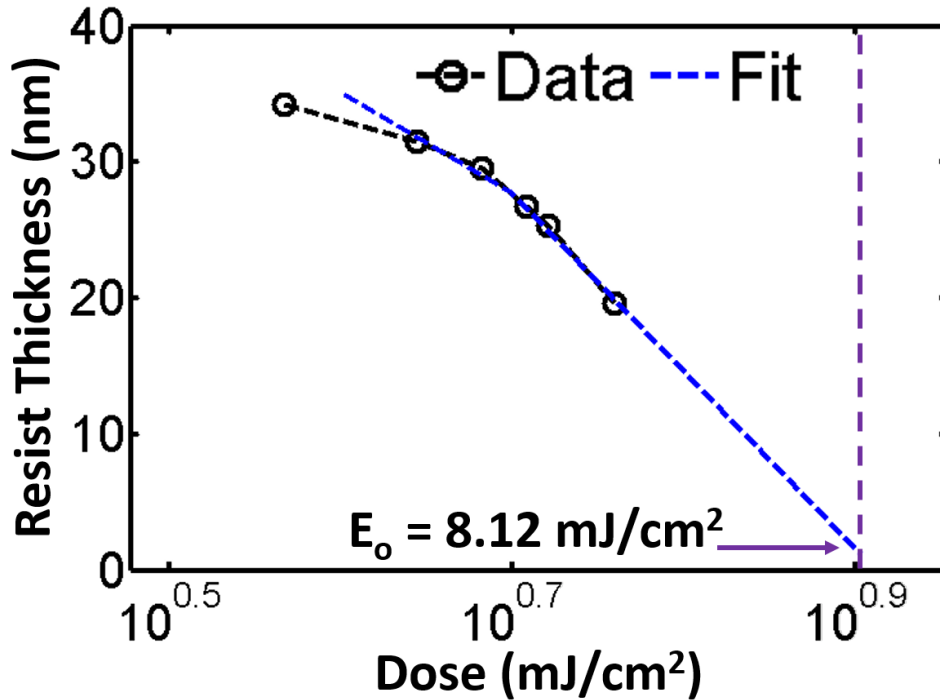
Figure 3.4: Contrast curve for open frame exposures of resist A

The contrast curve describes the dissolution rate, which depends on the relative volumetric concentration of de-protected sites in the resist that form as a result of exposure [35]. There is a simplified model for dissolution, which suggests that if a critical fraction of all

the protected sites within a volume is de-protected, then that volume becomes soluble in the developer. Considering that here dissolution processes are not modeled, this simplified model was used to determine whether a given region of the resist with a certain de-protection level would be considered soluble in simulation. Simulations were performed for deprotection threshold values of 0.3 and 0.5. In addition to the deprotection level, sweeps of the acid/base neutralization rate constant were also performed. For each neutralization rate constant and deprotection level, the best fit deprotection rate constant was determined through a least squares error minimization procedure performed with an optimizer in MATLAB.

The fitting procedure used by Gronheid et. al. [34] resulted in a deprotection rate constant of roughly 0.45 nm^3/s at 100 ^{o}C. In the optimization process, this value was used as an initial condition. A lower bound of 0.01 nm^3/s and an upper bound of 30 nm^3/s were used. The error metric given in equation 3.4 was provided as the objective function to the optimizer. This metric simply evaluates the fractional error in experimental dose-to-clear (E_o), and the simulated E_o. In order to evaluate E_o in simulation, the deprotection levels for an open frame exposure were calculated over a range of dose values. A linear interpolation was then performed to obtain the dose at which the critical threshold for development was reached. There is some guidance in the literature for determining the relative ratios of the deprotection and the acid/base neutralization rate constants. Measurements performed by Jung et. al. [36] showed that for temperatures up to 120°C, the acid/base neutralization rate constant (k_{AB}) is expected to be larger than the deprotection rate constant (k_D). Sweep range of the acid/base neutralization rate constant here were chosen to fall within the range of uncertainty of the value of 10 nm^3/s reported by Houle et. al. as described earlier.

The best fit parameters resulted in the simulated dose to clear for each scenario to match with experimental value of 8.12 mJ/cm^2 to within 1%. A plot of the best fit deprotection rate constant for a range of acid/base neutralization rate constants is provided on the top left in Fig. 3.5. The same data plotted as a function of the deprotection threshold is provided on the top right. All other resist parameters being equal, as the neutralization rate constant goes up, in each time step of the bake cycle the amount of acids lost goes up. Therefore, the deprotection rate constant required to achieve a given deprotection level goes up as seen in the plot on the top left. Similarly, increasing the threshold deprotection level for dissolution results in an increase in the de-protection rate constant as seen on the plot on the top right. The trend was also normalized to produce the plot shown on the bottom left, which shows the relative increase in the deprotection rate constant as a function of the relative increase in the neutralization rate constant. A 4X increase in the neutralization rate constant resulted in around 3X increase in the deprotection rate constant. Plot on the bottom right shows ratio of the neutralization rate constant relative to the deprotection rate constant. For the neutralization rate constant values that were chosen, a deprotection threshold of 0.3 shows relative ratios larger than 8, however it has a downward trend with decreasing neutralization rate constant near the smallest neutralization rate constant used in the simulations here.

$$Error = \frac{|Eo_{simulated} - Eo_{experiment}|}{Eo_{experiment}} \tag{3.4}$$
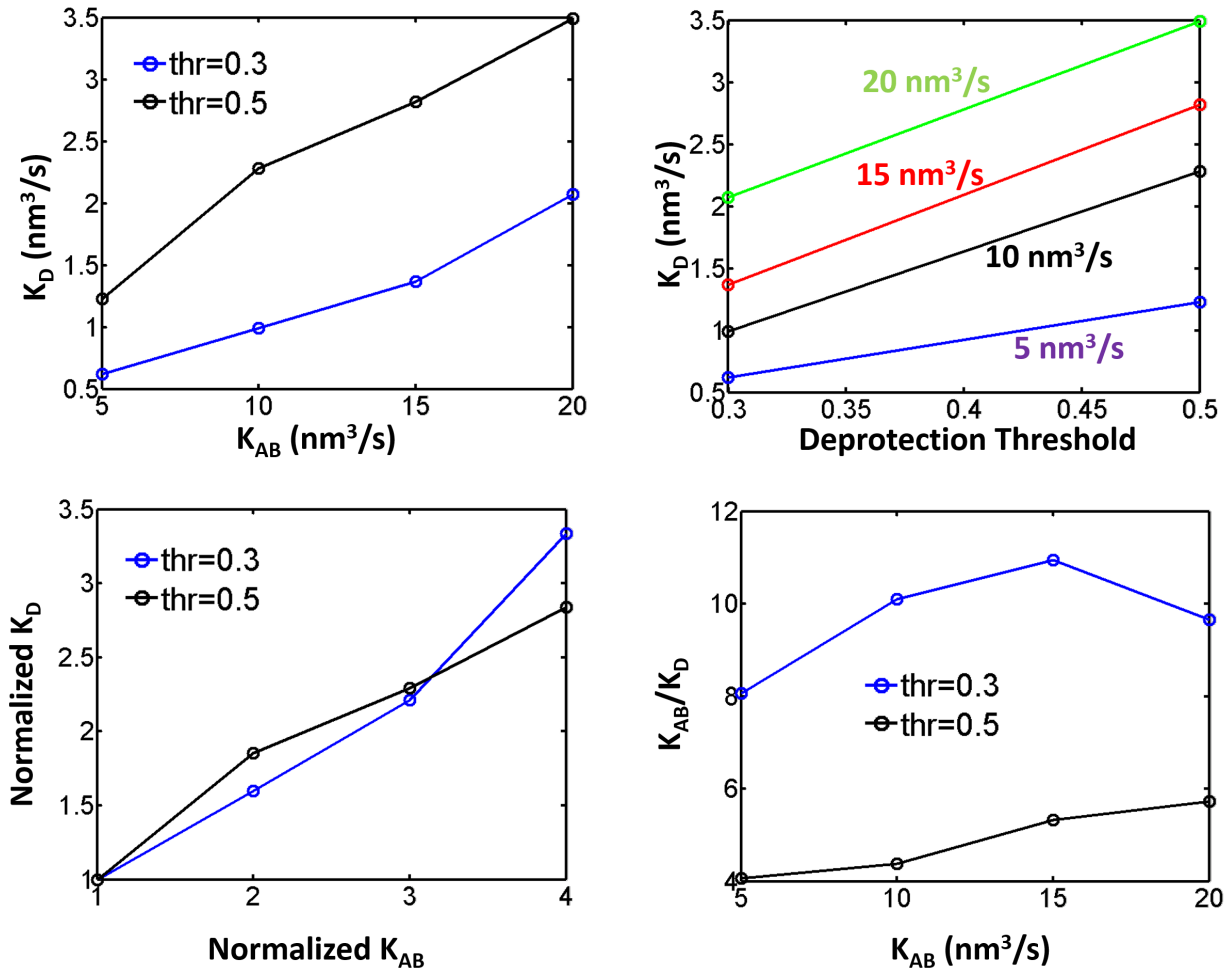
Figure 3.5: **(top left):** Best fit deprotection rate constant vs. neutralization rate constant; **(top right):** Best fit deprotection rate constant vs. deprotection threshold for various acid/base neutralization rate constants; **(bottom left):** Normalized increase in deprotection rate constant vs. normalized neutralization rate constant; **(bottom right):** Ratio of neutralization rate constant and the deprotection rate constant v.s. neutralization rate constant

3.4.2 Calibration of Acid Diffusion Length

For each reaction kinetics parameters shown in Fig. 3.5, the acid diffusion length over a 90 s bake time with a bake temperature of $100^{o}C$ was chosen so as to closely match the CD at the experimentally determined value of dose (E_{size}) needed to pattern 50 nm half-pitch lines and spaces. An alternative to this approach is to perform a least squares fit of the acid diffusion length by using all the data points as a function of dose. This approach was

not taken here, however for most of the scenarios a close match was found between the simulated and experimental linewidths for all of the dose values by simply fitting the acid diffusion length at E_{size}. In Fig. 3.6, the simulated CD vs. dose and the experimental CD vs. dose are compared for both the dissolution threshold values of 0.3 and 0.5, and the acid/base neutralization rate constant values of 5 nm^3/s and 10 nm^3/s. Comparisons for the neutralization rate constant values of 15 nm^3/s and 20 nm^3/s are shown in Fig. 3.7. In both of these figures, the plotted CD values in the case of experimental data correspond to the width of the remaining resist. Since the resist being simulated is a positive tone resist, in simulation therefore the calculated CD is that of the unexposed regions of the line/space pattern. The acid diffusion lengths that were used for these simulations are annotated in the plots. Interestingly, most of the diffusion length values are very similar, on the order of about 16 nm.
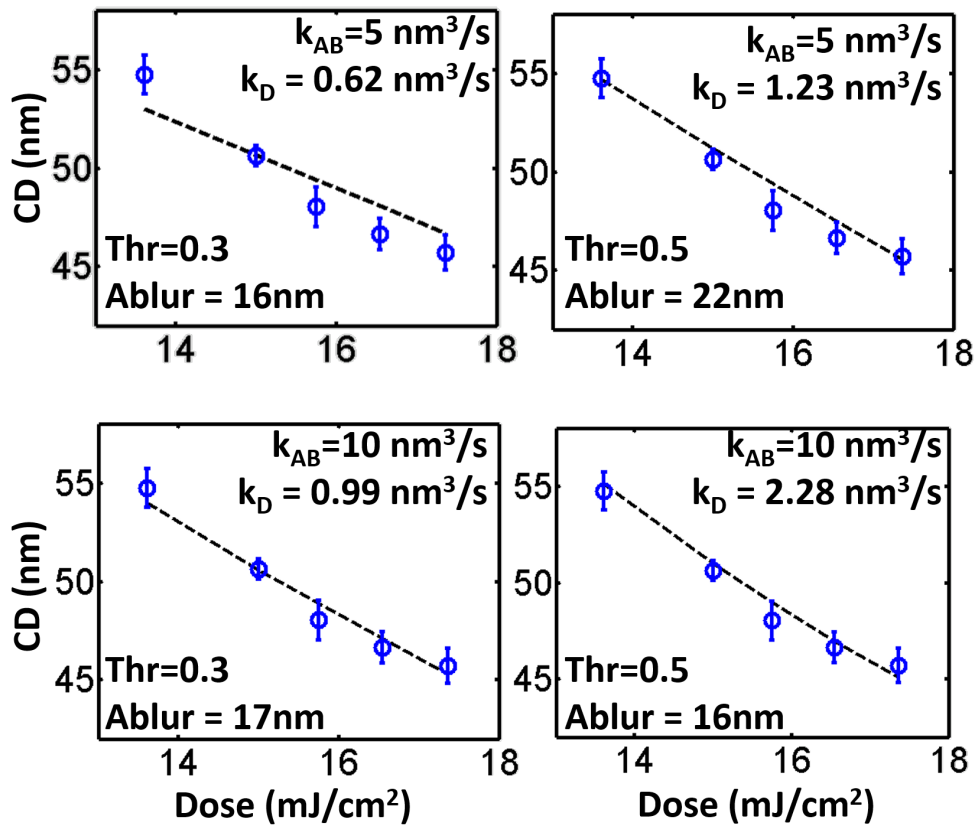
Figure 3.6: Comparison between simulated (dashed line) and experimental (blue circles) linewidth (CD) vs. dose for neutralization rate constants of 5 nm^3/s and 10 nm^3/s, and deprotection threshold values of 0.3 and 0.5. The corresponding deprotection rate constants can be found in Fig. 3.5
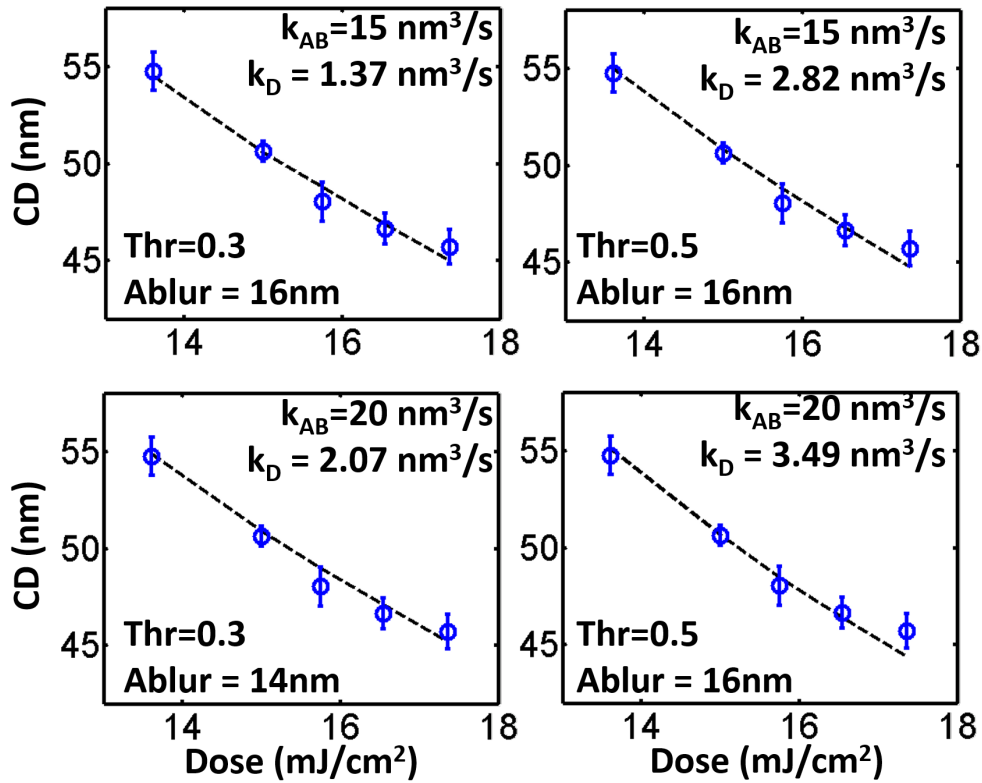
Figure 3.7: Comparison between simulated (dashed line) and experimental (blue circles) linewidth (CD) vs. dose for neutralization rate constants of 15 nm^3/s and 20 nm^3/s, and deprotection threshold values of 0.3 and 0.5. The corresponding deprotection rate constants can be found in Fig. 3.5

3.5   LER Contribution by Various Material Intrinsic Sources

For analyzing the influence of various contributors in determining LER, one of the parameter scenarios presented previously was used. Acid/base neutralization rate constant of 10 nm^3/s, a de-protection rate constant of 0.99 nm^3/s and a de-protection threshold of 0.3 were used. A summary of the LER values obtained by turning on one noise source at a time is provided in table 3.3. In the table, turning on photon shot noise means that only the randomness introduced by absorption was enabled, while the acid generation, and the volumetric densities were treated as deterministic values from table 3.2. Similarly, all three of the remaining sources of randomness in the table were enabled one at a time. The LER values were evaluated from the deprotection image at the point where the image reaches a dissolution

Table 3.3: Influence of various material contributors to the final deprotection LER

LER Source	LER	LER % in quadrature
Photon shot noise	1.94 ± 0.13 nm	46.7 %
Acid generation statistics	1.36 ± 0.12 nm	22.9 %
Base loading	1.63 ± 0.08 nm	32.9 %
Photo-acid generator loading	0.03 nm	0.01 %
Combined	2.84 ± 0.19 nm	100 %

threshold of 0.3. The total LER that results from enabling all the sources of randomness is 2.84 nm. This number is smaller than the value of 4 ± 0.3 nm measured for this resist. The model is expected to under-predict the LER since it captures only ideal LER and currently does not account for LER that could be contributed by the chemical interactions that take place during resist dissolution.

The LER values that result from enabling one source of randomness at a time add in quadrature to give 2.88 nm, within 1.4% of the value of 2.84 nm. The results show that 46.7% of the entire LER is contributed by photon shot noise. Base loading contributes 32.9% of the total LER, while the acid quantum efficiency contributes 22.9% of the total LER.

3.6 Summary

In this chapter, a stochastic resist model was used to study the influence of various material intrinsic source of randomness in determining the line edge roughness (LER) of the deprotection image in a chemically amplified EUV resist. Overview of the SuMMIT stochastic resist model was provided. Calibration of the model was performed using a combination of resist contrast curve and line/space patterning data. Emphasis was placed on fitting the reaction rate constants and the acid diffusion length values while holding the other resist parameters at typical baseline values. With the acid/base neutralization rate constants swept over a range of values from 5 nm^3/s to 20 nm^3/s and two different deprotection thresholds for dissolution, the best fit deprotection rate constants assuming a quantum yield of 2 were found to range between 0.6 nm^3/s and 3.5 nm^3/s. By using the extracted deprotection rate constants, the acid diffusion length was fit to the linewidth data at best dose to obtain a diffusion length of 16 nm for a 90s bake at a temperature of 100°C. Using the best fit rate constants and acid diffusion length the calculated LER values were found to under-predict the experimentally determined LER values. This indicates the presence of other contributors to the final resist LER. Considering that at best focus the mask contribution is likely small, some of the discrepancy between modeled and experimental LER is likely coming from the statistics of chemical interactions during the dissolution process. For the calculations presented here, photon shot noise was found to contribute 46.7% of the total deprotection

image LER, while base loading and acid generation statistics accounted for 32.9% and 22.9% respectively, of the total LER.

Chapter 4

Experimental Study of Exposure of Resists with Low Energy Electrons

In this chapter, an experimental approach is presented for studying the role of low energy electrons in causing chemistry in EUV resist films. A photon absorption event in an EUV resist produces photo-electrons and subsequently secondary electrons with energies that may range between 0 eV and 80 eV. By directly exposing the resist with electrons with these energies, interesting questions like the energy delivery capacity of the electrons can be experimentally studied. Of particular importance to EUV lithography are the questions of the spatial extent over which secondary electrons can create acids, and the extent over which the acids can lead to solubility switch in the resist. In this project, a chemically amplified EUV resist was directly exposed with electrons with energies between 15 eV and 91 eV, and the thickness loss measured after bake and dissolution. Thus, the actual measurements include the combined effects of events caused by electrons during exposure and the de-protection reactions caused by acids during the bake step. The resist thickness loss that can be measured after the exposure, bake and dissolution steps is known as the contrast curve. The contrast curves that were measured were used to estimate the relative energy delivery efficiency of electrons, and the results were tested against the proportionate energy delivery model which suggests that energy delivery capacity scales proportionately with electron energy. The low energy electrons considered here likely create acids in the top few nanometers in the material. For example, Gronheid et. al. [34] predicted a mean secondary electron blur of 2.4 nm by using a stochastic resist model calibrated to data for a chemically amplified EUV resist. By assuming a penetration depth for the electron, the contrast curve data measured here was used to extract a rough estimate the deprotection blur created by diffusion of acids through a simple fitting procedure. By using measured electron flux, estimates were also made of the amount of volume in cubic nanometers cleared per unit energy by an electron with energy ranging between 29 eV and 91 eV.

In the next section, an overview of the experimental techniques demonstrated in the literature for studying electron-matter interactions will be provided. The overall experiment used in this study will then be described. Subsequently, challenges associated with the

expeirmental technique will be described, which will include a discussion of the impact of acid diffusion and the impact of charging of films upon exposure to electrons. Then, the experimental results obtained by performing open frame exposures of a chemically amplified resist with a low energy electron microscope (LEEM) and subsequently with a scanning electron microscope (SEM) will be provided. Then, techniques for extracting the energy delivery efficiency of electrons based on contrast curve measurements will be presented. An estimate of the deprotection blur extracted from the resist contrast curves based on a fitting procedure will then be provided, followed by a calculation of the amount of volume cleared by dissolution induced by electron exposures at various energies. Finally, conclusions of the study will be presented.

4.1 Existing Experimental Techniques for Studying Low Energy Electron Interactions

The mechanisms with which low energy electrons interact with materials are of immense interest to many researchers, and several experimental techniques have been demonstrated in literature. For example, Hargreaves et. al. performed angle resolved gas phase electron energy loss spectroscopy (EELS) with incident electron energies ranging between 9 and 20 eV, and quantified the energy loss cross-sections in gas-phase ethanol for scattering angles ranging between 5° and 130° [37]. Khakoo et. al. focused on quantifying the cross-sections for excitation of vibrational modes in gas-phase tetrahydrofuran (C4H8O) with incident electron energies ranging between 2 eV and 20 eV [38]. In EUV lithography, the mechanisms of low energy electron interactions are important because the most probable outcome of an EUV photon absorption event is the ionization of resist which results in generation of a photo-electron and subsequently, secondary electrons. These electrons are primarily responsible for causing events that can eventually lead to a solubility switch during the bake step that occurs after the initial exposure step. In a chemically amplified resist, the role of the electrons is to react with the photo-acid generators (PAGs) to create acids. The processes by which these interactions occur are complex, and designing experimental techniques to understand the processes involved is of tremendous value. Narasimhan et. al. tested whether the mechanism of internal excitation is a viable pathway for excitation of a PAG by 80 eV electrons [39]. The authors drew an analogy between internal excitation and the easier to measure phenomenon of electron-induced flourscence and presented data for quantum yield for a variety of fluorophores. Decomposition of PAGs due to interactions with electrons can produce by-products along with acids. One such by-product is benzene. Grzeskowiak et. al. [40] exploited the out-gassing of benzene from resists, and with the aid of mass spectrometry estimated the number of reactions triggered by an 80 eV electron. Narasimhan et. al. [41] performed flood exposures of resists with electrons having energies larger than and equal to 80 eV, and provided a comparison between thickness loss experimental data and Monte Carlo modeling of electron-resist interactions. Thete et. al. [42] used a low

energy electron microscope to assess thickness loss in poly-methyl methacrylate (PMMA) resist upon exposure to low energy electrons.

The key question pertaining to low energy electron interactions in the resist has to do with the energy efficiency of the electrons at various energies at triggering useful chemistry. Gas phase experiments can be designed to test the energy loss by electrons to resist molecules. For example, Ogletree et. al. presented measurements of the cross-sections of electron-impact ionization of an iodo-methylphenol resist compound [43] for energies ranging from single-digit eV up to 100 eV incident energies. Experimental techniques for solid phase measurement of these interactions are also important and can complement the results from gas phase measurements. In this project, the same experimental approach by Narasimhan et. al. [41] and Thete et. al. [42], of directly exposing EUV resist films with low energy electrons over large areas (micron scale) was used. In such an experiment, the loss in resist thickness as a function of dose can be measured after exposure and application of bake and dissolution processes. The curve that results is known as the contrast curve. In typical contrast curve experiments, the volumetric energy density deposited by a high-energy (kilo-electronvolts) electron beam scales proportionately with the energy of the electron. This idea was tested for low energy electron exposures by simply scaling the dose values in the measured contrast curves with the ratio of electron energies.

4.2 The Experimental Approach Used in this Work

An overview of the overall experimental approach is provided in Fig. 4.1. A leading chemically amplified EUV resist is spin-coated on a silicon wafer with HMDS as an adhesion layer. Open frame exposures of the resist are performed with electrons with energies that would be typical of the electrons created by photon absorption in an EUV resist. Exposures are performed at a range of dose values. Considering that the values of penetration depth of electrons at the energies of interest are on the order of a few nanometers, the exposure leads to the creation of acids concentrated near the top few nanometers of the resist [34]. Following the exposure, the resist is baked to drive the reaction/diffusion mechanisms that involve diffusion of the acids deeper into the resist, deprotection reaction and acid/base neutralization reactions. After the bake step the resist is developed with tetra-methyl ammonium hydroxide (TMAH), which results in conversion of the deprotection profile in the resist into a dose dependent thickness loss. The thickness loss vs. dose trends can then be analyzed as a function of electron energy to assess the energy delivery capacity of electrons at various energies.

The first round of experiments were performed with a low energy electron micrsocopy (LEEM) tool at the National Center for Electron Microscopy (NCEM) at the Lawrence Berkeley National Laboratory [44]. A second round of experiments was also performed, where the resist was exposed with electrons created in a scanning electron microscope operated in deceleration mode. The first round of experiments provided clues about the important phenomenon of charging that occurs during thin film exposures with charged particle beams.

It is impossible to conclusively establish that the thickness loss data is not corrupted by charging artifacts without directly measuring the surface potential as a function of exposure time. However, the SEM allows for direct visualization of the secondary electron signal being emitted from the sample, which can then be used to tune the SEM control parameters to minimize artifacts typical of charging, e.g. image distortions, at least in a qualitative sense.
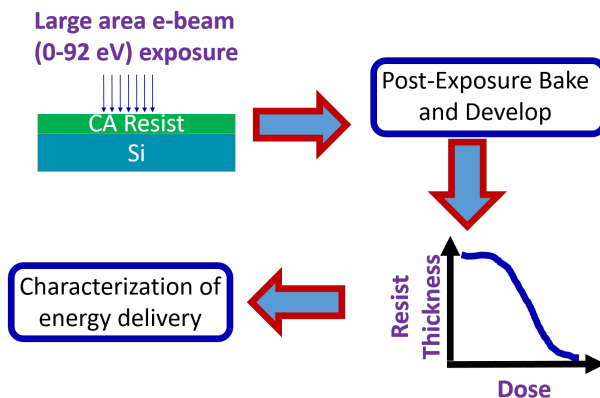
Figure 4.1: The experimental technique for exposing an EUV resist with low energy electrons to assess the energy delivery capacity of electrons

4.3 Challenges

4.3.1 Acid Diffusion Effects

While this experimental technique can provide useful insights about the capability of electrons at triggering chemistry useful for EUV lithography, it cannot provide direct measurements of the electron penetration depth. As described in the previous chapters, formation of the image in a chemically amplified resist involves the reaction and diffusion processes that occur during the bake step. As a result, in this experimental approach where electrons create acids in the top few nanometers of the resist, during the bake process the acids can penetrate much deeper in the resist and cause thickness losses that are much larger than the electron penetration depth. The implications are that the measured thickness loss vs. exposure dose data needs to be examined as a combined effect of electron penetration into the material as well as diffusion of acids during the bake step.

4.3.2 Charging Effects

Insulating materials that cannot provide a direct path to ground can accumulate extra charge when exposed to charged particle beams. This leads to the formation of potentials on

the sample that can contribute to retardations or accelerations of electrons that do enter
the sample, thus perturbing the energies of electrons that actually trigger chemistry. In
scenarios with very low incident energies, the charged surface can act like a mirror that
reflects electrons. The magnitude and time-domain behavior of these potentials during the
exposure process depends on the overall charge balance, i.e. the flux of electrons leaving the
sample through emission and back-scattering mechanisms relative to the flux of electrons
incident on the sample.

Shaffner et. al. [45] treated the insulating sample as a leaky capacitor, and suggested
a simple exponential drop model for charge decay between exposure frames. Babin et. al.
performed more rigorous calculations of transport of the excess electrons in a material by
using drift and diffusion models [46]. The authors also experimentally demonstrated impact
of charging on the secondary electron emission as a function of number of recorded frames
for landing energies ranging between 100 eV and 3 keV [47]. At 100 eV incident energies,
the electron yield with a larger number of integrated frames was found to be 41% lower than
the yield with a smaller number of integrated frames, and the reduction was attributed to
sample charging.

Bai et. al. [48] developed an apparatus involving a Kelvin probe mounted inside an e-
beam vacuum chamber for direct measurements of surface potentials on an e-beam resist after
exposure with 10 and 20 keV electrons. The stage allowed the authors to move within seconds
the exposed regions of the resist to fall underneath the Kelvin probe for a measurement of the
surface potential. Surface potentials of 1.1 V and 2.6 V were observed for 10 keV and 20 keV
exposures at two different thickness and incident dose values. The interesting result was that
the potentials were found to drop by only about 35% after roughly one hour. The authors
suggested an expression for the voltage due to the charge at the top surface as well as the
charge trapped deeper in the insulator when exposed to high energy electrons. Considering
that exposures with energies lower than 100 eV result in excess charges being trapped mostly
near the top few nanometers, Denbeaux [49] considered only the surface charge and used
the expression for surface potential given by equation 4.1. Here, ϕ is the surface potential
magnitude, $sigma$ is the deposited area density of charge, d is the film thickness, ϵ_o is the
permittivity of free space, and ϵ_d is the relative permittivity.

$$\phi = \frac{\sigma d}{\epsilon_o \epsilon_d} \tag{4.1}$$

The implications of charging in this study was that it put a limit on the smallest electron
energy for which the thickness loss data could be trusted. As will be shown later, with
exposures down with the SEM this energy was 29 eV.

4.4 Resist Thickness Loss Experiments with a Low Energy Electron Microscope

The low energy electron microscope (LEEM) available at the national center for electron microscopye (NCEM) at the Lawrence Berkeley National Laboratory [44] is capable of creating electron landing energies down to 0 eV, and allows for experimental studies of surface phenomena. In this experiment, the tool was used for exposing the resist with a variety of energy values over a range of exposure dose values, by letting the beam dwell over a certain time period in selected regions, while turning off the beam when moving the stage.

Two experiments were performed, and the resist processing parameters are summarized in table 4.1. Interestingly, after the develop process, the unexposed regions of the resist were found to suffer 13 to 16 nm thickness loss, which suggests a background dissolution rate of the polymer. Since a measurement of the landing current was not available, all the exposures were done by holding the emission current constant, and setting the dose by controlling the exposure time. Scanning Electron Microscope (SEM) images of the printed patterns for the two different experiments are shown in Fig. 4.2. The spots in these images are separated by 100-150 μm.

For the first experiment, that corresponds to the image on the left in Fig. 4.2, dose values at each energy increase from bottom to top. Exposures were also perfored with a 80 eV energy. Those patterns are not captured in the SEM image, but the thickness data were measured and will be described later. The emission current value was held at 184 nA. For 15 eV patterns, the exposure times ranged from 50 s to 350 s. However, pattern for the first dose could not be found during the thickness measurement, therefore the thickness loss data to be presented later contains the thickness obtained with 100 s exposure as the first data point. For 20 eV patterns, the exposure times ranged between 10 s an 90 s. For 25 eV and larger energies, the exposure times ranged from 5 s to 80 s. The missing exposure spots in the array are intentional as surface contamination was encountered at these co-ordinates. At large doses with 40 and 60 eV incident energies, the spots appear to be darker in the SEM image. This is occuring likely due to cross-linking of the resist upon over-exposure. Cross-linked resists do not develop in a positive tone developer such as tetra-methyl ammonium hydroxide (TMAH). Therefore, the thickness loss data to be presented later will show a corresponding increase in thickness at these large doses.

For the second experiment (30-80 eV exposure image), the dose values increase in alternate directions in each row for a fixed incident energy in Fig. 4.2. Lowest dose for the 30 eV exposures corresponds to the first spot from the left. For 30 eV, the emission current value was 375 nA, with exposure times ranging from 10 s to 80 s. Compared to the first experiment, with 2X the current and similar exposure times if the landing current scales linearly with emission current, the relative dose increase for 30 eV in the second experiment would be 2X relative to the first experiment. For 40, 60 and 80 eV, the emission current was lowered relative to the first experiment in order to obtain data points that did not contain cross-linking effects. The current vlaues ranged between 106 nA and 109 nA. Exposure times

ranged between 5 s and 80 s. The patterns at 30 eV in these images appear to get darker with increasing dose, and this could also be a cross-linking effect.

Table 4.1: Experiment parameters for first round of exposures of resist with low energy electrons using the LEEM tool

Parameter	Expt No. 1	Expt No. 2
Post-apply bake Temp/Time	110°C / 90 s	
Pre-exposure film thickness	45 nm	66 nm
Post-develop unexposed resist thickness	32 nm	50 nm
Post-exposure bake Temp/Time	110°C / 90 s	
Developer solvent	MF26A	
Develop time	40 s	
DI water rinse time	30 s	
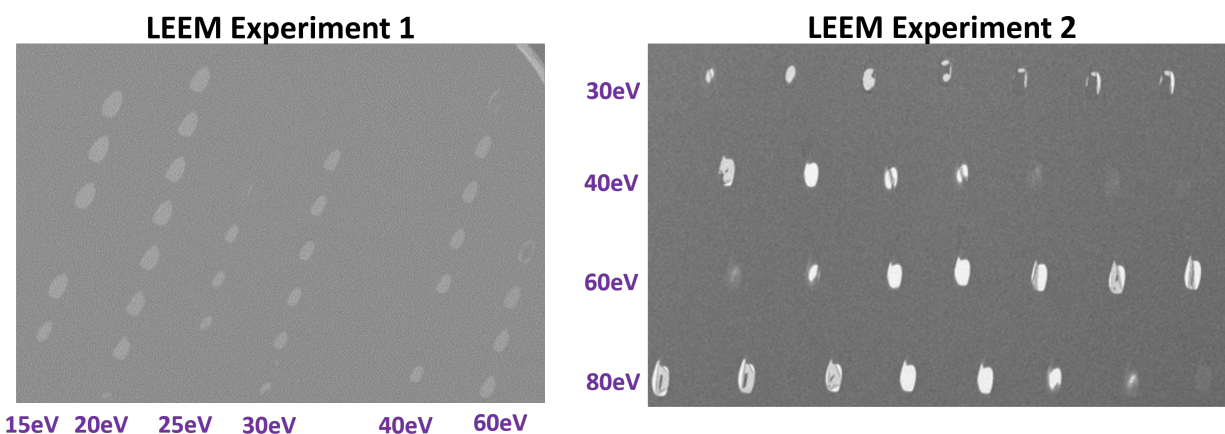
Figure 4.2: SEM images for patterns formed with low energy electron exposures performed with a low energy electron microsope (LEEM) tool; **(left):** Experiment 1, dose increases from bottom to top; **(right):** Experiment 2, dose increases in a serpentine pattern, starting from top left exposed pattern

4.4.1 First Round of Low Energy Exposures Experiment with the LEEM Tool

In the first LEEM experiment, exposures were performed with incident electron energies ranging between 3 eV and 80 eV. No resist patterns formed at energies below 15 eV incident energy (3, 6, and 9 eV were tried). Thete et. al. observed this same result for exposures

of PMMA resist with their LEEM tool [42]. Resist thickness data for the first experiment
are shown in Fig. 4.3. Since the size of the focused beam is roughly the same size as the
spot over which the thickness metrology tool calculates the thickness, only one measurement
could be performed for each dose and energy. Therefore, error bars for the thickness values
could not be calculated. Data for 15 to 30 eV energies are shown on the left, while the data
for 30 to 80 eV energies are shown on the right. The 30 eV data shown in the plot on the left
is also provided in this plot for reference. The typical dose notation in e-beam lithography is
in the units of area density of charge, $\mu C/cm^2$. However, since the landing beam current is
usually much smaller than the emission current, and was not measured, the incident charge
density could be not be calculated. Therefore, dose values shown on the horizontal axis in
the figure have been normalized relative to the smallest dose value across all energies. In
the plots, only thickness values larger than 18 nm are valid, as this is the measurement floor
below which the NanoSpec tool used for these measurements is not capable of accurately
measuring the thickness. Considering that electron range at these low energies is on the
order of only a few nanometers, thickness loss on the order of 12 nm is due to the diffusion
of acids in the resist. The data shows that 15 eV electrons require a drastically larger dose
to clear same amount of resist thickness than 20, 25 and 30 eV electrons do. There is also
slight indication that 30 eV electrons are creating more acids than 20 and 25 eV electrons.
Slope of the 25 eV electron thickness vs. dose curve is significantly different that the slopes
of the 20 eV and the 30 eV contrast curves. In the figure on the right, in the low dose regime
shift in the thickness trend is roughly inversely proportional to the beam energy. On the
high dose end where cross-linking effects are likely occuring, the dose needed to cross-link is
smaller for larger electron energies.
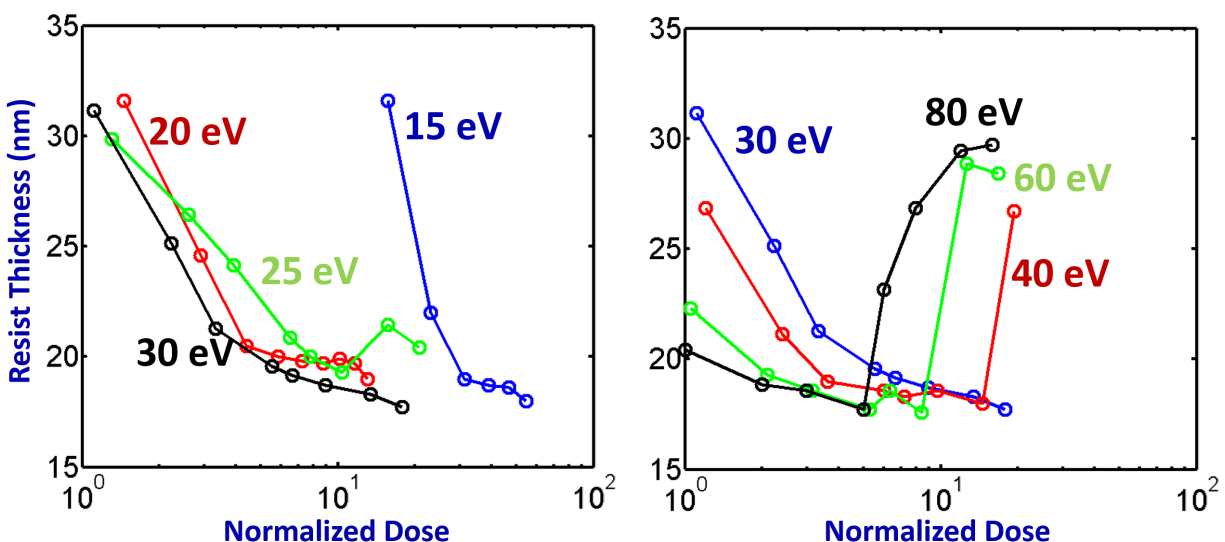
Figure 4.3: Data for experiment No. 1 done using the LEEM tool. Thickness minimum of 18 nm is the measurement floor of the NanoSpec tool that was available for these measurements; **(left):** Thickness vs. dose for 15 to 30 eV; **(right):** Thickness vs. dose for 30 to 80 eV, showing cross-linking at high doses for 40 to 80 eV energies

4.4.2   Second Round of Low Energy Exposures Experiment with the LEEM Tool

In the second LEEM exposures, a larger spun resist thickness was used with the motive of extracting thickness loss data over a wide range, as summarized in table 4.1. However, in this experiment no patterns formed at 15, 20 and 25 eV incident energies, while patterns did form at energies between 30 and 80 eV. A possible explanation for this observation is that the surface potentials in the thicker resist were large enough to apply sufficient deceleration on the electrons with energies lower than 25 eV. The contrast curve results for round 2 of experiments with the LEEM tool for 30 to 80 eV incident energies are shown in Fig. 4.4. The energy values annotated in the contrast curves are the energies used in the exposure and do not subtract any surface potentials that may have formed. As mentioned earlier, the emission current for 30 eV exposures in the second experiment was 2X larger compared to the first experiment. The exposure time values were such that the dose values for the seven data points for 30 eV data shown in Fig. 4.4 correspond to 2X the dose values of the last seven data points for 30 eV data shown in Fig. 4.3. Yet, the 30 eV exposure data for this experiment shows an increase in thickness at high doses while the results of the first experiment for corresponding 2X larger doses do not.
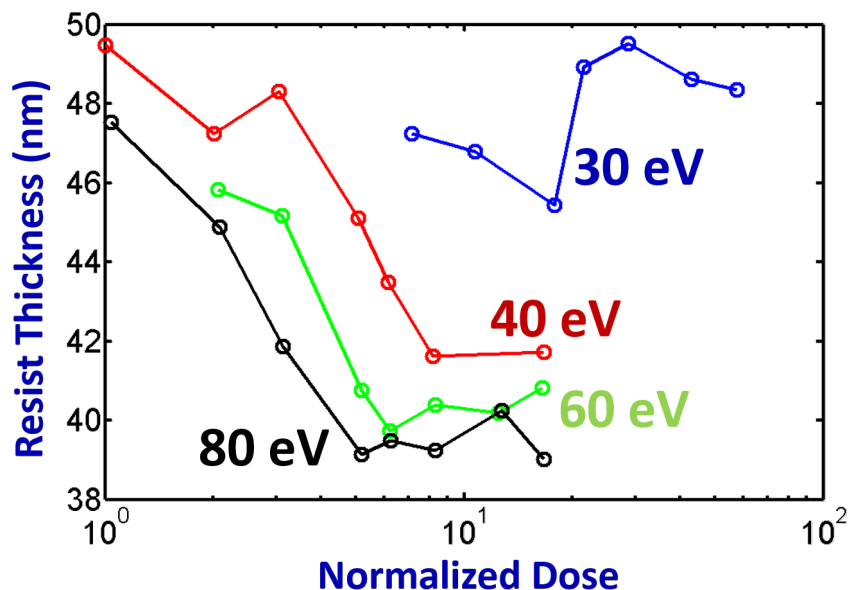
Figure 4.4: Data for experiment No. 2 done using the LEEM tool; **(left):** Thickness vs.
dose for 15 to 30 eV; **(right):** Thickness vs. dose for 30 to 80 eV, showing cross-linking at
high doses for 40 to 80 eV energies

In summary, the LEEM exposure experiments revealed thickness loss on the order of 8
to 10 nm for electron energies between 15 eV and 80 eV, which was interpreted to be due to
diffusion of acids in the material given that electrons penetrate only a few nanometers. The
experiments revealed the possbility of cross-linking mechanisms at very high doses even in
positive tone resists. The experiments also revealed the likely presence of charging.

4.5   Resist Thickness Loss Experiments with a Scanning Electron Microscope Operated in Deceleration Mode

The experiment performed using the LEEM tool was also replicated on a Hitachi-S4800
scanning electron microscope (SEM) operated in deceleration mode. The motivation for this
was that an SEM could be used to test the severity of charging at a given landing energy
by examining the secondary electron signal emitted by the sample for typical signatures of
charging, e.g. image distortions and uneven brightness. A summary of the overall exper-
imental technique is shown in Fig. 4.5. Low energy electrons are created by applying a
negative DC bias (Vdecel) on the sample stage in the SEM chamber. The landing energy
then becomes Eland = Eacc - q*Vdecel, where Eacc is the accelerated energy of the electron,

and q is the electronic charge. A large area exposure is performed by raster scanning the focused electron beam over a field of view that can be set by choosing an appropriate SEM working distance and magnification setting. The resist is then baked to trigger the reaction/diffusion processes, followed by developing the exposed resist in TMAH. The resulting contrast curve is then used to analyze the energy delivery capabilities of electrons at various energies. In Fig. 4.5, an example microscope image of the post-develop patterns formed on the resist from an early iteration of the experiments is also provided.
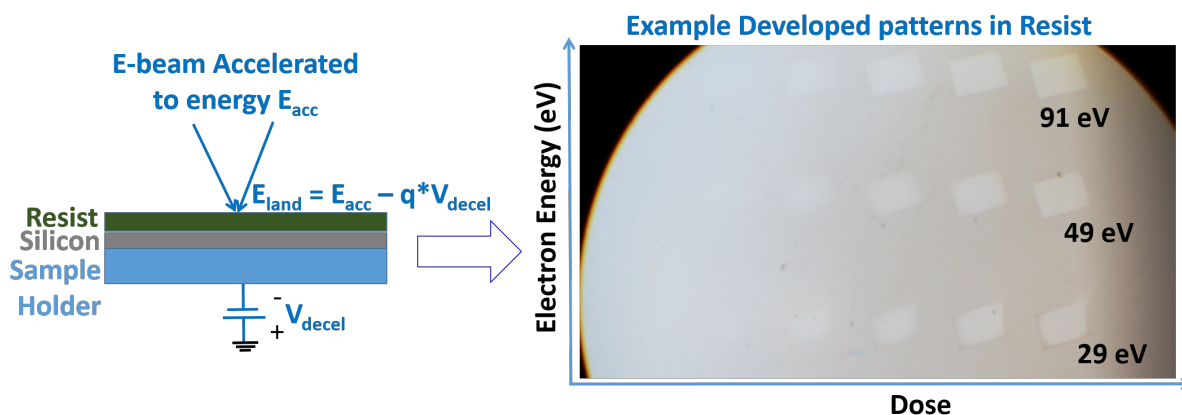
Figure 4.5: The experimental technique for performing low energy electron exposures, by operating an SEM in deceleration mode

Summary of experimental parameters is provided in table 4.2. Exposures were performed with electron energies ranging from 91 eV down to 29 eV. In this energy regime, with a low emission current of 2 μA, and a scan rate of 33 ms/frame, the secondary electron images of surface defects in sacrificial parts of the wafer were found to be well behaved without distortion and uneven brightness effects typical of charging. At energies lower than about 25 eV, the secondary electron images of surface defects were found to demonstrate significant distortions which was taken as a sign of charging, therefore these energies were not used for exposures. The post-exposure bake (PEB) temperature was reduced to 90°C from 110°C used in the LEEM experiments so as to reduce the net blur of the reaction/diffusion point spread function. Similarly, the dissolution time was reduced to 6 seconds from 30 seconds in order to prevent substantial thickness loss in the unexposed regions that was seen in the LEEM experiments (table 4.1).

Table 4.2: Summary of experiment parameters for exposure of resists with 29-91 eV electrons

Parameter	Value
Resist type	Positive tone, chemically amplified
Spun thickness	32.01 ± 0.11 nm
Post-exposure bake	90^oC for 90 s
Develop chemistry	6 s in TMAH, 6 s DI water rinse
SEM model	Hitachi S-4800
SEM emission current	2.0 μA
SEM acceleration energy	500 eV
Variable DC bias	408-470 eV
Patterned field sizes	42.3 X 29.4 μm^2
Center-to-Center separation between fields	200-300 μm

4.5.1 Estimate of the Landing Current Dynamics in the SEM Chamber

The SEM control system allows us to set the emission current, however the landing current after the electrons go through the focusing optics is usually substantially smaller. In order to obtain an estimate the relative magnitudes of current landing on the sample, a pico-ammeter was used for measuring the current with 500 eV electrons incident on the metallic sample holder. A deceleration voltage could not be used for this measurement because both the voltage source and the ammeter share the same co-axial connector on the tool. In addition to the emission current setting, other parameters like the condenser lens excitation and the probe current mode can be used for finer control of the landing current. The plot on the left in Fig. 4.6 shows the current measured with a Keithley 6517A pico-ammeter, with an emission current of 2 μA, with the condenser lens and the probe current settings set to operate in lowest possible current modes. An interesting trend is observed, where the current rapidly rises after the beam is turned on, then drops and then rises gradually again. The plot on the right shows the current behavior in the first eight seconds. The first peak around four seconds corresponds to a systematic effect, which is clearly visible on the secondary electron signal on the control computer screen every time the beam is turned on regardless of the sample being studied. The relative locations of this peak for the three measurements are different due to the measurement being started at slightly diffent times. The second peak around six seconds and the time-domain behavior is likely a function of the material being studied. Interestingly, transient behavior of the current shows about 27% fluctuation between the minimum value reached in the first minute and the close to stable value of 0.7 pA reached in about 20 minutes.
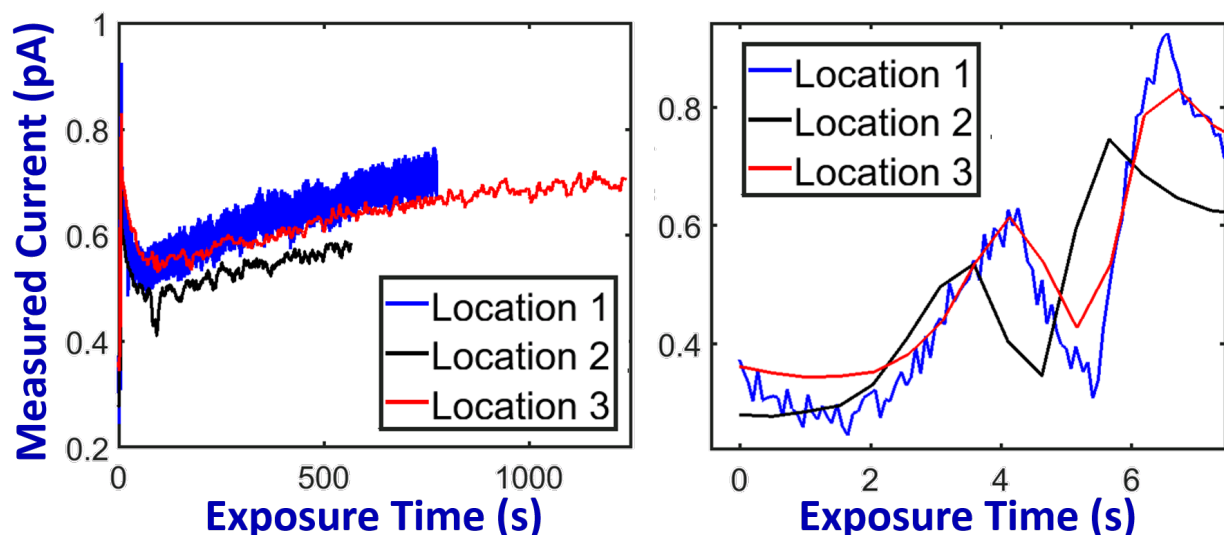
Figure 4.6: Landing current measured at three different locations with an emission current of $2\mu A$, with the condenser lens and the probe current parameters set to operate in lowest possible current modes; **(left):** The current values over a maximum of 20 minutes; **(right):** The current values in the first 8 seconds

4.5.2   The Contrast Curves Data

Considering that turning the beam on results in the first peak current of roughly 0.6 pA seen in Fig. 4.6, for all the exposures, first the beam was turned on in a sacrifical region of the wafer, and was left to dwell for a few minutes. Subsequently, the beam was simply blanked to ensure that it was not exposing the sample, without turning it off. Then, the stage was moved to the desired co-ordinates for performing the exposures. While direct measurement of current with the application of the deceleration could not be made as mentioned above, the time domain behavior of the incident charge calculated with the current profiles shown in Fig. 4.6 was used in conjunction with the exposure time to calculate the relative dose values between exposures. A plot of the charge vs. time evaluated by integrating the current vs. time data is provided in Fig. 4.7. The charge values that correspond to the typical exposure values used in the experiment are plotted as blue circles. The time dependence of charge is not exactly linear since the current vs. time plot is not constant.
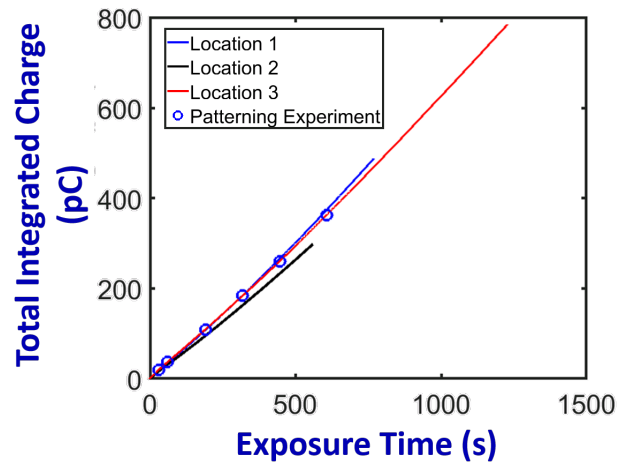
Figure 4.7: Accumulated charge vs. time in the SEM. Charge values corresponding the exposure times are shown as blue open circles

The SEM can be operated at various raster scan frame rates. Three frame rate settings of 33 ms/frame, 8 s/frame and 30 s/frame were used for performing the exposures. Two exposures were performed for each energy and dose setting. Of all the exposure conditions, the 91 eV exposure with a frame rate of 33 ms/frame had the largest thickness standard deviation of up to 3 nm. The data are provided in Fig. 4.8. For each frame rate, the dose values were normalized by the smallest dose aross all energies for each dataset. At about one order of magnitude larger dose, the resist thickness drops by about 5 to 6 nm compared to the unexposed thickness.
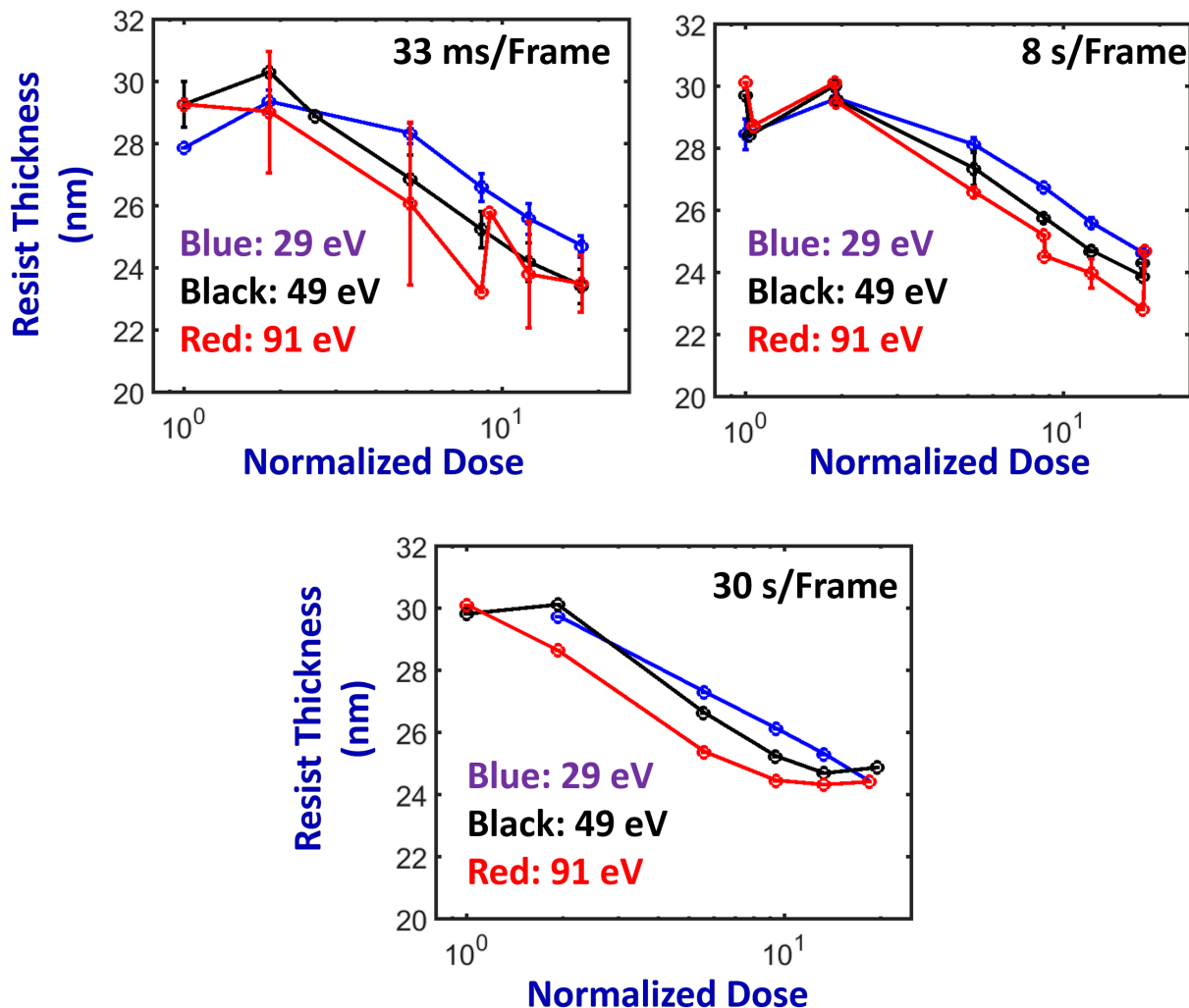
Figure 4.8: Measured contrast curves with resist exposed with an SEM operated in deceleration mode at three scan frame rates from two experiments

4.6   Energy Delivery Efficiency as a Function of Electron Energy

In order to test whether the energy delivery efficiency scales proportionately with electron energy, the dose values in the contrast curves were scaled by a fraction such that a close overlap of the thickness vs. dose trend was obtained. Resulting contrast curves for the first LEEM experiment are shown in Fig. 4.9. Results are shown for the 15 to 30 eV exposures, as well as the 30 to 80 eV exposures where cross-linking behavior was observed. For the 15

to 30 eV exposure data, 30 eV was used as the reference while all the dose values for the
remaining three contrast curves were scaled so as to obtain a close overlap of the thickness vs.
dose trends in relation to this reference. For 15 eV and 25 eV data where clear discrepancies
in the slopes are seen, the scaling fractions were closen to closely match the thickness values
around 23 nm. These curves allow for determining the relativey energy delivery capacity of
the electrons at various energies. For example, if the energy delivery capacity of a 15 eV
electron was half as large as that of a 30 eV electron, the dose values would have to be scaled
by 0.5X in order to closely overlap with the 30 eV contrast curve. As shown in the plot,
the 15 eV data had to be scaled by 0.12X, which suggests that based on this data 15 eV
electrons are 12% as efficient as 30 eV electrons at triggering chemistry in the material. In
the plot on the right, the data for 80 eV was used as the reference, and the contrast curve
dose values were scaled to closely overlap the region where the onset of cross-linking behavior
is observed. The result shows for example, that 40 eV electrons which are half as energetic
as 80 eV electrons, are 35% as efficient from an energy delivery standoint.
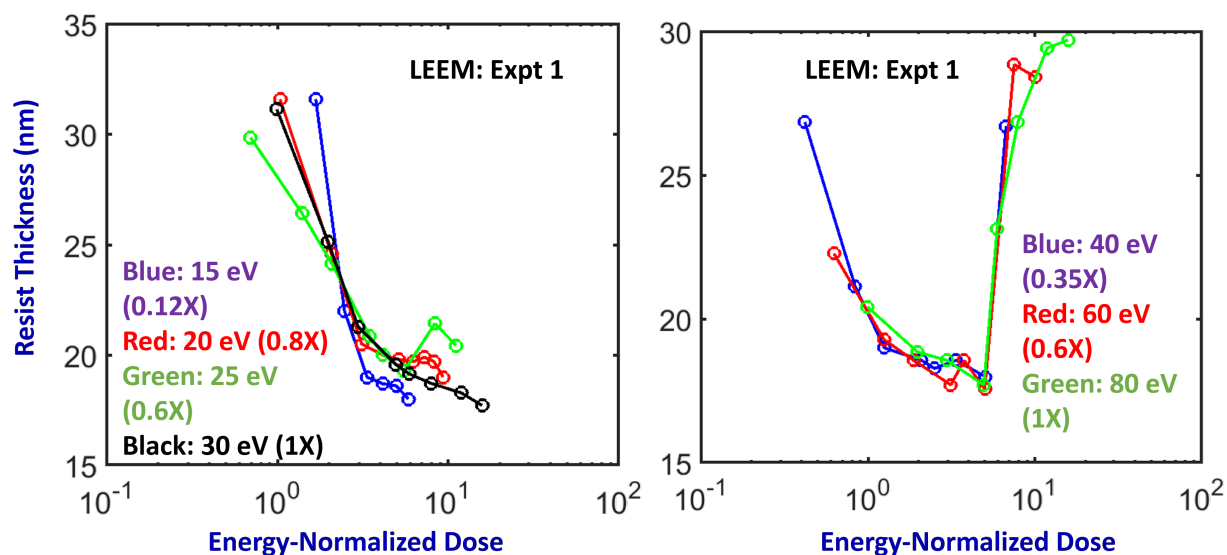
Figure 4.9: Contrast curve data from the first LEEM experiment with dose scaled by ratio
of energies

The contrast curves resulting from scaling the dose on data from the second LEEM
experiment are shown in Fig. 4.10. The results for the data obtained from SEM exposures
are also shown in the figure. For the SEM exposures, due to a lower post exposure bake
temperature, the acids may not penetrate as deep. As seen in the plots, the SEM exposure
data shows that in the linear region of the contrast curve, a 5X increase in dose results in
about 5 nm thickness loss. With the LEEM exposure data, a 5X increase in dose results in
about 8 nm thickness loss.
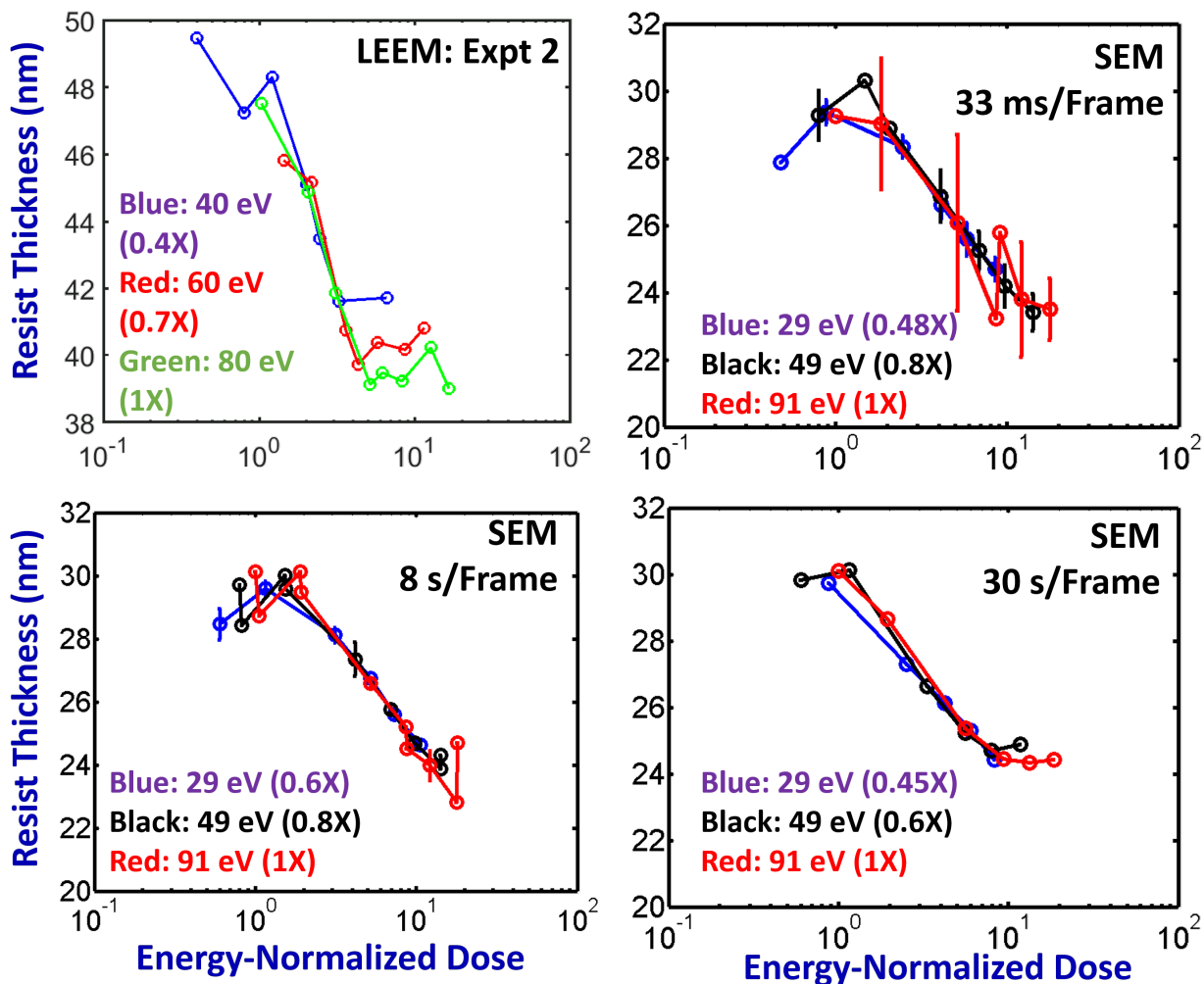
Figure 4.10: Contrast curve data from the second LEEM experiment, and the exposures performed with the SEM with dose scaled by a ratio to obtain close overlap for several incident energies

A summary of the dose scaling ratios that result in a close overlap between the contrast curves is provided in Fig. 4.11. The expected trend based on simple proportionate energy scaling model is also shown as the dashed blue line. For data in the 15 to 30 eV regime, the 20 eV data shows an energy delivery capability that is larger than that expected from the proportionate scaling model, however the opposite trend is found for 15 eV and 25 eV data points. Data for LEEM exposures in the 40 to 80 eV regime and the SEM exposure experiments are normalized relative to 80 eV so that the results can be compared. The LEEM experiments show energy delivery efficiencies that fall below that expected from proportionate scaling model. For example, 40 eV electrons are found to be around 0.4X

as efficient as 80 eV electrons, despite being half as energetic. This is in contrast with the energy delivery efficiency obtained with exposures performed with the SEM. For example, 29 eV electrons were found to be around 0.55X as efficient as 80 eV electrons despite being only 36% as energetic. These discrepancies could result from a combination of differences in the resist thickness, post-exposure bake and develop times used in the two experiments, as well as from discrepancies in the surface potentials due to charging that may have formed in the two exposure systems.

The presence of charging was described when presenting the contrast curve data from the LEEM exposures. As described before, in the SEM exposures, surface defects in sacrificial regions of the wafer were inspected to qualitatively test the impact of charging with a given energy, a procedure that was not performed with the LEEM experiments. Therefore, the data obtained for 29 eV, 49 eV and 91 eV energies with the SEM may be more accurate.
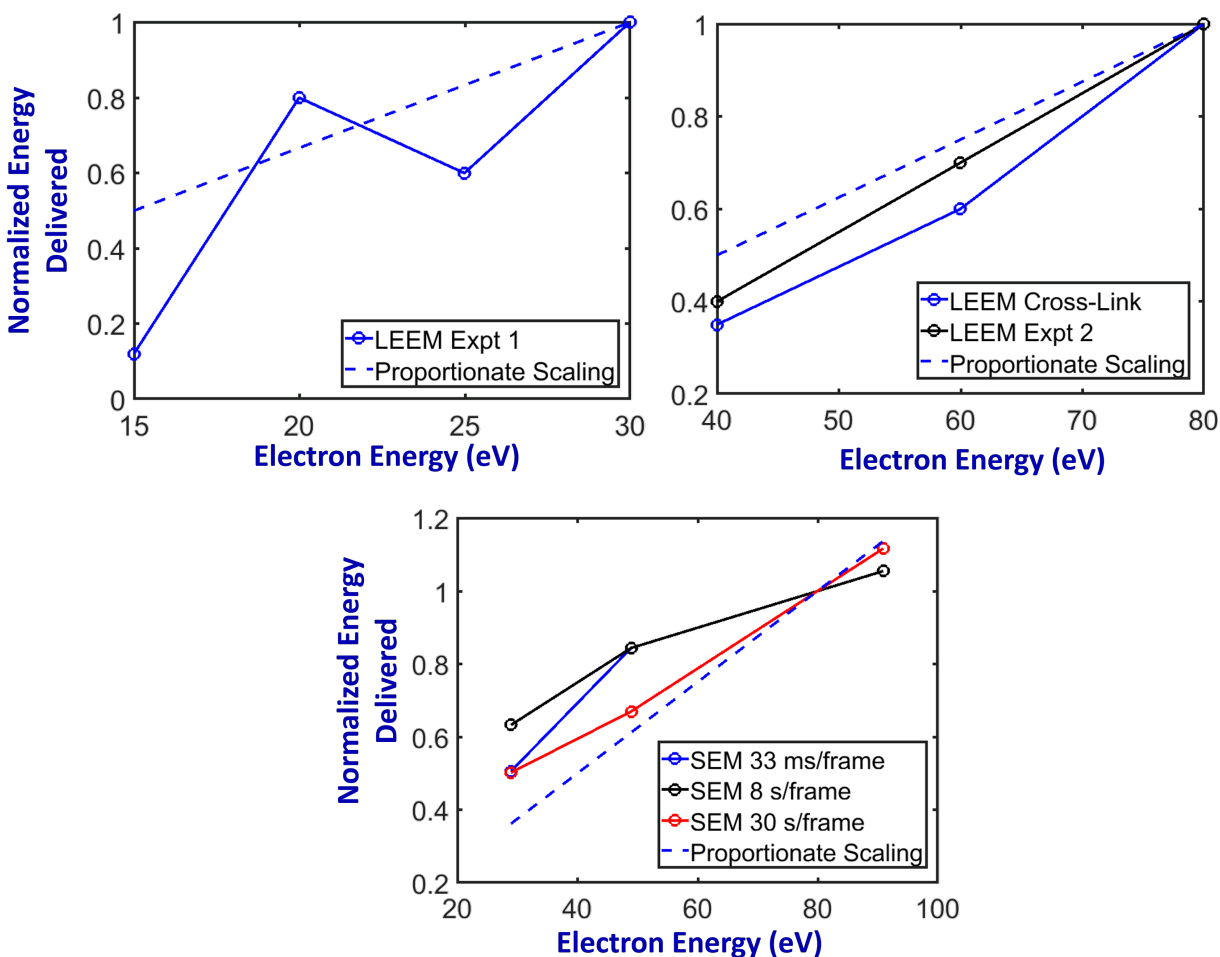
Figure 4.11: Summary of energy delivery capacity extracted from contrast curve data

4.7 Estimate of the Resist Deprotection Blur through Simple Modeling

The electron exposures result in creation of acids within the top few nanometers in the resist. Data however shows 8 to 10 nm of thickness loss. This occurs because of the diffusion of acids through the thickness of the film during the bake process. An estimate for the blur can be performed by using a simple fitting procedure like the one illustrated in Fig. 4.12. Here, the acidic region near the top of the resist is modeled with a uniform density with a spatial extent along the depth dimension equal to an assumed electron range. A Gaussian approximation is then made for the deprotection point spread function (PSF), and Fickian diffusion is assumed. Then, depth profile of the acid distribution is calculated by convolving the acid distribution with the deprotection PSF. By assuming a threshold for dissolution, the thickness loss can be calculated as a function of dose. Slope of the thickness loss vs. dose can be compared with measurement results to determine the full width at half maximum of the deprotection profile that results in a close match with experimental data. It should be noted that a better approach is to model the reaction/diffusion steps iteratively, as was shown in chapter 3 and will be shown in chapter 5. The results provided here are approximate calculations that do not take into account acid/base reactions.
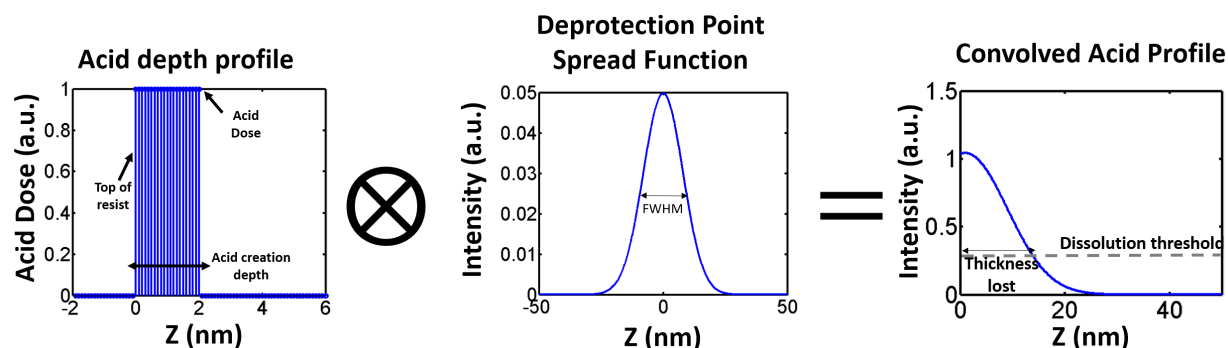
Figure 4.12: Procedure for extraction of resist deprotection blur through simple modeling; **(left):** Acid distribution created by electrons; **(middle):** Deprotection point-spread function with the full width at half maximum as a fit parameter; **(right):** Example convolved acid profile that can be used to esimate thickness loss

An example simulation result showing resist thickness as a function of dose for four different deprotection profile standard deviation values is provided in Fig. 4.13. The experimental data from SEM and LEEM exposures are provided in the middle and to the right in the figure. Dose values on the horizontal axes in these plots were scaled by the scaling ratios

shown in Fig. 4.10, and the points in the linear regime of the contrast curves were used for performing the fit shown in these plots with solid lines.
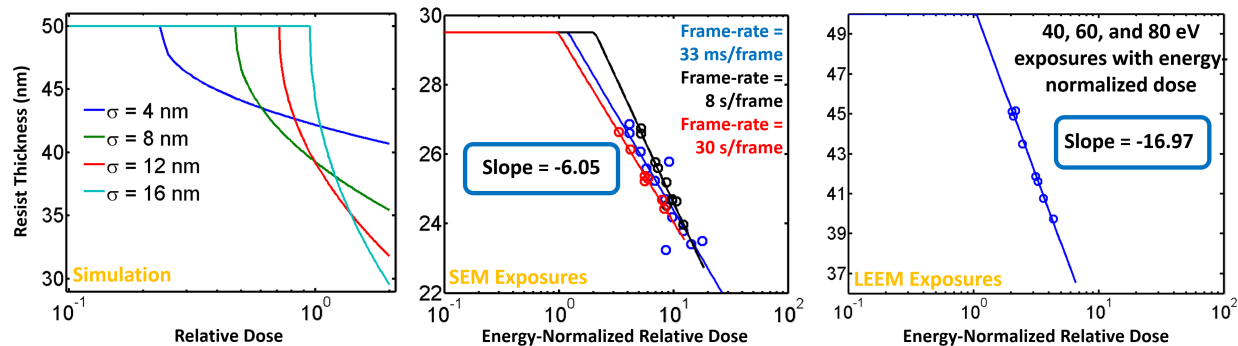
Figure 4.13: Resist thickness vs. dose for: **(left):** Simple simulation approach in Fig. 4.12, and experimental contrast curve data showing best fit line for **(middle):** SEM exposure data; **(right):** LEEM exposure data

In Fig. 4.14, calculations of slopes of the simulated thickness vs. dose results are shown as a function of standard deviation (σ) of the deprotection point spread function. The slopes were calculated at dose values where the simulated thickness loss values matched the experimental thickness loss values. Results are provided for two different electron range values and two different values for dissolution threshold. It should be noted that the electron range parameter simply specifies the depth over which acids are created in simulation. The boxes indicate the regions of the curve that closely match with experimental results for the SEM exposure data (90^oC bake), and the LEEM exposure data (110^oC bake). This simple approach suggests a deprotection spatial blur of around 4.5 to 5.5 nm for 110^oC bake, and around 2 to 3.5 nm for 90^oC bake.
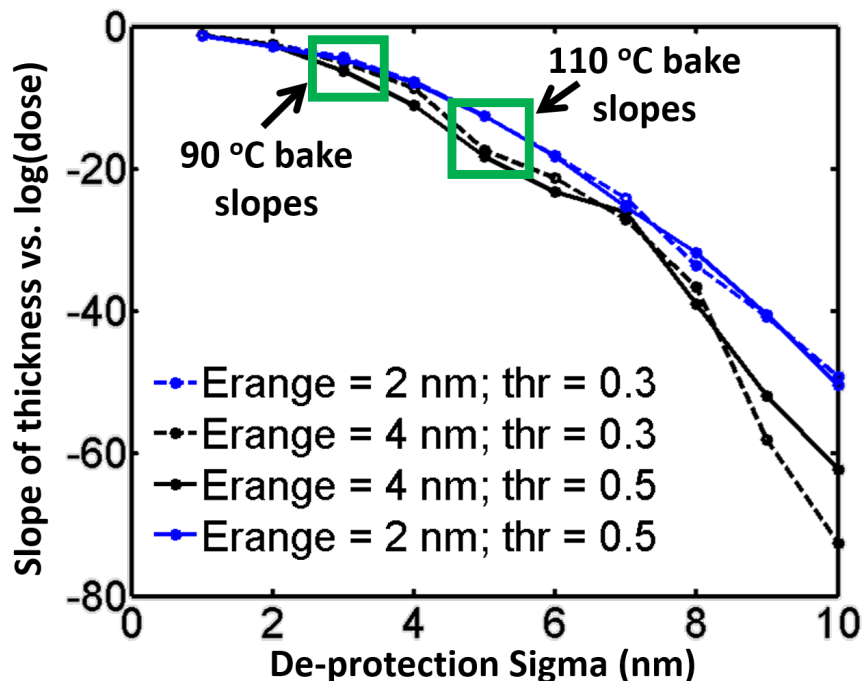
Figure 4.14: Slope of simulated resist contrast curves for a range of de-protection standard deviation (sigma)

4.8 Estimate for Volume Removed by Dissolution Induced by Low Energy Electron Exposures

One of the most important paramaters for EUV lithography is the amount of chemistry that electrons created by EUV photons can trigger, and the spatial extent over which they can do this work. The dissolution contrast curve data measured with low energy electron exposures can be used to gain insights into the specific question of the amount of volume that electrons created by an EUV photon are able to ultimately clear. This volume can be calculated simply by dividing the thickness loss at a given dose by the actual dose (e^-/nm^2) to obtain nm^3 cleared per electron. To estimate this value therefore, the incident flux must be known. An estimate for landing current and the integrated charge for the exposure time values used in the experiment were shown previously in this chapter. These values were used to estimate the deprotection volume per electron for the SEM exposures.

The integrated charge vs. exposure time data in an SEM chamber presented earlier in Fig. 4.7 were first converted into the number of incident electrons. Subsequently, these values were converted into area density by normalizing with the area of the exposed fields (42.3 μm X 29.4 μm). Thickness loss vs. dose data were presented earlier using normalized

dose on the horizontal axes. Those data points were mapped to the estimate for incident
flux, and subsequently the volume removed per incident electron were calculated by simply
dividing the thickness removed at each dose by the corresponding dose. Thickness loss as
a function of incident flux used for the calculation is shown for reference in Fig. 4.15. The
calculation results for the amount of cubic nanometers removed are shown in Fig. 4.16. Plot
on the top left shows the amount of volume cleared, while the plot on the top right shows
volume cleared per eV energy for electrons with energy values ranging between 29 eV and
91 eV. In the figure, on the bottom the volume removal data calculated from EUV exposure
contrast curve is also provided for reference. This contrast curve was measured after open
frame exposures performed with the EUV exposure tool available at the Center for X-Ray
Optics (CXRO) at LBNL. The same resist was used for all of these exposures. However, the
EUV and e-beam exposures differed in post-exposure bake (PEB) and dissolution conditions.
The EUV exposed wafer was baked at 100^oC for 90 s, while the e-beam exposed wafers were
baked at 90^oC for 90 s. The EUV exposed wafer was developed for 30 s in TMAH, while
the e-beam exposed resists were baked for 6 s in TMAH. Also, the acids created in the top
few nanometers in electron exposures diffuse both into and out of the resist. The horizontal
axis for the EUV data shown in the figure represents the area density of absorbed photons
calculated using the incident dose values and the EUV absorption constant measured for this
resist using equation 4.2. Here, the incident dose (mJ/cm^2) is converted to eV/nm^2, and α
and r_t are the absorption constant (/nm) and the resist thickness respectively.
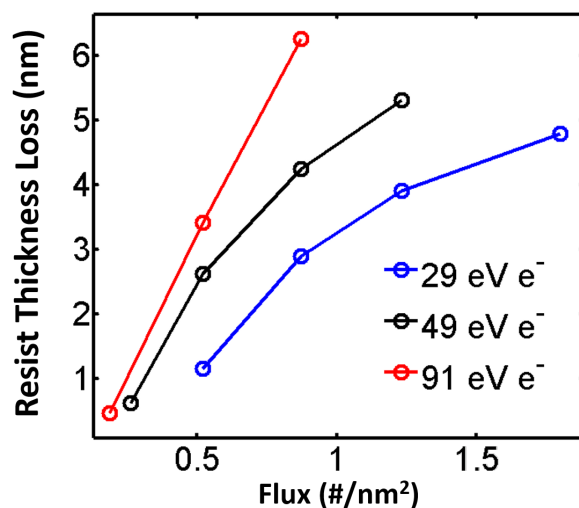
Figure 4.15: Resist thickness loss data for SEM exposures with 33 ms/frame from Fig. 4.10
vs. incident electron flux used for calculation of volume cleared by electrons with three
different energy values

$$\rho_{abs}(\#/nm^2) = \frac{Dose(eV/nm^2)}{92eV/photon} * (1 - e^{-\alpha r_t}) \qquad (4.2)$$

The incident electrons create acids only on the top few nanometers of the resist. There-
fore, the deprotection volume induced by an electron only extends up to 8 nm^3 in this data.
The EUV contrast curve on the other hand clears a much larger volume because in this
scenario absorptions take place in several locations along the thickness of the resist.

The energy delivery capacity per unit energy of electrons can also be quantified by nor-
malizing this volume cleared data with the respective electron energies. These results are
shown on the plot on the right. Volume removed per eV energy per electron is about 0.1 nm^3
per square nanometer. For EUV exposure with the resist processing conditions described
above, at the dose to clear of 8.13 mJ/cm^2 for a 45 nm thick resist the volume cleared per
absorbed photon per eV energy is 0.52 nm^3. Overall trend shows some indication that lower
energy electrons clear a larger volume per unit energy per square nanometer. However, there
is some uncertainty in this conclusion as there are thickness saturation issues in the data.
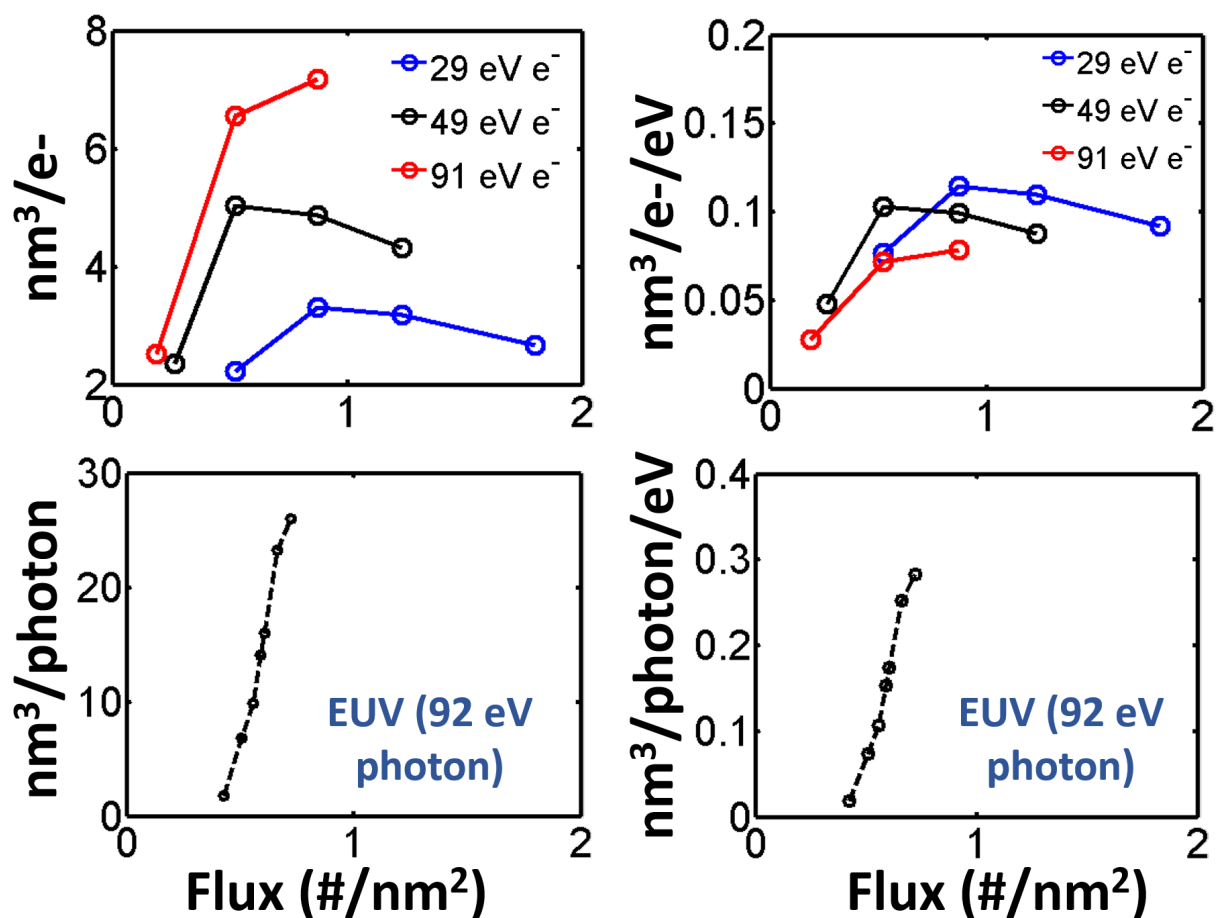
Figure 4.16: Amount of cubic nanometers cleared; **(top left):** Per electron; **(top right):** Per electron per eV energy; **(bottom left):** Per EUV photon; **(bottom right):** Per EUV photon per eV energy. The photon data shows absorbed flux per square nanometers

4.9   Summary

In this chapter, the technique of characterizing the energy delivery capability of low energy (less than 91 eV) electrons by directly exposing thin resist films with these electrons was tested. A leading positive tone chemically amplified EUV resist was exposed with electrons created in a low energy electron microscope (LEEM) tool, as well as a scanning electron microscope (SEM) tool operated in deceleration mode. Dissolution contrast curves were measured for open frame exposures performed with both the tools for energies ranging between 15 eV and 91 eV. Given that electrons at these energies penetrate only a few nanometers, the thickness loss values on the order of 7 to 12 nm seen in the data are due to diffusion of the

acids created by the electrons. With a lower post exposure bake temperature applied on the SEM exposure experiments it was expected that the acid diffusion lengths would be smaller compared to the LEEM experiments due to the Arrhenius trend for temperature dependence of diffusivity. This effect was seen as a difference in the deprotection blur estimated using a simple fitting procedure.

The relative energy delivery capacity of the electrons was determined by simply scaling the dose values in the contrast curve data until a close overlap was obtained in the contrast curve for each energy in relation to a reference energy. These relative ratios that were found were compared against proportionate energy scaling model. From the LEEM exposure data, 15 eV electrons were found to be only 12% as efficient as 30 eV electrons, despite being half as energetic as 30 eV electrons. While a closer examination of charging effects is needed to validate the results, specially at lower electron energies, the SEM based exposure technique provided a better control, since charging effects could be visually detected through the secondary electron image at any given landing energy of the electron. The SEM exposures resulted in energy delivery capacities that were larger than expected from proportionate scaling model as the energy of the electron decreased.

Using a measurement of the current landing on the sample holder in the SEM chamber, the incident flux was estimated and the SEM based resist contrast curve data for 29 eV, 49 eV and 91 eV electrons was used to estimate the cubic nanometer of volume cleared per incident electron per unit energy. The electrons removed about 0.1 nm^3 per eV energy per square nanometer. The spatial extent of the influence of these low energy electrons is of importance from the standpoint of shot noise. Measurement of contrast curve by exposure to low energy electrons appears to be a good technique to extract the parameter.

Chapter 5

Modeling of Low Energy Electron Interactions in EUV Resists

In this chapter, the capability of low energy electrons at depositing energy in chemically amplified resists that can lead to lithographically important chemistry is studied from a modeling standpoint. In order to complement the experimental strategy of performing contrast curve measurements by directly exposing the resist with low energy electrons, here a simulator that models resist thickness loss upon exposure to low energy electrons will be presented. Simulating this mechanism requires modeling the scattering behavior of electrons. Here, the simple analytical dielectric model for inelastic scattering will be applied to simulate the energy deposited by the electron that can lead to the excitation of a photo-acid generator (PAG), which can in turn result in formation of an acid which can then participate in deprotection processes. In the next section, a big picture overview of the simulation of electron trajectories in materials will be provided. Subsequently, the dielectric function based model for inelastic scattering will be described, along with a discussion of the extraction of dielectric function over a wide energy range by using the electron energy loss spectroscopy (EELS) data. Finally, two simulation scenarios will be presented. In the first scenario the number of acids generated by an electron, as well as the spatial distribution of the acid generation sites relative to the point of origin of an electron will be presented. In the electron exposure experiments, acids created by electron interactions in the top few nanometers diffuse during the bake step, and cause deprotection reactions which lead to a solubility switch at depths much larger than the penetration depth of the electrons. These mechanisms can be simulated using a reaction/diffusion solver that models diffusion in small time increments and updates the deprotection level iteratively as a function of time. In the second simulation scenario, the result of thickness loss obtained by using the electron trajectory simulator in conjunction with the SuMMIT algorithm for modeling reaction/diffusion processes that govern the resist bake step extended to 3-D will be provided. The 2-D version of this algorithm was described in chapter 3.

5.1 Overview of The Simulator Model

A block diagram overview of the contrast curve simulator design is presented in Fig. 5.1.
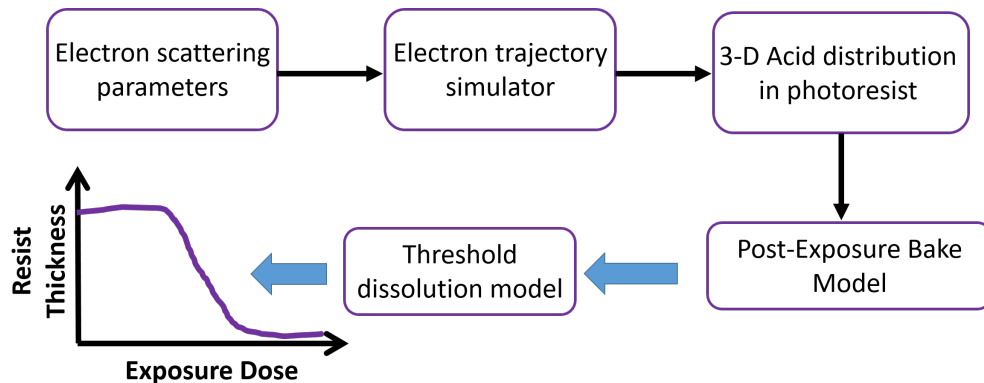
Figure 5.1: Big Picture overview of the contrast curve simulator

5.1.1 Trajectories Traversed by Electrons

The trajectories of electrons are simulated by using the dielectric theory for energy loss of an electron as it inelastically scatters in the sample. Similar model was used by Villarubia [50] for modeling secondary electron emission in a scanning electron microscope, and Biafore et. al. [51] for simulating the secondary electron image produced by an EUV photon absorption event in the resist. An electron that enters the sample in the low energy exposure experiment is given a fixed directionality orthogonal to the surface normal of the sample. The distance that the electron travels before undergoing a scattering event is treated as a Poisson process with a given mean free path, which is the parameter extracted from the dielectric model to be described later. The probability density function (f(x)) and the cumulative density function (F(x)) for a Poisson process with a mean free path of λ are provided in equation 5.1. The random distance traveled, x, can be generated using the standard procedure of randomly sampling a fraction uniformly distributed between 0 and 1, and inverting F(x) at this random value. For instance, if the randomly sampled fraction is denoted by α, then, the step length is $x_{step} = \lambda \ln(1-\alpha)$. The expected value for the Poisson process $E[x] = \int_0^\infty x f(x) dx = \lambda$, while the variance is $\sigma_x^2 = E[x^2] - (E[x])^2 = \lambda^2$.

$$f(x) = 1/\lambda e^{-x/\lambda}$$
$$F(x) = 1 - e^{-x/\lambda}$$

$$(5.1)$$

5.1.2 Modeling Events Caused by Electrons

The actual energy deposited by an electron at a scattering site is sampled from the energy-differential cross-section distributions that will be presented later. If the deposited energy is smaller than 5 eV, it is treated as an unfruitful event as the typical PAG excitation energy is 5 eV. If the deposited energy is larger than the ionization potential (12 eV), then the most likely event is the generation of a secondary electron. Energy of the secondary electron is simply the difference between the deposited energy and the ionization potential of the sample. There is however a finite probability that the deposited energy is transfered to the photo-acid generator (PAG) leading to creation of an acid. Which of these two events occurs is determined probabilistically by using the relative number densities of PAGs and the monomer units. The PAGs are loaded in these simulations at 6.2% by volume. Therefore, for example if a randomly sampled number distributed uniformly between 0 and 1 results in a value less than and equal to 0.062, then the electron causes an acid creation event, else it creates a secondary electron.

For energy losses between 5 eV and the ionization potential (12 eV), the existing model in the literature is to treat the deposited energy as an acid creation event if there is a PAG within the reaction radius of the electron's co-ordinate [52][53]. Kozawa et. al. suggested a reaction radius value of 2 nm [54] for a triphenyl sulfonium triflate (TPS-Tf) PAG in a polyhydroxystyrene based polymeric resist. This simplified model however, likely assumes acid creation due to both direct excitation of the PAG by the electron as well as indirect excitation. Indirect excitation refers to the mechanism where the electron excites the monomer unit in the polymer chain, which then transfers the energy to a PAG that may be present in the vicinity. When estimating the acid yield upon exposure to 193 nm wavelength (6.44 eV) photons, Houle et. al. [31] also noted that the polymer absorbs as strongly as the PAGs at these energies. As an example, the EELS data for a chemically amplified resist that was presented in chapter 2 is shown in Fig. 5.2 for energy absorption in the 3 eV to 12 eV regime. Typical PAG excitation energy of 5 eV is annotated along with the major peak at 6.5 eV, which is likely due to the monomer units in the material. Since the typical number densities of PAGs are much lower than the polymer, Houle et. al. [31] hypothesized the likely contribution of energy deposited in the polymer in leading to the typically measured acid yields through sensitization processes. Hacker et. al. [55] conducted some of the early experimental investigations by studying the flourescence properties of polymer films containing t-boc protecting groups with varying volumetric densities of PAG loading. With an increase in the PAG loading, the flourescence intensities were found to decrease. As an explanation, the authors proposed that quenching of the polymer excited state was due to sensitization of the PAGs by the polymer through electron transfer.
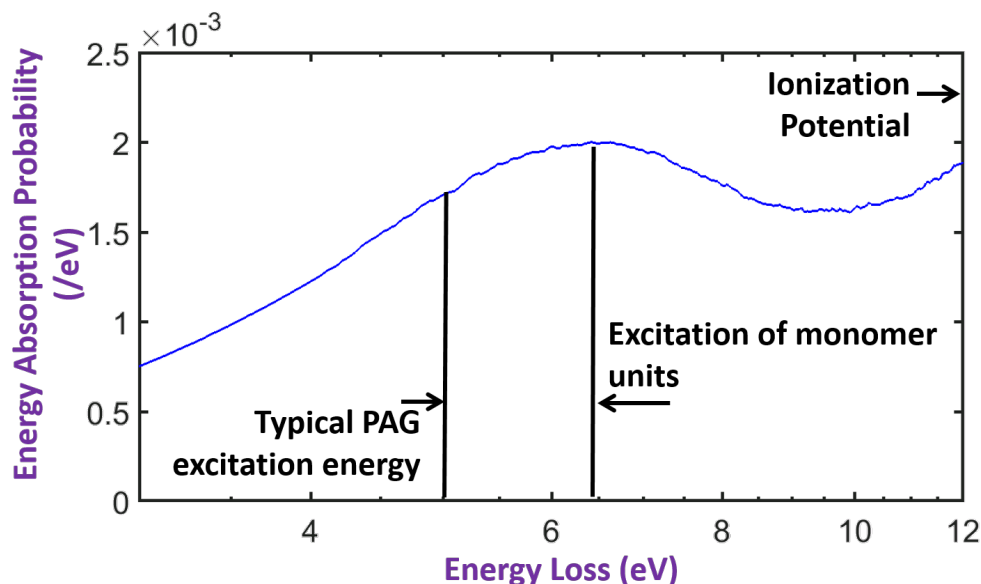
Figure 5.2: Measured EELS spectrum of a chemically amplified resist in the 3 to 12 eV energy loss regime

5.1.3 Model for 3-D Simulation of Reaction/Diffusion Mechanism in the Resist

In this study, The reaction/diffusion algorithm implemented in the SuMMIT resist simulator described in chapter 3 (equations 3.2) was extended to 3-D for calculating the deprotection profile which can be used to calculate the resist thickness loss upon exposure to low energy electrons. Acid distribution resulting from the electron trajectory simulator is provided as input to the reaction/diffusion model, along with a 3-D distribution of base and protected polymer sites in the resist. The model then applies diffusion and reaction operators described in chapter 3. The total post-exposure bake time is divided into N steps, such that the diffusion length for a given time step is $\sigma_{step} = \sigma_{tot}/\sqrt{(N)}$. This diffusion step is modeled as a 3-D Gaussian convolution applied on the acid and base matrices. In order to speed up the convolutions, the Gaussian kernel matrix size is chosen to be large enough to include only $\pm 3\sigma_{step}$. This is a reasonable approximation considering that 99% of the area under the Gaussian function falls within ± 3 standard deviations.

5.2 Dielectric Model for Inelastic Scattering of Electrons

One of the most widely used models of the inelastic interaction of electrons in solids is the dielectric model, which describes the scattering of electrons off of the valence electrons in the medium. Some of the early expositions of the model were provided by Ritchie [56], and a review is provided by Dapor [57]. The theory was originally developed for modeling the scattering of highly energetic electrons in solids. Many authors [58][59][60][61] have since applied the analytical framework to estimate the mean free path of electrons with energies less than 100 eV. Tanuma et. al. did calculations with dielectric data from literature for 14 organic compounds [62], 15 inorganic compounds [63] and 41 elemental solids [64]. The authors also gave empirical formulae for mean free path for electrons with energies larger than 50 eV for each elemental solid. In the dielectric model, the inverse mean free path for a moving electron to cause an electronic excitation in the material per unit distance traveled per unit energy deposited is given by equation 5.2 [50] [57]. In this equation, a_o is the Bohr radius (53 pm), E is the energy of the electron in motion, E_{loss} is the energy lost by an electron during a collision event, and q is the momentum transfered. Im[-1/$\epsilon(q, E_{loss})$] is defined as the energy loss function of the material that characterizes the absorption properties of material for an energy loss of E_{loss} and momentum transfer of $\hbar q$. $\epsilon(q, \omega)$ is the complex dielectric function of the material. The scattering cross-section, which is another useful parameter this usually of interest, is simply the inverse mean free path divided by number density of the scattering molecules in the sample.

$$\frac{d^2\lambda^{-1}}{dE_{loss}dq} = \frac{1}{\pi a_o E} Im\Big[\frac{-1}{\epsilon(\mathbf{q}, E_{loss})}\Big]\frac{1}{q} \tag{5.2}$$

5.3 Probabilistic Determination of Energy Loss and Scattering Angles at a Scattering Site

For simulating the trajectories of electrons, in addition to the mean free path, the energy lost by the electrons in a collision event and the angles of scattering are also needed. These parameters can be extracted by using the analytical model shown in equation 5.2 in conjunction with the energy-momentum conservation laws. Diagrams for inelastic scattering are provided in Fig. 5.3. An electron with a given energy, velocity and momentum [E_i,v_i,$\hbar k_i$], scatters off a molecule, imparting some energy (E_{loss}) and momentum ($\mathbf{q}$) to it, thus emerging with a lower energy, velocity and momentum [E_f,v_f,$\hbar k_f$].
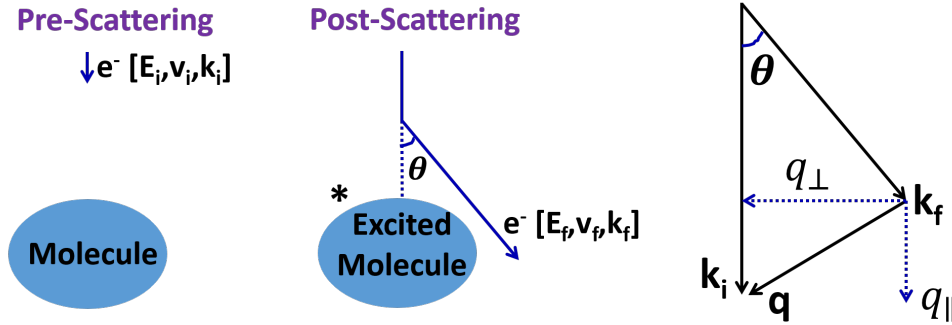
Figure 5.3: Inelastic scattering diagrams

The momentum-differential inverse mean free path can be converted into angle differential inverse mean free path by utilizing the energy-momentum conservation laws. Applying the conservation rules to the scattering diagram shown to the right in Fig. 5.3, we get:

$$q^2 = k_i^2 + k_f^2 - 2k_i k_f cos(\theta)$$
$$\frac{dq}{d\theta} = \frac{k_i k_f sin(\theta)}{q} \tag{5.3}$$

Here, the initial and final electron momenta are $k_i^2 = 2mE_i/\hbar^2$, and $k_f^2 = 2mE_f/\hbar^2 = 2m(E_i - E_{loss})/\hbar^2$, respectively. Plugging the expression for dq from equation 5.3 into equation 5.2, equation 5.4 can be obtained.

$$\frac{d\lambda^{-1}}{dE_{loss}} = \frac{1}{\pi a_o E} Im\left[\frac{-1}{\epsilon(\mathbf{q}, E_{loss})}\right] \frac{k_i k_f sin(\theta) d\theta}{q^2} \tag{5.4}$$

Finally, using the solid angle ($d\Omega = 2\pi sin(\theta) d\theta$), equation 5.5 describes the energy and angle-differential inverse mean free path.

$$\frac{d^2\lambda^{-1}}{dE_{loss}d\Omega} = \frac{1}{2\pi^2 a_o E} Im\left[\frac{-1}{\epsilon(\mathbf{q}, E_{loss})}\right] \frac{k_i k_f}{q^2} \tag{5.5}$$

Integrating $d^2\lambda^{-1}/dE_{loss}d\Omega$ for all possible angles yields the energy loss-differential inverse mean free path $d\lambda^{-1}/dE_{loss}$. Similarly, integrating the double differential inverse mean free path for all allowed energy loss values yields the angle-differential inverse mean free path. These distributions can be used as probability distributions to generate random energy loss and scattering angles that characterize the scattering parameters at the collision site.

The inverse mean free path can be calculated from equation 5.2 by integrating the double differential cross-section over all allowed energy loss values and all allowed momentum

transfer values, as shown in equation 5.6. The momentum integration limits for this integration can be extracted from the conservation law for q^2 in equation 5.3 by applying the limits $\cos(\theta)=\pm 1$. The momentum integration limits are thus $q_{min}=\sqrt{(2m_e E_i)}/\hbar$ - $\sqrt{(2m_e(E-E_{loss}))}/\hbar$ and $q_{max}=\sqrt{(2m_e E_i)}/\hbar + \sqrt{(2m_e(E-E_{loss}))}/\hbar$. The inverse inelastic mean free path for an electron at a given energy can also be evaluated by integrating the double-differential inverse mean free path from equation 5.5.

$$IIMFP = \frac{1}{\pi a_o E} \int_{E_{min}}^{E_{max}} \int_{q_{min}}^{q_{max}} \frac{1}{q} Im\left[\frac{-1}{\epsilon(\hbar q, E_{loss})}\right] dq dE_{loss} \tag{5.6}$$

5.4 Limitations of the Dielectric Model for Scattering

The dielectric model for inelastic scattering describes the probability of interaction between an electron in motion and the valence electrons in the solid, and places a limit on the largest possible energy loss, the E_{max} in equation 5.6: $E_{max} = E_i$ - E_F, where E_i represents the energy of the incident electron, and E_F is the Fermi energy of the solid [60][61]. E_F is defined as the energy level where the probability of occupation is 50% assuming Fermi-Dirac statistics, which is a model for describing the probability of an allowed energy level being occupied by electrons. This probability density function is given by equation 5.7.

$$f(E) = \frac{1}{1 + e^{(E-E_F)/kT}} \tag{5.7}$$

The expression for Fermi energy (E_F) is provided in equation 5.8 [58], where ρ_{elec} is the volumetric density of valence electrons and a_o is the Bohr radius (53 pm). For a resist system with a poly-hydroxy-styrene (C_8H_8O) backbone polymer, the molecular mass (M_w) of the monomer unit is 120 g/mol. Assuming the typical density (ρ) of 1.19 g/cm^3, we get $\rho_{elec}=\rho/M_w*Na*N_{valence}$, where Na is Avogadro's number and $N_{valence}$ is the number of valence electrons per molecule, which is 46 for C_8H_8O. Using these numbers, the Fermi energy estimate is 15.5 eV. Tanuma et. al. [65] reported the Fermi energies for several elemental solids. Among them, Fermi energy for carbon is reported as 20.4 eV. This number is larger than the estimate provided here because ρ_{elec} reported in [65] is 47% larger than that for the resist. The value of E_{min} in equation 5.6 is the lowest energy that can lead to an electronic excitation, and a value of 0 is typically used for metals [60]. For insulators however, the bandgap value is typically used [58]. In the model here, the energy integral in equation 5.6 is carried out with $E_{min}=0$, but the decision of treating energy loss events less than a threshold (e.g. 6 eV event as seen in the EELS data) as unfruitful events is performed in the electron trajectory simulator.

$$E_F = \frac{13.606eV}{\left(\left(\frac{4}{9\pi}\right)^{1/3} r_s\right)^2}$$

$$r_s = \left(\frac{4}{3}\pi \rho_{elec}\right)^{-1/3} / a_o$$

(5.8)

5.5 The Mermin Dielectric Functions

The dielectric model for scattering described above clearly requires knowing the complex dielectric function and hence the energy loss function (Im[-1/$\epsilon(q,\omega)$]) of the material. However, the energy loss function that can be most easily measured is the energy loss function in the optical limit (small q). Therefore, the technique that is most widely used for predicting electron scattering behavior is to approximate the q-dependence of the dielectric function using analytical models. One such analytical model for the dielectric function of a material that has explicit dependence on momentum transfered to the material is the Mermin dielectric function. This function in turn builds upon the Lindhard dielectric function, and accounts for the fact that plasmons generated in solids can have finite lifetimes [59] which result in a broadening of the plasmon resonance peak when measured with an EELS tool. Definition of the function is provided in equation 5.9, where ϵ_L is the Lindhard dielectric function.

$$\epsilon_M(k,\omega) = 1 + \frac{(1 + j\gamma/\omega)[\epsilon_L(k,\omega+j\gamma) - 1]}{1 + (j\gamma/\omega)[\epsilon_L(k,\omega+j\gamma) - 1]/[\epsilon_L(k,0) - 1]}$$

(5.9)

By measuring the energy loss function of the material in the optical limit (Im[-1/$\epsilon(q = 0, E_{loss})$]), a fit can be performed on the measurement with a linear combination of analytical Mermin energy loss functions evaluated at low values of q. A linear combination is required because most materials may have multiple absorption peaks in addition to the main bulk plasmon peak in the 15-30 eV regime. The fitting relationship is described in equation 5.10, where A_i, E_i and γ_i are the fit parameters that represent the strength of the oscillator, the center energy of the oscillator and the width of the oscillator, respectively. Abril et. al. [59] demonstrated this technique for four materials. Bourke et. al. performed these calculations with both directly measured optical dielectric function, as well as dielectric functions evaluated from first principles using density functional theory [60][61]. Dapor [66] performed these calculations for poly-methyl-methacrylate (PMMA).

$$Im\left[-\frac{1}{\epsilon(q=0,\omega)}\right] = \sum_i A_i Im\left[-\frac{1}{\epsilon_M(q=0,E,E_i,\gamma_i)}\right]$$

(5.10)

5.6 Measurement of the Energy Loss Function of the Resist for 2 - 100 eV Regimes

Electron energy loss spectroscopy can be used to measure the optical properties of thin films. Dielectric function based description of the scattering of electrons described by Ritchie [56] can also be applied to EELS, and used for estimating the dielectric function of the material. The instrument-broadened single scattering distribution, described by Egerton [8], is given in equation 5.11. In this equation, I_0 is the zero-loss integral sum, t is the sample thickness, a_0 is the Bohr radius (53 pm), v is the velocity of the incident electron, β is the collection angle (12 mrad for our data), θ is the scattering angle, and θ_E is the characteristic angle for scattering for a given energy loss. When the energy loss values are much smaller than the energy of the incident electron energy, the characteristic angle for scattering at a given energy loss can be approximated as $\theta_E = E/(\gamma m_0 v^2)$ [8], where γ is the relativistic correction factor, and its value is 1.2 for 120 keV electrons.

$$SSD(E) = \frac{I_0 t}{\pi a_0 m_0 v^2} Im\left[\frac{-1}{\epsilon(E)}\right] \int_0^\beta \frac{\theta}{\theta^2 + \theta_E^2} \tag{5.11}$$

The procedure for extracting the single scattering distribution from the measured plural scattering distribution is to use the fourier log deconvolution (FLOG) technique described by Egerton [8]. Equation 5.11 suggests a simple way of calculating the energy loss function (Im[-$1/\epsilon$]) directly from the single scattering distribution. However, surface plasmon scattering probabilities need to be subtracted from the measured single scattering distribution, as they can lead to a slight reduction in the intensity of the bulk plasmon signal. The analytical models for probabilitiy of surface plasmon scattering are described and implemented in software by Egerton [8].

The energy loss function extracted from the EELS data is shown in Fig. 5.4. The Mermin dielectric functions used for performing a fit using the model in equation 5.10 are also shown, and the linear combination of these Mermin functions is also overlaid on the curve extracted from the EELS measurement. The fit was performed with a least squares error minimizer, and the fit parameters are provided in the inset of the figure. Both lower and upper bounds were provided as constraints on the center energies for the first two Mermin functions (E_1 and E_2) such that a Mermin function would be placed at energies where clearly visible peaks are seen in the data. For all of the other variables, a lower bound of zero was provided, and no upper bounds were provided. As seen in the figure, the main peak at 23.22 eV is 10.69 eV wide, while the 6.22 eV peak is 3.14 eV wide. The 32 eV oscillator was needed to better fit the tail of the plasmon peak, and it is 26.49 eV wide. The 295.7 eV oscillator was provided to fit the ionization edge of carbon, and is much weaker in strength than all the other oscillators.
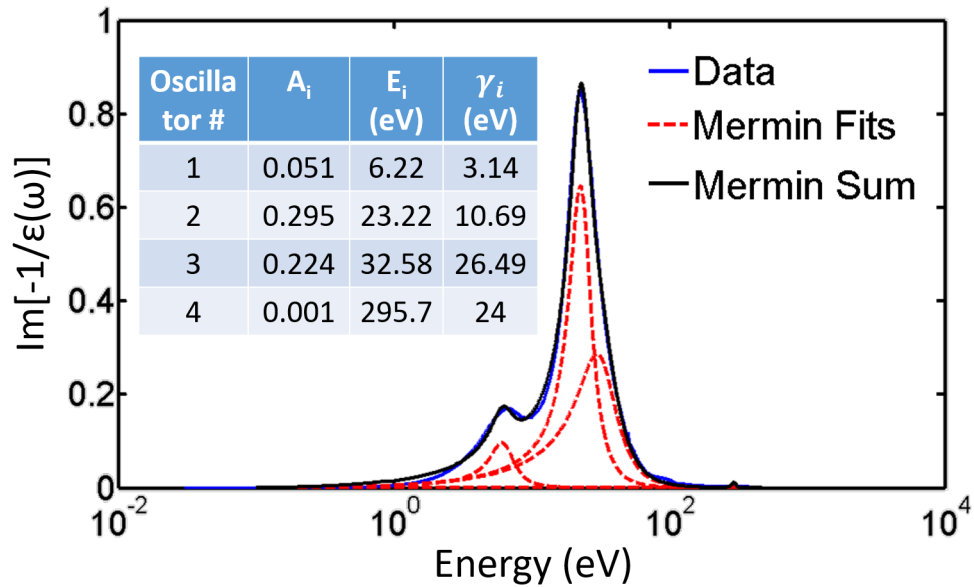
Figure 5.4: Energy loss function (Im[-1/ϵ]) of an EUV resist extracted from EELS data

5.7 Resist Scattering Parameters Used in the Electron Trajectory Simulator

5.7.1 Inelastic Mean Free Path

The inelastic mean free path is one of the parameters used in the simulator, and it describes the expected distance between scattering events. A plot of the mean free path calculated by inverting equation 5.6, in conjunction with equation 5.10, and using the Mermin dielectric function fit parameters from Fig. 5.4, is provided in Fig. 5.5. The curve has the overall shape of the universal mean free path curve [67], where below around 60 eV, with decreasing energy the mean free path increases indefinitely.
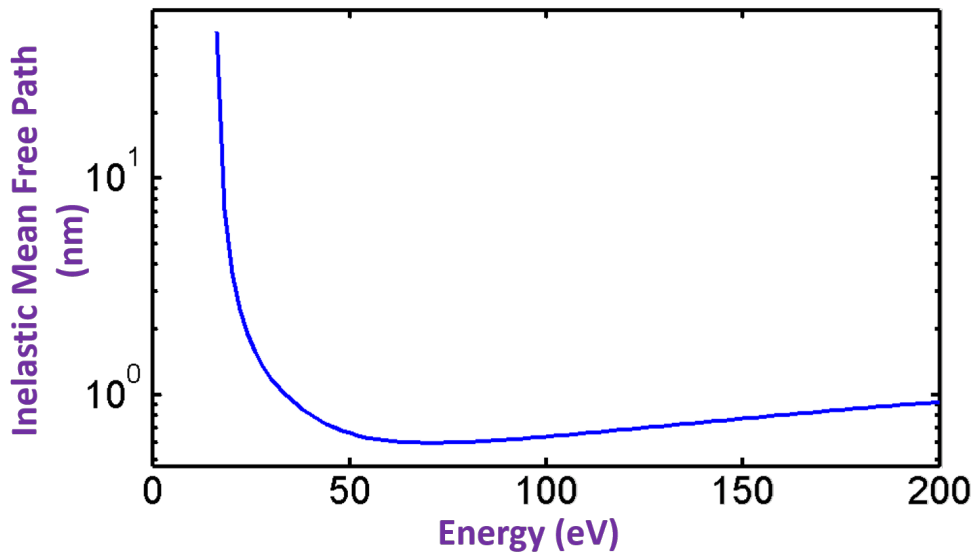
Figure 5.5: Inelastic mean free path calculated using the Mermin dielectric functions

5.7.2   Scattering Cross-Sections

The other two parameters used in the simulator are the energy loss and the scattering angle cross-sections, calculated using the double differential cross-section described in equation 5.5. The plots for these distributions are provided in Fig. 5.6, the energy loss distribution on the left and the scaterring angle distribution on the right. Results are provided for four incident electron energies ranging from 26 eV to 100 eV. The maximum energy loss for each incident energy is set to be the incident energy minus the Fermi energy of 15.5 eV as described earlier. As seen from the energy loss distribution, with decreasing electron energy, the limits of integration drop. Even though the net scattering cross-section for a given energy loss goes up slightly, the net integral drops, and this causes the mean free path to increase with decreasing energy below around 60 eV.
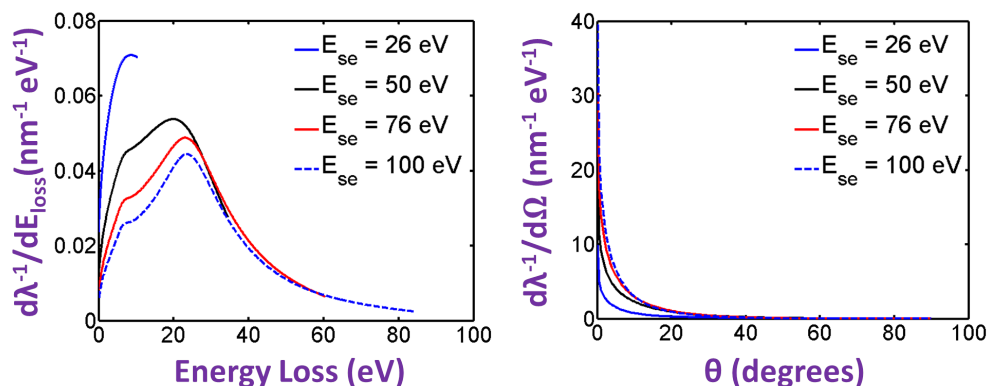
Figure 5.6: Energy loss and scattering angle distributions based on the dielectric model for inelastic scattering of electrons

5.7.3 Mean Free Path at Low Energies

The inelastic mean free path curve clearly shows a rapidly increasing mean free path as the energy approaches the Fermi energy of the material, estimated earlier to be 15.5 eV for the EUV resist being studied. Experimental measurement of the mean free path at these low energies is a topic of research. Bourke et. al. [68] proposed using the technique of x-ray absorption fine structure (XAFS) for estimating the low energy mean free path of photo-electrons by performing a fitting procedure on the oscillations that appear next to an absorption edge. The inelastic mean free path estimate for copper was found to have the overall shape of the universal mean free path curve, but was found to increase rapidly only around 5 eV. Mean free path calculated using the Mermin dielectric functions was found to over-predict the mean free path by 0.3 nm at 20 eV and and by 1 nm at 10 eV [69]. For energies larger than 50 eV the XAFS based technique and the Mermin function based technique were found to be in very close agreement.

Other scattering mechanisms may also be important for scattering of low energy electrons. One possible mechanism is that of vibrational scattering. Llacer and Garwin built upon the analytical models for electron-phonon scattering by Fröhlich [70], and derived the scattering mean free path for the creation and annihilation of longitudinal optical phonon modes. The authors also presented a Monte Carlo model to simulate the emission of electrons from alkali halide solids [70]. Dapor used the analytical model in combination with the dielectric function based model to estimate the mean free path at energies below 25 eV for silicon dioxide [71]. The author also showed that using the simple analytical model for phonon scattering caused the mean free path curve to decrease at energies below around 25 eV. Villarubia used the analytical electron-phonon scattering formula in conjunction with other scattering mechanisms in a Monte Carlo model for simulating scanning electron microscope (SEM) images [50]. In polymeric resists, vibrational processes can include modes associated

with for example stretching of the CH_2 that forms the backbone polymer chain, stretching of the carbon-carbon bonds etc. Khakoo et. al. used an angle-resolved low energy EELS tool with an energy resolution of 60 meV full-width at half maximum to measure the energy and angle-differential cross-sections for vibrational modes excited in gas phase tetrahydrofuran (C_4H_8O) by electrons with energies ranging between 2 eV and 20 eV [72]. By tabulating all the vibrational modes ranging from 84 meV to 796 meV, the authors found the integrated cross section to maximize at 10 eV, and decrease on both sides of this energy. Considering that mean free path is the number density of scattering sites divided by the integrated cross section, the data provided by Khakoo et. al. [72] results in an increase of the mean free path with decreasing energies below 10 eV.

5.8   Simulation Scenarios

Two simulation scenarios were considered. First, acid generation by electrons was simulated with the motive of determining both the acid yield statistics as well as the spatial extent of the regions where acids are created by electrons. In the second set of calculations, resist thickness loss as a function of electron exposure dose was simulated. In these simulations, the three-dimensional acid distribution calculated by the electron trajectory simulator was provided as an input to a three-dimensional reaction/diffusion solver that accounts for post exposure bake mechanisms, to calculate the three-dimensional deprotection levels in the resist.

As described earlier, when simulating the trajectories of electrons, at scattering sites the amount of energy deposited is treated as a random variable with a distribution given by the energy-differential cross section described by equation 5.4. This value is obtained by using a custom random number generator. This generator uses the standard procedure of picking a uniformly distributed random fraction between 0 and 1, and inverting the cumulative distribution function that corresponds to the energy differential cross-section at this value. In Fig. 5.7, it is shown that this procedure is working correctly. Blue bars represent the relative counts for the sampled energy loss values that were used in the simulator. Red lines show the analytical energy-differential cross-section for each of the two energies shown in the figure. A close agreement is found between the histograms and the analytical function.
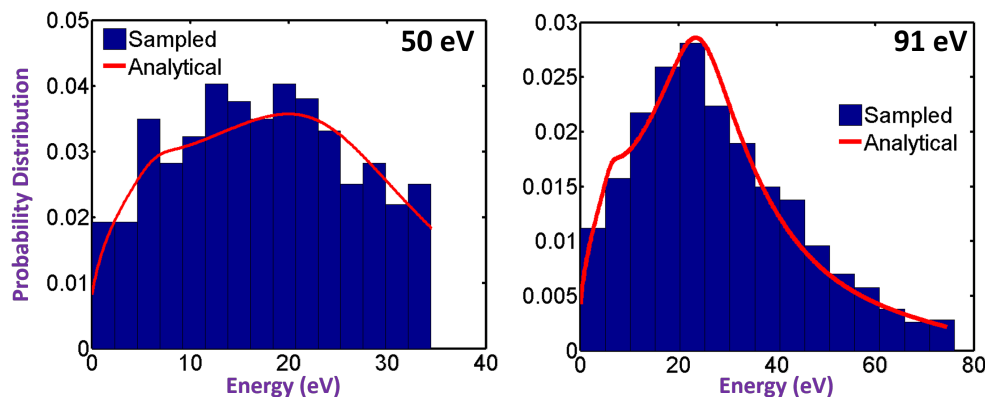
Figure 5.7: Demonstration of the outcome of energy sampling at the scattering site by electrons at 50 eV and 91 eV

5.8.1 Acid Yield and Spatial Distribution as a Function of Electron Energy

The parameters pertaining to electron interactions in resists that are of importance are the net acid yield and the distances over which electrons create the acids.

5.8.1.1 Net Acid Yield

The number of acids generated by electrons with energies between 30 eV and 91 eV was calculated by placing an electron at the center of a 50 nm x 50 nm x 50 nm volume element, and tracking its trajectories and the number of acid generation events triggered by it. A total of 1024 independent trials were simulated. The electron in each trial was initially given uniformly distributed random polar and azimuthal angles. The subsequent scattering angles were computed following the framework described earlier. Monomer number density of $6/nm^3$, PAG density of $0.4/nm^3$ and a voxel volume of $1 nm^3$ were assumed. Statistics of number densities were modeled using the Poisson distribution. Grids containing the photoacid generator sites and the monomer unit sites were initialized and randomized for each of the independent trials. Example images of the mean number of monomer sites and the photo-acid generators used in simulation averaged along the y-dimension are provided in Fig. 5.8.
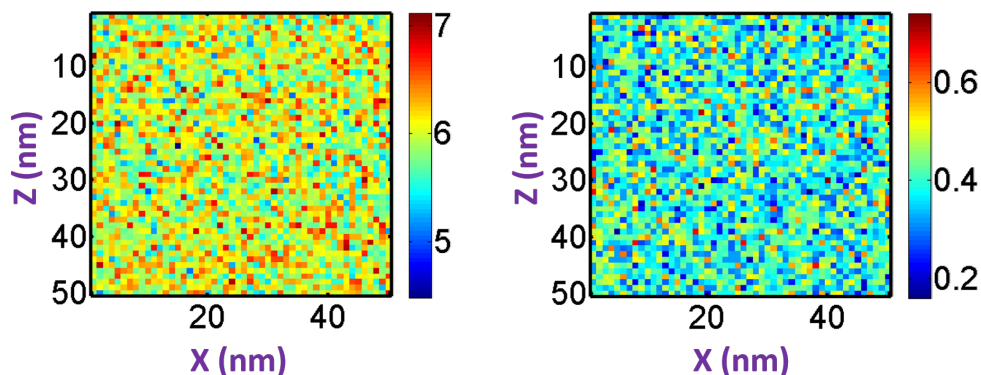
Figure 5.8: Number densities per pixel of monomer sites **(left)** and photo-acid generators **(right)** used in the simulation of acid generation events

The acid generation statistics for electron energies ranging between 30 eV and 91 eV
are shown in Fig. 5.9. The horizontal axes represent the number of acid creation events
and the vertical axes represent the normalized frequency for each of these events from 1024
independent trials. Compared to the other three energies, for 30 eV electrons the probability
of creating one acid is much larger in relation to other acid counts. This occurs because in
the model electrons are being tracked down to only an energy of 20 eV due to the lack of a
model to account for scattering at lower energies in this material. As a result, contributions
of the secondary electrons that may be created with energies less than 20 eV are not being
accounted for. With increasing energy, the relative frequency of more than one acid creation
goes up. The probability of zero acid creation ranges between about 20% to about 30%.
This number would also decrease if models for movement of electrons at lower energies were
included. The mean number of acids are also annotated in the plots, and show an increasing
trend with increasing energy as expected.
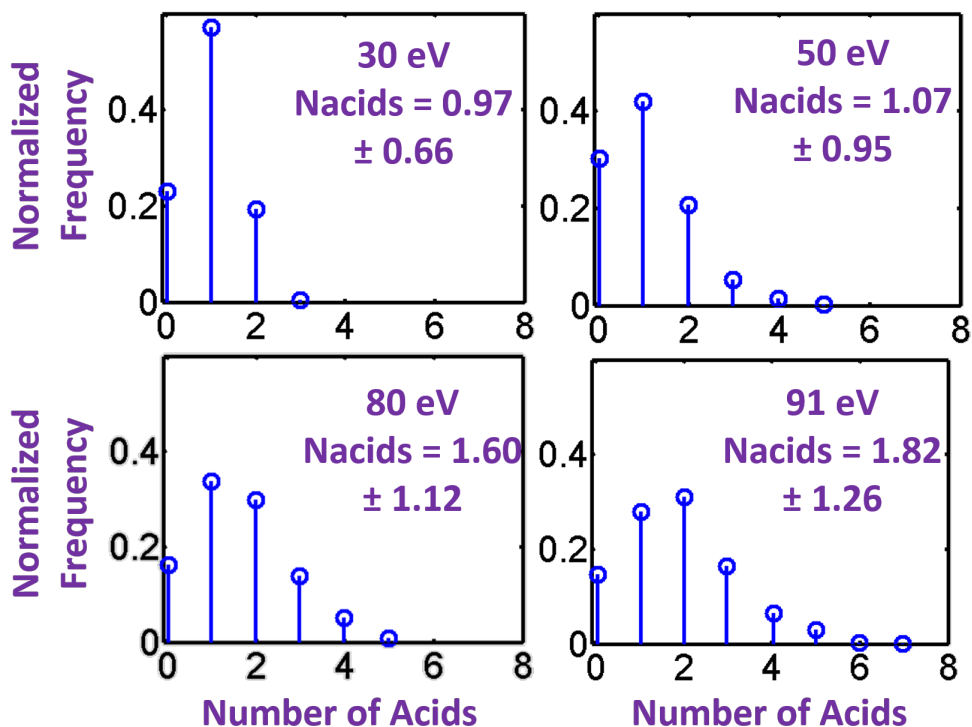
Figure 5.9: Acid generation statistics for electrons with energies between 30 eV and 91 eV from 1024 independent trials

The key objective of the simulation study presented in this chapter is to complement the experimental technique that was presented in chapter 4. Therefore, we seek to calculate the number of acids created per eV energy. Plot on the left in Fig. 5.10 shows the number of acids created per electron, using the results from Fig. 5.9. The plot on the right shows the number of acids normalized by the secondary electron energy. Due to the saturation in the acid count at lower energies, the acids created per eV increases at lower energies to about 0.032/eV at 30 eV, compared to about 0.021/eV at 50 eV. Compared to 91 eV electrons, these results show that the 30 eV electrons produce about 1.6 times more acids per eV energy. The 50 eV electrons produce only about 1.1 times more acids per eV compared to 91 eV electrons.
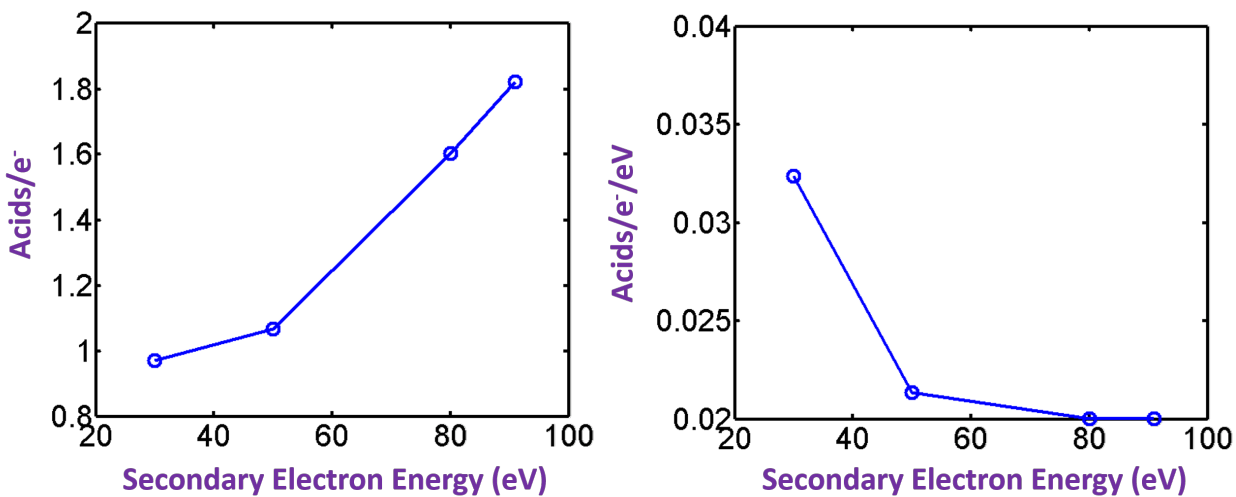
Figure 5.10: Acid yield for various electron energies; **(left):** Yield per electron; **(right):** Yield per electron per eV energy

5.8.1.2 Spatial Extent of Acid Generation Sites

Spatial distribution of the acid generation sites for all 1024 trials for 30 and 50 eV electrons are illustrated in Fig. 5.11, and those for 80 and 91 eV electrons are shown in Fig. 5.12. Images on the top show Z-X cross-section views where the total number of electrons along the y dimension have been added up. Images on the bottom show X-Y top views, where the total number of electrons along the z dimension have been added up. The total number of acids were divided by the number of trials (1024), so the color scales represent the number of acids per electron.
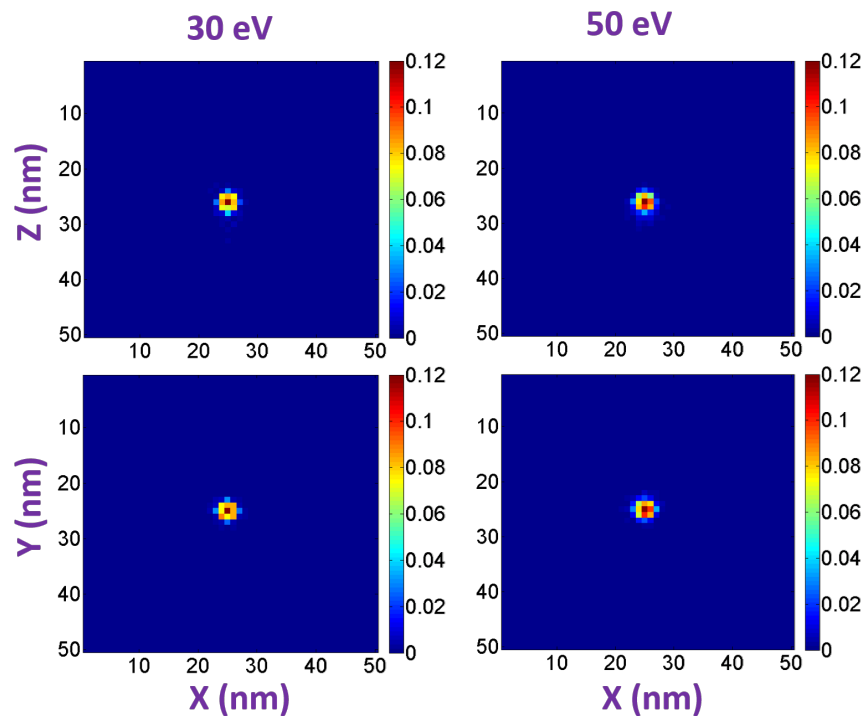
Figure 5.11: Spatial profile of acids created per electron from 1024 independent trials for energies of 30 eV **(left)** and 50 eV **right**
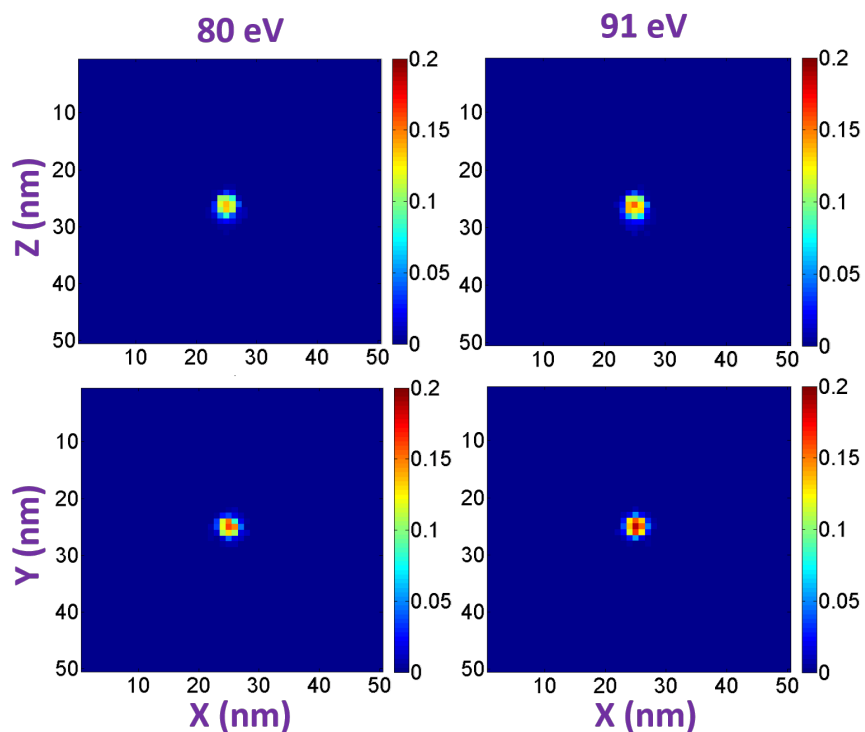
Figure 5.12: Spatial profile of acids created per electron from 1024 independent trials for energies of 80 eV **(left)** and 91 eV **right**

Probabilistic nature of the scattering process and the randomized spatial distribution of photoacid generators result in a randomization of the sites where photo-acids are activated by the electrons that may be created by an EUV absorption event. This effect is seen pictorially in Figs. 5.11 and 5.12. Co-ordinates of the acid generation sites were tracked in simulation, and the radii of these sites relative to the point of origin of the electron were calculated. Histograms are shown in Fig. 5.13. Average distances where the acids are generated are 2.05 nm for the largest energy simulated here (91 eV), and 1.80 nm for the smallest energy (30 eV). The standard deviations range between 0.96 nm and 1.12 nm.
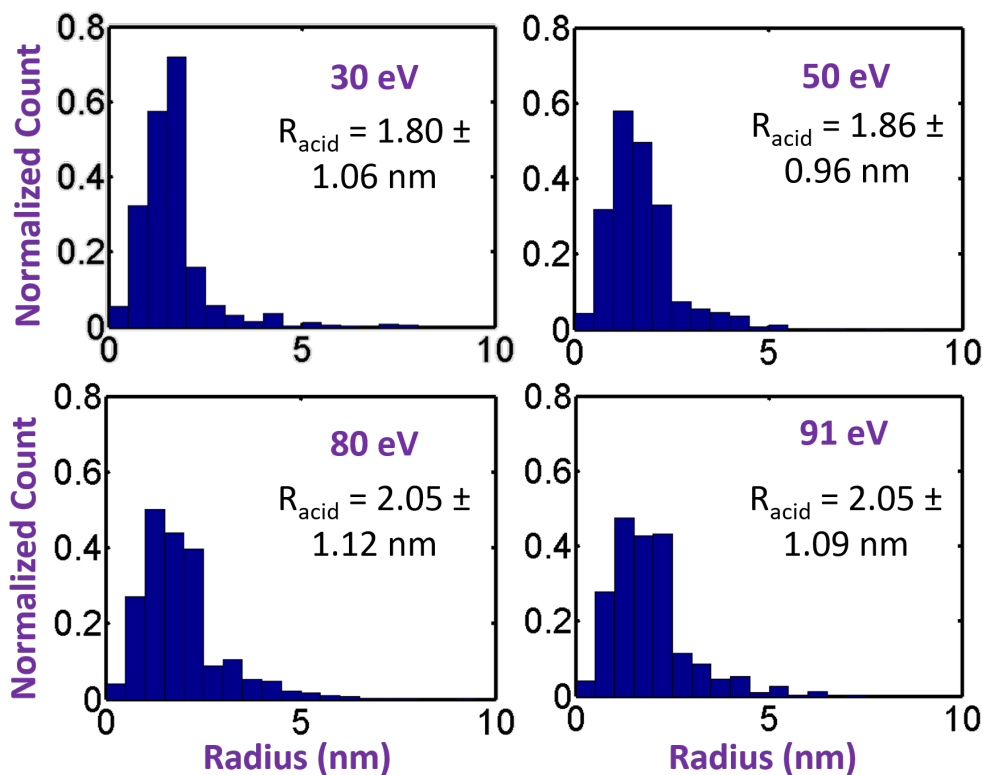
Figure 5.13: Histograms of acid generation site radius relative to the point of origin of the primary electron

The radius of acid generation sites relative to the point of origin of the electron has the same qualitative shape found by Gronheid et. al. [34] in their simulations of an 80 eV electron created by absorption of an EUV photon. An analytical fit can be performed on the distribution of the acid generation radii. The usefulness of this is that it can be used as an analytical blur function in simpler resist simulators that may not take into account electron trajectories. The Rayleigh probability distribution function described in equation 5.12 was used. A least squares fit was performed for the parameter σ in this function for each of the four energies. In Fig. 5.14, for each energy the normalized count values from Fig. 5.13 are plotted as circles, while the best fit Rayleigh functions are plotted as black dashed lines. The best fit σ values have been annotated in the plots for each energy, and are found to increase from 1.2 nm at 30 eV to 1.41 nm at 91 eV.

$$f(x) = \frac{x}{\sigma^2} e^{-x^2/(2\sigma^2)} \tag{5.12}$$
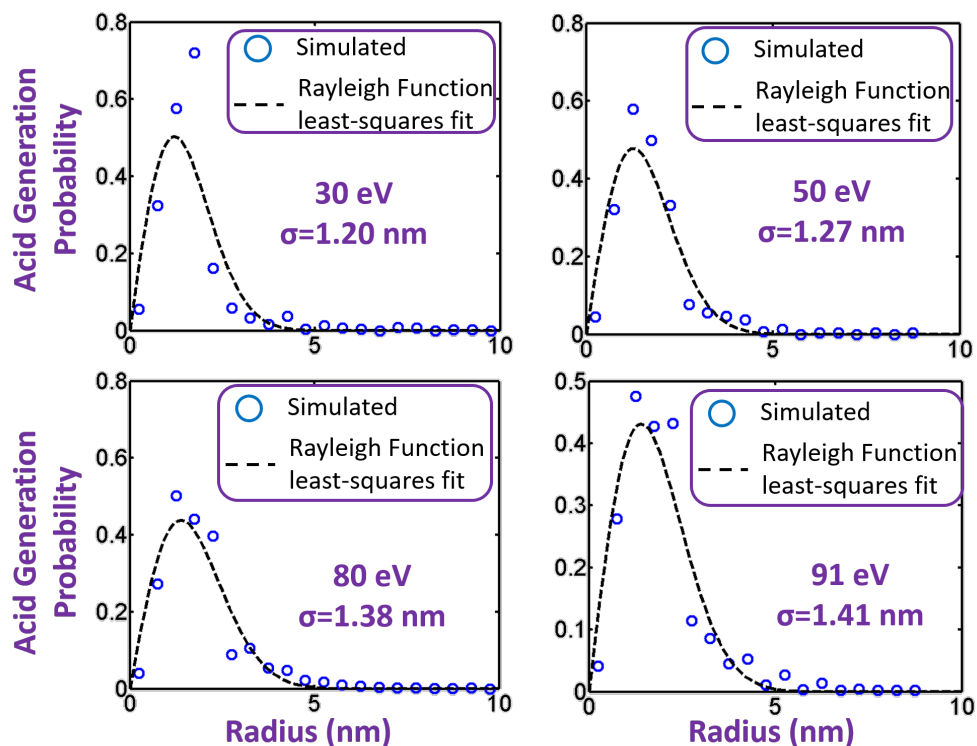
Figure 5.14: Least squares fitting of three-dimensional acid generation radii statistics with
a Rayleigh distribution

In addition to calculating the probabilities for acid generation radius in 3-D space, the
probability for the radius in 2-D space was also calculated. The utility of this calculation is
that the results can be used as a model for acid generation radius in 2-D resist simulators
that may not track electrons. The z-x cross-section views shown in Figs. 5.11 and 5.12 were
used for this purpose. The results are shown in Fig. 5.15. The best fit σ values for the
Rayleigh functions are found to increase from 0.87 for 30 eV electrons up to 1.04 nm for 91
eV electrons.
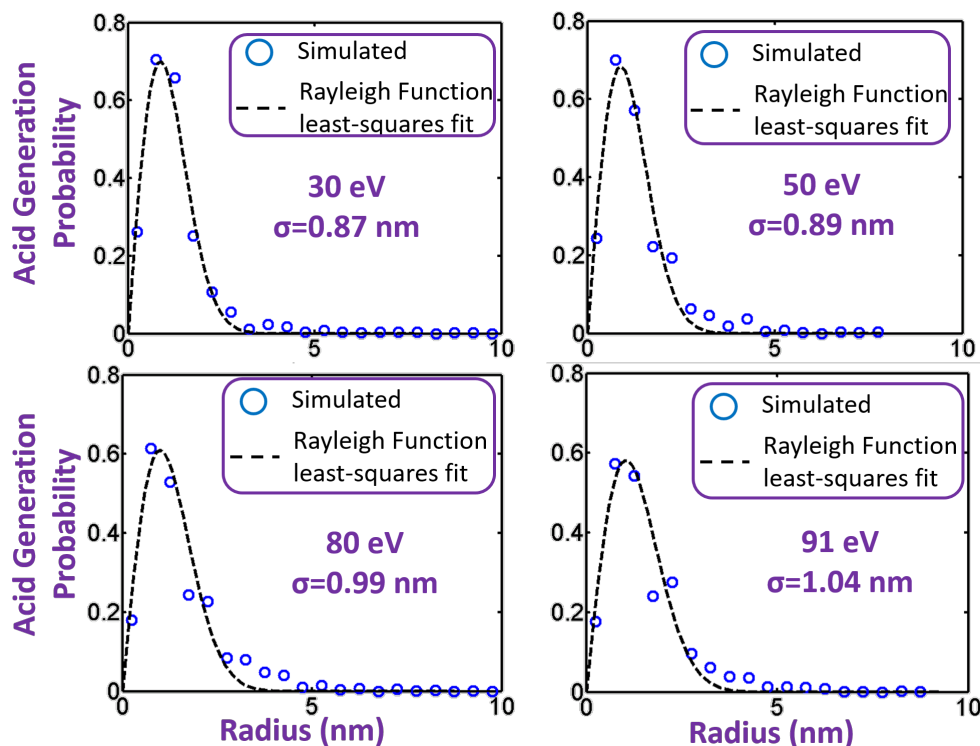
Figure 5.15: Least squares fitting of two-dimensional acid generation radii statistics with a Rayleigh distribution

5.8.2 Simulated Resist Thickness vs. Electron Exposure Dose

In these resist thickness loss simulations, a 5 nm x 5 nm area was illuminated with electron beam at the top of the resist, and the exposure dose was varied over a range of values. Top view of the exposure pattern is shown in Fig. 5.16. The color scale represents the dose used for the electron exposures. In this figure for example, an exposure dose of 4 electrons per pixel is shown. This corresponds to a dose of 4 e^-/nm^2 for this example, since the voxel dimensions of 1nm x 1 nm x 1nm are used for the simulations here.
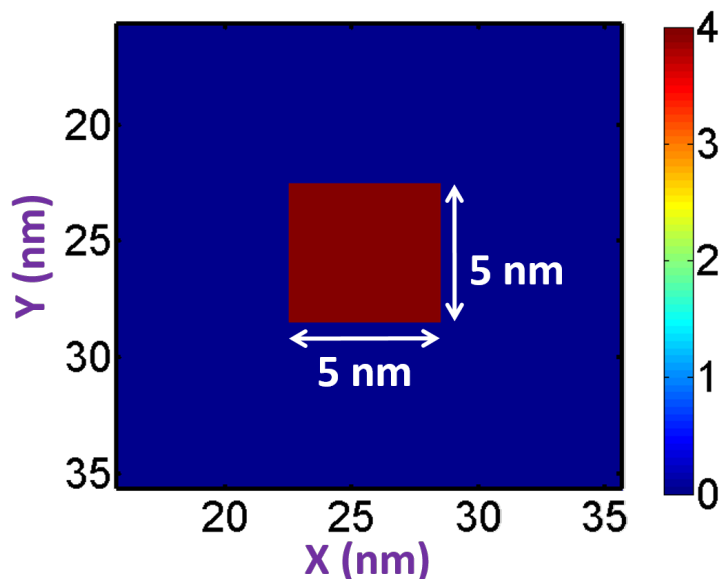
Figure 5.16: Top view of exposure pattern used for simulating the electron exposures. The color scale represents the exposure dose in electron per exposed pixel.

Example simulation results showing the acid generation sites for 29 eV and 91 eV incident energies with dose values ranging from 1 e$^-$/nm^2 (16 μC/cm^2) to 8 e$^-$/nm^2 (128 μC/cm^2) are provided in Fig. 5.17. In these images, the color scale represents the total number of acids along the y dimension for each pixel. Qualitatively, increase in the net penetration depth of the electrons as a function of dose can be seen from these images. In some of the images there are isolated acid generation events about 10 nm deep in the resist. This occurs because as described earlier, distance between scattering events is sampled from a probability distribution with an expectation value given by the mean free path. As a result, some rare acid creation events can take place at distances much larger than the electron mean free path.
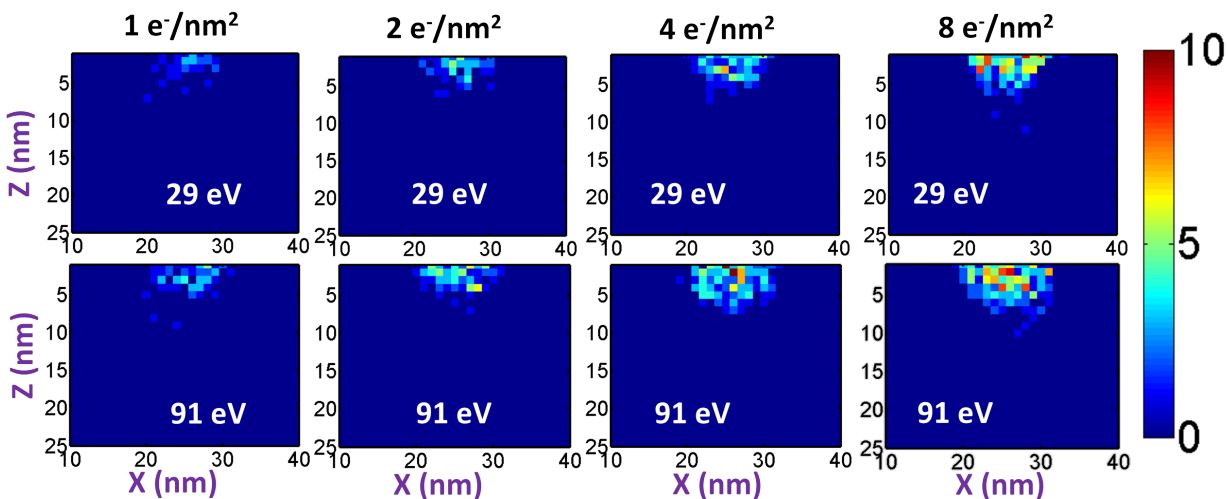
Figure 5.17: Example simulation of penetratration depth for 29 eV and 91 eV electrons for a range of dose values. The color scale represents the sum of all acids along the y dimension

Examples of final deprotection images computed with a 3-D extension of the SuMMIT resist simulation algorithm [24][25][26] by using the three-dimensional acid profile calculated using the electron scattering model are shown in Fig. 5.18. The deprotection level for each pixel is a number between 0 and 1 that denotes the fraction of the protected groups at the site that have been de-protected due to interactions with an acid during the bake process. The reaction/diffusion system used for modeling the dynamics of the acids and bases during the bake step were described in chapter 3. These cross-section images represent the mean deprotection level averaged along the length of the exposed region in the y dimension.
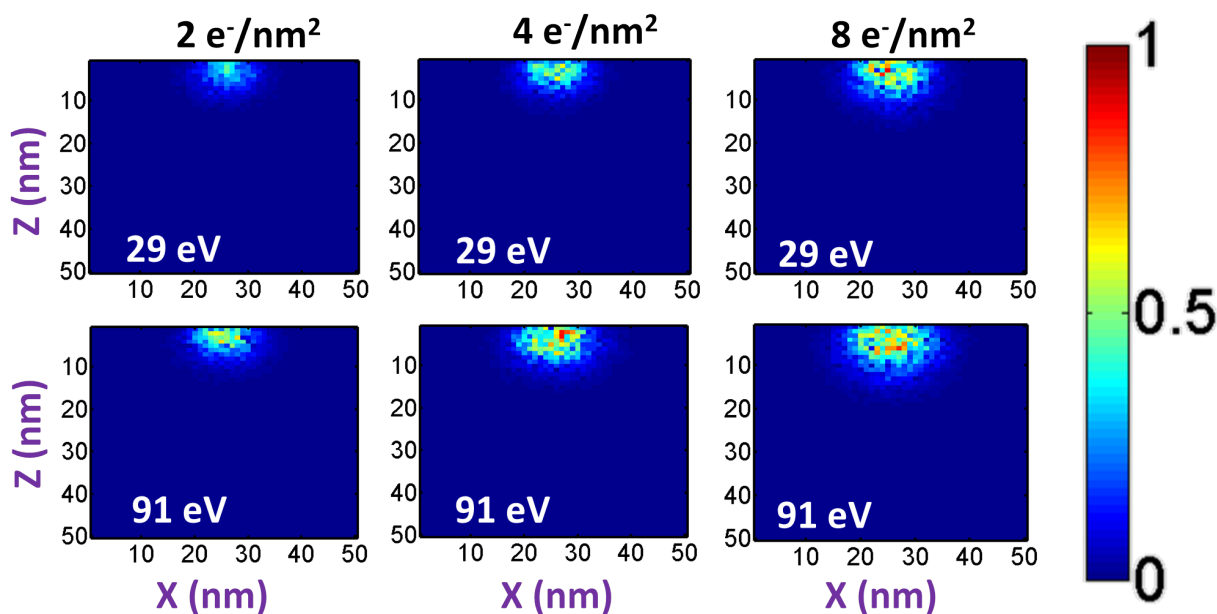
Figure 5.18: Simulated resist deprotection levels averaged along the length of the exposed region in the y dimension, computed with a 3-D implementation of the SuMMIT reaction/diffusion algorithm, the 2-D version of which was described in chapter 3

An example plot of the mean deprotection levels for each slice in the z dimension is provided for illustration purposes for 29 eV and 91 eV incident energies for a range of dose values in Fig. 5.19. On the horizontal axis, z=0nm corresponds to the top of the resist. By comparing the plots on the left with the plots on the right, it can be seen that for a given exposure dose 91 eV electrons result in a larger deprotection level compared to the 29 eV electrons. For the calculations here, a threshold de-protection level was chosen to determine the net thickness loss in the simulation. In the figure for example, a threshold level of 0.5 that was used for estimating thickness loss in subsequent plots, is shown. In the simplified dissolution model then, voxels with deprotection levels larger than this threshold would be considered as soluble in the developer solvent while the voxels with deprotection levels smaller than this threshold would be considered as insoluble.
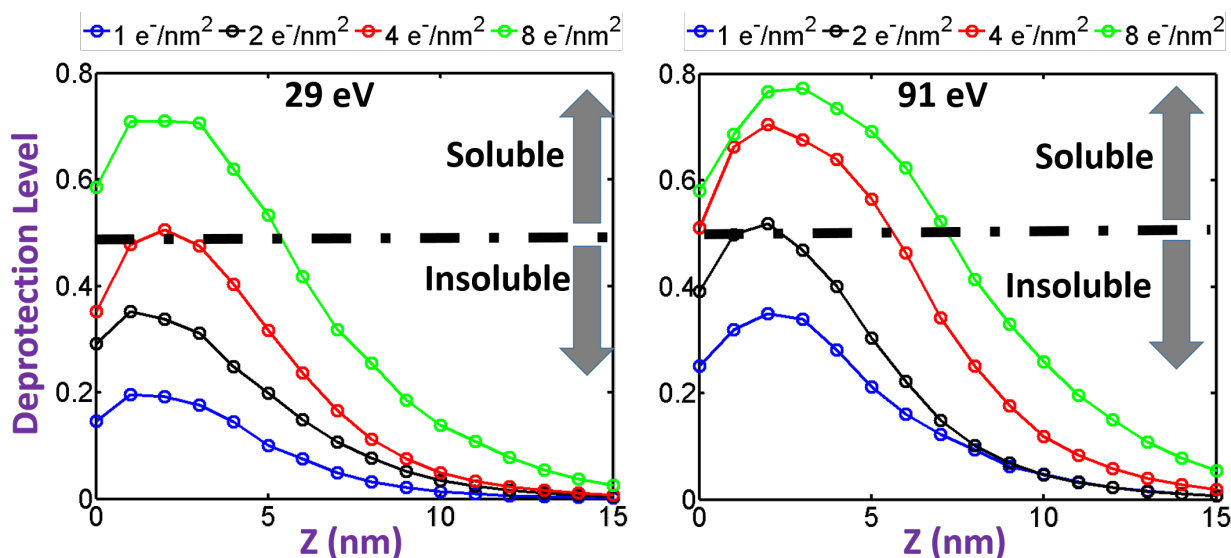
Figure 5.19: Example simulated resist deprotection levels along z dimension for 29 eV and 91 eV incident energies as a function of exposure dose

In chapter 3, the reaction and diffusion parameters that resulted in a close match between simulations and experimental lithographic data were presented. A bake temperature of 100^oC was used in the experimental results used for those comparisons. As presented in chapter 4, the bake temperature used for the 29 to 91 eV electron exposure experiments was 90^oC. Therefore, in the contrast curve simulations here, the acid diffusion length, the deprotection rate constant and the acid/base neutralization rate constant were slightly reduced relative to the best fit values from chapter 3 in order to account for the Arrhenius trends for these constants. Since the base is not expected to diffuse much [32][27], in the simulations this parameter was not perturbed and was held at a fixed small value of 5 nm used in chapter 3. A summary of the parameters that were used to simulate the contrast curves is provided in table 5.1. These parameters were chosen to obtain a reasonable match for the slope of thickness vs. logarithmic dose in the transition regions of the contrast curves.

A plot of the simulated remaining resist thickness as a function of exposure dose is provided on the left in Fig. 5.20. Plot on the right shows the total number of acids produced within the exposure volume that led to the corresponding thickness loss for various incident electron energy values.

Table 5.1: Photoresist parameters used for simulation of low energy electron exposure contrast curves

Parameter	Value
PAG number density	0.4 /nm^3
Base number density	0.04 /nm^3
Protecting groups number density	1 /nm^3
Acid diffusion length (90s bake)	8 nm
Base diffusion length (90s bake)	5 nm
Deprotection Rate	1 nm^3/s
Acid-Base Neutralization Rate	2 nm^3/s
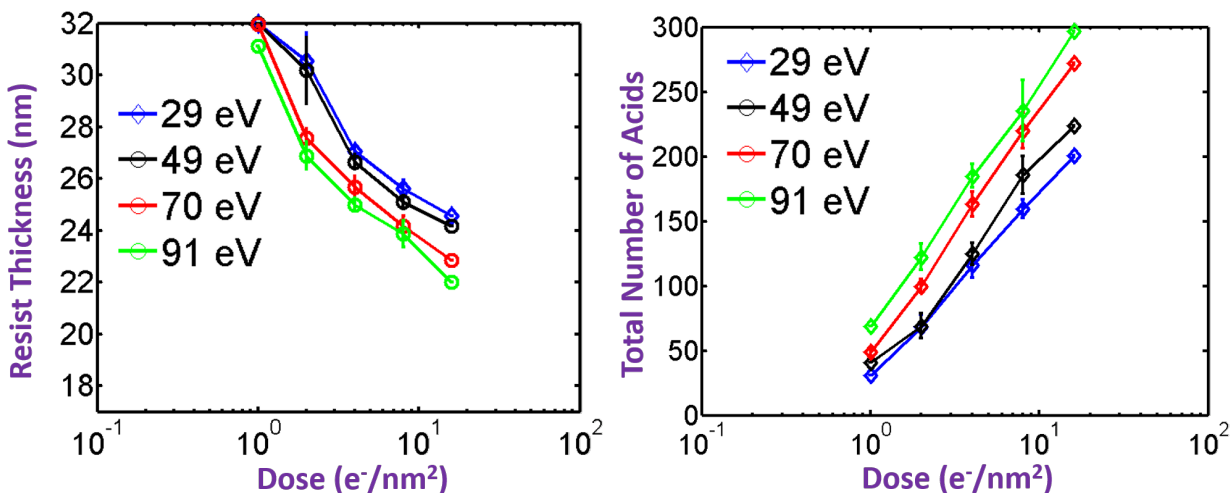
Figure 5.20: **(left):** Simulated thickness loss as a function of exposure dose for 29 eV to 91 eV incident electron energies. The resist parameters used for the calculations are summarized in table 5.1; **(right):** The total number of acids produced within exposure volume as a function of dose

In order to evaluate the efficiency with which electrons with various energies initiate chemistry that can lead to dissolution, the total acid count as a function of dose shown in Fig. 5.20 was normalized to obtain the number of acids per incident electron, as well as the number of acids per incident electron per eV energy of the electron. These results are provided in Fig. 5.21. Plot on the left shows the number of acids produced per incident electron calculated by dividing the total acid yield from Fig. 5.20 by the total number of electrons incident within the area of 25 nm^2 illustrated earlier in Fig. 5.16. The vertical axis values in this plot are not identical for all dose values because the model accounts

for PAG depletion effects. The number density of photoacid generators (PAGs) is a finite quantity (e.g., 0.4 /nm^3 was used here). As a result, considering that the average distances that electrons penetrate are on the order of a few nanometers, at very large doses a certain fraction of all the incident electrons do not create any acid due to depletion of the PAGs within the exposed volume as a function of exposure time. The number of acids created per incident electron therefore decreases with increasing dose. At the smallest dose values where the depletion effects are not severe, the number of acid creation events per incident electron is consistent with the results shown earlier in Fig. 5.10. The plot on the right shows the total acid yield per incident electron per incident eV energy. The overall trend of larger acids per unit energy with decreasing electron energy is consistent with the result shown earlier for a single electron placed in the center of a 50 nm x 50 nm x 50 nm cube (Fig. 5.10). This trend is also consistent with the experimental results for the energy delivery efficiency extracted from thickness vs. dose data for 29 to 91 eV exposures that were illustrated in chapter 4.
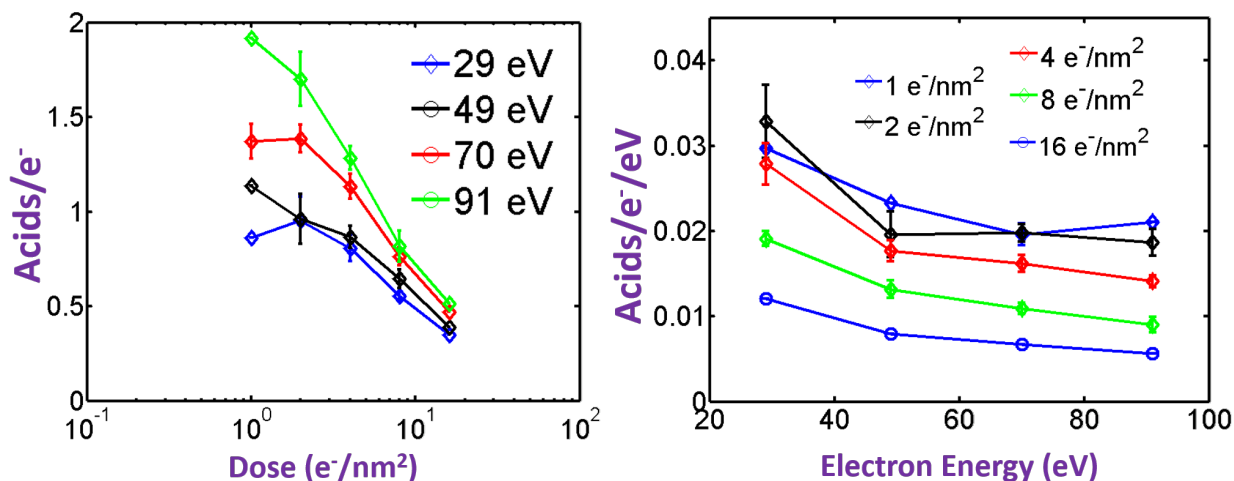
Figure 5.21: **(left):** Total number of acids per incident electron that illustrates PAG depletion effects that the model accounts for; **(right):** Total number of acids per incident electron per incident eV energy for various incident dose values

A summary of the comparisons of the slope of thickness vs. logarithmic dose between simulations and experimental data is provided in table 5.2. The resist thickness results for doses larger than the onset of dissolution were used for performing the linear fit for extracting these slopes. Using the reaction/diffusion parameters summarized in table 5.1, a close agreement is found between simulated and experimental slope values for 29 eV, 49 eV and 91 eV exposures, for which data is available and was illustrated in chapter 4.

Table 5.2: Comparison of slope of resist thickness vs. logarithmic dose between simulations and experimental data

Energy	Slope (sim)	Slope (expt)
29 eV	-6.7	-6.6
49 eV	-6.5	-6.9
91 eV	-6.6	-7.1

5.9 Summary

Interactions of electrons with energies larger than 20 eV and smaller than 91 eV in a chemically amplified EUV resist were studied in this chapter from a modeling standpoint. A technique for simulating electron trajectories using the analytical dielectric model for inelastic scattering was presented. As a way of calibrating the scattering model to data, the energy loss function (Im[-1/ϵ]) that was directly measured for a chemically amplified EUV resist was used for calculating scattering parameters like the mean free path and the energy and angle-differential scattering cross-sections. These calculations were performed using the analytical Mermin dielectric functions.

A simplified model for electron-PAG interactions based on electronic excitations seen as the 6 eV peak in the energy loss distributions measured with EELS was used to model acid generation in the resist. Results showed that an 80 eV electron leads to 1.6 acid generation events by the time its energy drops to 20 eV. The total number of acids was found to increase as a function of electron energy, as expected. A distribution of acid generation blur was extracted from the simulation results, and was fit to a polar Rayleigh function. Peak positions of the radii were found to occur between 1.8 nm and 2 nm from the site of generation of an electron.

In order to complement the experimental methodology presented in chapter 4, simulations were also performed of the contrast curves that result from creation of acids near the top surface of the resist as a result of exposure to electrons and subsequent diffusion and reactions during bake.

Chapter 6

Conclusions

6.1   Line Edge Roughness Study

In this thesis, two aspects of interactions in photoresists for EUV lithography were studied. A new approach of comparative analysis of EUV and e-beam lithography performance for experimental investigation of the influence of absorption count statistics on LER was tested. The key contribution of this project is that the experiments were performed with matched imaging conditions between EUV and e-beam lithography, which allowed for a fair comparison between LER values measured using the two patterning technologies. In scenarios where the e-beam spatial resolution was better than that for EUV, the technique of gray-scale e-beam lithography was experimentally demonstrated to result in closely matched image gradients between e-beam and EUV patterning. It was shown that the measurable parameter known as the exposure latitude can be used to test how well the aerial images are matched for idential materials and processing conditions.

From the data on the probability of energy loss events by 100 keV electrons, it was learned that despite having access to core energy levels (e.g., 284 eV ionization edge due to carbon), the electrons lose on average only about 35 eV in the resist film. The net probability of inelastic scattering events in a 45 nm thick film was determined to be 2.36x larger than for EUV photons depositing 92 eV for resist A, and 1.73x for resist B. In the lithography experiments however, these discrepancies in absorption probabilities almost exactly canceled out by a scaling of the incident dose needed to print 50 nm half-pitch lines and spaces. These results provide indication that the energy distribution of electrons created in the system by the two exposure mechanisms were likely not different enough to cause a discrepancy in the volumetric density of acids created by a single absorption event. With matched exposure latitudes and roughly equal absorption count however, e-beam lithography resulted in mean LER values larger by about 1 nm. The overall technique shown here, of using multiple beams to assess the influence of shot noise should aim for creating a discrepancy in the acid yield efficiency of an absorbed photon. Performing a comparison between DUV and EUV lithography with matched materials, processing and imaging conditions is a potential option.

Influence of various material contributors on resist LER was also studied by using a stochastic resist simulator. The reaction/diffusion parameters in the resist model were calibrated by using a combination of measured resist contrast curves that resulted from large area open frame EUV exposures, as well as line/space patterning data from exposures performed with the Berkeley MET. Using the best fit rate constant and the acid diffusion length, the simulator was found to under-predict the experimentally determined LER values. This indicates the presence of other contributors to the final resist LER. Considering that at best focus the mask contribution is likely small, some of the discrepancy between modeled and experimental LER is likely coming from the statistics of chemical interactions during the dissolution process. For the calculations presented here, photon shot noise was found to contribut 46% of the total deprotection image LER, while base loading and acid generation statistics accounted for 32% and 22% respectively, of the total LER.

6.2 Study of Electron Interactions in EUV Resists

To gain insights into the amount of work done by electrons at low energies typical of those that would be created by absorption of an EUV photon, a leading chemically amplified EUV resist was directly exposed with low energy electrons. Measurements of thickness loss in the resist were made as a function of exposure dose with electrons with incident energies between 15 eV and 91 eV. The thickness removed was much larger than the average secondary electron range and was bake temperature dependent and thus is a useful indicator of acid diffusion. Through a simple fitting procedure and assuming a Gaussian deprotection profile, the deprotection standard deviation values were found to be around 5 nm for a bake temperature of 110^oC, and between 2 and 3.5 nm for 90^oC bake. The data for thickness loss also allowed for calculating the volume over which a single electron at various energies can cause chemical reactions that can lead to dissolution. The volume removed was about 0.1 nm^3 per eV energy per 1 nm^2 area. The dissolution per eV deposited energy was nearly similar for 29 eV to 91 eV exposures, although there is some indication that incident electrons with lower energies are slightly more effective at causing chemical reactions.

A well known analytical model for inelastic mean free path of electrons in solids, known as the dielectric model, was used to create a simple simulator that models movement of electrons in a 3-D grid in a probabilistic manner. In order to capture the energy and momentum (q) transfer that occur during an inelastic scattering event, an analytical dielectric function known as the Mermin dielectric function was used. As a way of calibrating this analytical function to scattering properties in an actual resist, the dielectric function of the resist was measured over a wide energy loss range using EELS, and the absorption peaks were fit with a linear combination of these Mermin functions. By calculating 1024 electron trajectories in the resist, a distribution of acid generation blur relative to point of origin of the electron was extracted and was fit to a polar Rayleigh function. Peak positions of the radii were found to occur around 1.8 nm to 2 nm from the site of generation of an electron. The utility of this fit function is that it can be used in simpler simulators that may not take

into account electron interactions that are primarily responsible for delivering energy in the resist. Through analysis of acid yields from 1024 trials, 80 eV electrons were found to create 1.6 acids on average.

6.3 Future Directions

Exposing the resists with low energy electron can be used as a general technique for characterizing blur introduced by the bake process not only for chemically amplified resists, but also for the metal-organic resists that are currently popular for their high absorption characteristics. Specifically, since scanning electron microscopes (SEMs) are so ubiquitous and most of the modern ones provide the option of using the deceleration technology, this is a simple approach to test a few aspects of new EUV materials. The phenomenon of charging however, puts a limit on the energies that can be used for obtaining reliable data. Developing models for charging dynamics and extracting the surface potential on the sample during exposures through a combination of data collection and modeling is a worthwhile topic of future research.

On the simulation side, in order to improve the accuracy of acid yield calculations, developing probabilistic models for scattering of electrons in resists at low energies (e.g., less than 20 eV) is needed. For example, elastic scattering mechanisms were not considered in the model presented here and may prove to be important at lower energies. Similarly, experimental techniques like electron energy loss spectroscopy (EELS) with low energy primary electrons may provide useful information pertaining to scattering cross-sections which could be directly fed into the simulator as a look up table to model movement of electrons. The techniques for performing EELS with low energy (less than 20 eV) electrons with energy resolutions of milli-electronvolts are well established in the literature. As an example, Khakoo et. al. [72] demonstrated gas phase measurements of the cross-sections for scattering of less than 20 eV electrons from tetrahydrofuran (C_4H_8O) molecules. Similar experiments could be performed with resist molecules.

Bibliography

[1]   C. Mack. *Fundamental Principles of Optical Lithography*. John Wiley & Sons, 2007.

[2]   G. E. Moore. "Cramming more components onto integrated circuits, Reprinted from Electronics, volume 38, number 8, April 19, 1965, pp.114 ff." In: *IEEE Solid-State Circuits Society Newsletter* 11.5 (Sept. 2006), pp. 33–35. ISSN: 1098-4232.

[3]   W. Kaiser. *EUV Optics: Achievements and Future Perspectives*. 2015.

[4]   B. McClinton. "Mask Roughness Induced Line-Edge Roughness in Extreme Ultraviolet Lithography". PhD thesis. UC, Berkeley, July 2011.

[5]   R. Claus. "Partially Coherent Quantitative Phase Retrieval with Applications to Extreme Ultraviolet Lithography". PhD thesis. UC, Berkeley, 2015.

[6]   G. M. Gallatin et al. *Resolution, LER, and sensitivity limitations of photoresists*. 2008. URL: http://dx.doi.org/10.1117/12.772763.

[7]   P. P. Naulleau, D. Niakoula, and G. Zhang. "System-level line-edge roughness limits in extreme ultraviolet lithography". In: *Journal of Vacuum Science & Technology B: Microelectronics and Nanometer Structures Processing, Measurement, and Phenomena* 26.4 (2008), pp. 1289–1293. eprint: http://avs.scitation.org/doi/pdf/10.1116/1.2932100. URL: http://avs.scitation.org/doi/abs/10.1116/1.2932100.

[8]   R. F. Egerton. *Electron Energy-Loss Spectroscopy in the Electron Microscope*. New York, NY: Springer, 2011.

[9]   P. Ewels et al. "A Complete Overhaul of the Electron Energy-Loss Spectroscopy and X-Ray Absorption Spectroscopy Database: eelsdb.eu". In: *Microscopy and Microanalysis* 22 (Feb. 2016), pp. 717–724. ISSN: 1435-8115. URL: http://journals.cambridge.org/article_S1431927616000179.

[10] *EELS Data Base*. 2016. URL: https://eelsdb.eu/.

[11] *EELS Atlas*. URL: https://eelsdb.eu/.

[12] R. H. Ritchie. "Plasma Losses by Fast Electrons in Thin Films". In: *Phys. Rev.* 106 (5 June 1957), pp. 874–881. URL: http://link.aps.org/doi/10.1103/PhysRev.106.874.

[13] *Molecular Foundry TEM-EELS*. URL: http://foundry.lbl.gov/facilities/ncem/expertise.html.

[14] I. Waki and Y. Hirai. "The silicon L-edge photoabsorption spectrum of silicon carbide". In: *Journal of Physics: Condensed Matter* 1.37 (1989), p. 6755. URL: http://stacks. iop.org/0953-8984/1/i=37/a=021.

[15] *The CXRO Reflectometer*. URL: http://cxro.lbl.gov//reflectometer.

[16] *The CXRO Database of Index of Refraction*. URL: http://henke.lbl.gov/optical_ constants/getdb2.html.

[17] *NIST E-STAR Database: Stopping Power and Range Tables for Electrons*. URL: http: //physics.nist.gov/PhysRefData/Star/Text/ESTAR.html.

[18] S. A. Rishton and D. P. Kern. "Point exposure distribution measurements for prox- imity correction in electron beam lithography on a sub-100 nm scale". In: *Journal of Vacuum Science & Technology B: Microelectronics Processing and Phenomena* 5.1 (1987), pp. 135–141. eprint: http://avs.scitation.org/doi/pdf/10.1116/1.583847. URL: http://avs.scitation.org/doi/abs/10.1116/1.583847.

[19] T. Kozawa et al. "Analysis of acid yield generated in chemically amplified electron beam resist". In: *Journal of Vacuum Science & Technology B: Microelectronics and Nanome- ter Structures Processing, Measurement, and Phenomena* 24.6 (2006), pp. 3055–3060. eprint: http://avs.scitation.org/doi/pdf/10.1116/1.2366656. URL: http://avs.scitation. org/doi/abs/10.1116/1.2366656.

[20] G. Owen. "Methods for proximity effect correction in electron lithography". In: *Journal of Vacuum Science & Technology B: Microelectronics Processing and Phenomena* 8.6 (1990), pp. 1889–1892. eprint: http://avs.scitation.org/doi/pdf/10.1116/1.585179. URL: http://avs.scitation.org/doi/abs/10.1116/1.585179.

[21] E. H. Anderson et al. "Influence of sub-100 nm scattering on high-energy electron beam lithography". In: *Journal of Vacuum Science & Technology B: Microelectron- ics and Nanometer Structures Processing, Measurement, and Phenomena* 19.6 (2001), pp. 2504–2507. eprint: http://avs.scitation.org/doi/pdf/10.1116/1.1415506. URL: http://avs.scitation.org/doi/abs/10.1116/1.1415506.

[22] P. P. Naulleau and S. A. George. *Implications of image plane line-edge roughness requirements on extreme ultraviolet mask specifications*. 2009. URL: http://dx.doi.org/ 10.1117/12.824265.

[23] *The SuMMIT lithography analysis toolset*. 2016. URL: http://lithometrix.com/.

[24] P. P. Naulleau and G. M. Gallatin. "Effect of resist on the transfer of line-edge rough- ness spatial metrics from mask to wafer". In: *Journal of Vacuum Science & Technol- ogy B, Nanotechnology and Microelectronics: Materials, Processing, Measurement, and Phenomena* 28.6 (2010), pp. 1259–1266.

[25] P. P. Naulleau. *Multivariate Poisson Propagation Model and Resist Stochastics*. 2015.

[26] P. P. Naulleau et al. "Studying Resist Stochastics with the Multivariate Poisson Propagation Model". In: *Journal of Photopolymer Science and Technology* 27.6 (2014), pp. 747–750.

[27] W. D. Hinsberg et al. "Effect of resist components on image spreading during postexposure bake of chemically amplified resists". In: *Proc. SPIE* 3999 (2000), pp. 148–160. URL: http://dx.doi.org/10.1117/12.388294.

[28] L. Yuan. "Modeling and calibration of resist processes in photolithography". PhD thesis. UC, Berkeley, 2005.

[29] E. Croffie, M. Cheng, and A. Neureuther. "Moving boundary transport model for acid diffusion in chemically amplified resists". In: *Journal of Vacuum Science & Technology B: Microelectronics and Nanometer Structures Processing, Measurement, and Phenomena* 17.6 (1999), pp. 3339–3344.

[30] S. Nagahara et al. *Understanding quencher mechanisms by considering photoacid-dissociation equilibrium in chemically amplified resists.* 2005. URL: http://dx.doi.org/10.1117/12.598949.

[31] F. A. Houle et al. "Determination of coupled acid catalysis-diffusion processes in a positive-tone chemically amplified photoresist". In: *Journal of Vacuum Science & Technology B: Microelectronics and Nanometer Structures Processing, Measurement, and Phenomena* 18.4 (2000), pp. 1874–1885.

[32] F. A. Houle, W. D. Hinsberg, and M. I. Sanchez. "Acid-base reactions in a positive tone chemically amplified photoresist and their effect on imaging". In: *Journal of Vacuum Science & Technology B: Microelectronics and Nanometer Structures Processing, Measurement, and Phenomena* 22.2 (2004), pp. 747–757.

[33] J. J. Biafore and M. D. Smith. *Application of stochastic modeling to resist optimization problems.* 2012. URL: http://dx.doi.org/10.1117/12.916518.

[34] R. Gronheid et al. "Extreme-ultraviolet secondary electron blur at the 22-nm half pitch node". In: *Journal of Micro/Nanolithography, MEMS, and MOEMS* 10.3 (2011), pp. 033004-033004-7. URL: http://dx.doi.org/10.1117/1.3607429.

[35] J. S. Petersen et al. *Characterization and modeling of a positive-acting chemically amplified resist.* 1995. URL: http://dx.doi.org/10.1117/12.210377.

[36] B. Jung et al. *Sub-millisecond post exposure bake of chemically amplified resists by CO2 laser heat treatment.* 2010. URL: http://dx.doi.org/10.1117/12.848418.

[37] C. W. L R Hargreaves M. A. Khakoo and V. McKoy. "Excitation of the lowest electronic transitions in ethanol by low-energy electrons". In: *Journal of Physics B: Atomic, Molecular and Optical Physics* 49.18 (2016), p. 185201. URL: http://stacks.iop.org/0953-4075/49/i=18/a=185201.

[38] M. A. Khakoo et al. "Electron-impact vibrational excitation of tetrahydrofuran". In: *Phys. Rev. A* 88 (1 July 2013), p. 012705. URL: http://link.aps.org/doi/10.1103/PhysRevA.88.012705.

[39] A. Narasimhan et al. *Studying electron-PAG interactions using electron-induced fluorescence.* 2016. URL: http://dx.doi.org/10.1117/12.2219850.

[40] S. Grzeskowiak et al. *Cross sections of EUV PAGs: influence of concentration, electron energy, and structure.* 2016. URL: http://dx.doi.org/10.1117/12.2219851.

[41] A. Narasimhan et al. *Studying secondary electron behavior in EUV resists using experimentation and modeling.* 2015. URL: http://dx.doi.org/10.1117/12.2086596.

[42] A. Thete et al. *Low-energy electron (0-100eV) interaction with resists using LEEM.* 2015. URL: http://dx.doi.org/10.1117/12.2085369.

[43] D. F. Ogletree. *Primary excitation and relaxation in EUVL molecular resists.* 2016.

[44] *Molecular Foundry SPLEEM tool webpage.* URL: http://foundry.lbl.gov/facilities/ncem/expertise.html#spleem.

[45] T. J. Shaffner and R. D. V. Veld. "'Charging' effects in the scanning electron microscope". In: *Journal of Physics E: Scientific Instruments* 4.9 (1971), p. 633. URL: http://stacks.iop.org/0022-3735/4/i=9/a=002.

[46] S. Babin et al. "Simulation of scanning electron microscope images taking into account local and global electromagnetic fields". In: *Journal of Vacuum Science & Technology B, Nanotechnology and Microelectronics: Materials, Processing, Measurement, and Phenomena* 28.6 (2010), pp. C6C41–C6C47.

[47] H. Abe et al. *Time dependence of SEM signal due to charging: measurements and simulation using Monte Carlo software.* 2009. URL: http://dx.doi.org/10.1117/12.816899.

[48] M. Bai et al. "Charging and discharging of electron beam resist films". In: *Journal of Vacuum Science & Technology B: Microelectronics and Nanometer Structures Processing, Measurement, and Phenomena* 17.6 (1999), pp. 2893–2896. eprint: http://avs.scitation.org/doi/pdf/10.1116/1.591091. URL: http://avs.scitation.org/doi/abs/10.1116/1.591091.

[49] G. Denbeaux et al. *Measurement of the role of secondary electrons in EUV resist exposures.* 2013. URL: https://www.euvlitho.com/2013/P29.PDF.

[50] J. Villarrubia et al. "Scanning electron microscope measurement of width and shape of 10 nm patterned lines using a JMONSEL-modeled library". In: *Ultramicroscopy* 154 (2015), pp. 15–28. ISSN: 0304-3991. URL: http://www.sciencedirect.com/science/article/pii/S0304399115000133.

[51] J. J. Biafore et al. *Resist pattern prediction at EUV.* 2010. URL: http://dx.doi.org/10.1117/12.846535.

[52] C. A. Mack et al. "Stochastic exposure kinetics of extreme ultraviolet photoresists: simulation study". In: *Journal of Micro/Nanolithography, MEMS, and MOEMS* 10.3 (2011), pp. 033019-033019-11. URL: http://dx.doi.org/10.1117/1.3631753.

[53] C. A. Mack, J. J. Biafore, and M. D. Smith. "Stochastic exposure kinetics of extreme ultraviolet photoresists: Trapping model". In: *Journal of Vacuum Science & Technology B, Nanotechnology and Microelectronics: Materials, Processing, Measurement, and Phenomena* 31.6 (2013), 06F603.

[54] T. Kozawa, A. Saeki, and S. Tagawa. "Modeling and simulation of chemically amplified electron beam, x-ray, and EUV resist processes". In: *Journal of Vacuum Science & Technology B: Microelectronics and Nanometer Structures Processing, Measurement, and Phenomena* 22.6 (2004), pp. 3489–3492.

[55] N. P. Hacker and K. M. Welsh. "Photochemistry of triphenylsulfonium salts in poly[4-[(tert-butoxycarbonyl)oxystyrene]: evidence for a dual photoinitiation process". In: *Macromolecules* 24.8 (1991), pp. 2137–2139.

[56] R. H. Ritchie. "Plasma Losses by Fast Electrons in Thin Films". In: *Phys. Rev.* 106 (5 June 1957), pp. 874–881. URL: https://link.aps.org/doi/10.1103/PhysRev.106.874.

[57] M. Dapor. "Computer Simulation of Electron Transport in Solids with Applications to Materials Analysis and Characterization". PhD thesis. University of Trento, 2013.

[58] D. Emfietzoglou et al. "The effect of static many-body local-field corrections to inelastic electron scattering in condensed media". In: *Journal of Applied Physics* 114.14 (2013), p. 144907.

[59] I. Abril et al. "Dielectric description of wakes and stopping powers in solids". In: *Phys. Rev. A* 58 (1 July 1998), pp. 357–366. URL: https://link.aps.org/doi/10.1103/PhysRevA.58.357.

[60] C. T. Chantler and J. D. Bourke. "Electron Inelastic Mean Free Path Theory and Density Functional Theory Resolving Discrepancies for Low-Energy Electrons in Copper". In: *The Journal of Physical Chemistry A* 118.5 (2014), pp. 909–914.

[61] J. Bourke and C. Chantler. "Low-energy electron energy losses and inelastic mean free paths in zinc, selenium, and zinc selenide". In: *Journal of Electron Spectroscopy and Related Phenomena* 196 (2014). Advances in Vacuum Ultraviolet and X-ray Physics, The 38th International Conference on Vacuum Ultraviolet and X-ray Physics (VUVX2013), University of Science and Technology of China, pp. 142–145. ISSN: 0368-2048. URL: http://www.sciencedirect.com/science/article/pii/S0368204814000437.

[62] S. Tanuma, C. J. Powell, and D. R. Penn. "Calculations of electron inelastic mean free paths V Data for 14 organic compounds over the 50 to 2000 eV range". In: *Surface and Interface Analysis* 21.3 (1994), pp. 165–176. ISSN: 1096-9918. URL: http://dx.doi.org/10.1002/sia.740210302.

[63] S. Tanuma, C. J. Powell, and D. R. Penn. "Calculations of electron inelastic mean free paths. III. Data for 15 inorganic compounds over the 50 to 2000 eV range". In: *Surface and Interface Analysis* 17.13 (1991), pp. 927–939. ISSN: 1096-9918. URL: http://dx.doi.org/10.1002/sia.740171305.

[64] S. Tanuma, C. J. Powell, and D. R. Penn. "Calculations of electron inelastic mean free paths. IX. Data for 41 elemental solids over the 50 eV to 30 keV range". In: *Surface and Interface Analysis* 43.3 (2011), pp. 689–713. ISSN: 1096-9918. URL: http://dx.doi.org/10.1002/sia.3522.

[65] S. Tanuma, C. J. Powell, and D. R. Penn. "Calculations of electron inelastic mean free paths. IX. Data for 41 elemental solids over the 50 eV to 30 keV range". In: *Surface and Interface Analysis* 43.3 (2011), pp. 689–713. ISSN: 1096-9918. URL: http://dx.doi.org/10.1002/sia.3522.

[66] M. Dapor. "Mermin Differential Inverse Inelastic Mean Free Path of Electrons in Polymethylmethacrylate". In: *Frontiers in Materials* 2 (2015), p. 27. ISSN: 2296-8016. URL: http://journal.frontiersin.org/article/10.3389/fmats.2015.00027.

[67] M. P. Seah and W. A. Dench. "Quantitative electron spectroscopy of surfaces: A standard data base for electron inelastic mean free paths in solids". In: *Surface and Interface Analysis* 1.1 (1979), pp. 2–11. ISSN: 1096-9918. URL: http://dx.doi.org/10.1002/sia.740010103.

[68] J. D. Bourke and C. T. Chantler. "Measurements of Electron Inelastic Mean Free Paths in Materials". In: *Phys. Rev. Lett.* 104 (20 May 2010), p. 206601. URL: https://link.aps.org/doi/10.1103/PhysRevLett.104.206601.

[69] J. D. Bourke and C. T. Chantler. "Electron Energy Loss Spectra and Overestimation of Inelastic Mean Free Paths in Many-Pole Models". In: *The Journal of Physical Chemistry A* 116.12 (2012). PMID: 22390614, pp. 3202–3205.

[70] J. Llacer and E. L. Garwin. "Electron Phonon Interaction in Alkali Halides. I. The Transport of Secondary Electrons with Energies between 0.25 and 7.5 eV". In: *Journal of Applied Physics* 40.7 (1969), pp. 2766–2775.

[71] M. Dapor. "Monte Carlo Simulation of Secondary Electron Emission from Dielectric Targets". In: *Journal of Physics: Conference Series* 402.1 (2012), p. 012003. URL: http://stacks.iop.org/1742-6596/402/i=1/a=012003.

[72] M. A. Khakoo et al. "Electron-impact vibrational excitation of tetrahydrofuran". In: *Phys. Rev. A* 88 (1 July 2013), p. 012705. URL: https://link.aps.org/doi/10.1103/PhysRevA.88.012705.